þÿ M R I c o n t r a s t i n t h e l o c u s c S r u l e u s : O p t i m i s a t i o n w i t h spoiled gradient echo imaging

Auteur : Beckers, Elise
Promoteur(s) : Phillips, Christophe
Faculté : Faculté des Sciences appliquées
Diplôme : Master en ingénieur civil biomédical, à finalité spécialisée
Année académique : 2019-2020
URI/URL : http://hdl.handle.net/2268.2/8842



UNIVERSITY OF LIÈGE - FACULTY OF APPLIED SCIENCES
UNIVERSITY COLLEGE LONDON - FUNCTIONAL IMAGING LABORATORY
WELLCOME CENTRE FOR HUMAN NEUROIMAGING

MRI CONTRAST IN THE LOCUS CŒRULEUS:

OPTIMISATION WITH MULTI-COMPARTMENT SPOILED GRADIENT ECHO IMAGING

GRADUATION STUDIES CONDUCTED BY

ELISE BECKERS

WITH THE AIM OF OBTAINING THE MASTER'S DEGREE IN BIOMEDICAL ENGINEERING

Under the supervision of

Pr. Christophe PHILLIPS
Dr. Martina CALLAGHAN
Dr. Nadège CORBIN

ACADEMIC YEAR 2019 - 2020

Abstract

The locus cœruleus (LC) is a small noradrenergic nucleus of high interest in neuroscience. As the main source of noradrenaline in the brain, it is involved in numerous cognitive functions such as arousal, attention and memory. In addition, previous studies have emphasised its relationship with the progression of neurodegenerative disorders such as Alzheimer's and Parkinson's diseases. The visualisation of the LC in magnetic resonance imaging (MRI) is realised through so-called neuromelanin-imaging in which magnetisation transfer (MT) effects are thought to be the main source of contrast. However, current researches insufficiently characterise the underlying contrast generation mechanisms given the poor understanding in the LC tissue properties. Efficiently visualising the locus cœruleus is therefore a challenging process that requires further investigation.

The aim of this thesis is to provide an efficient tool for better understanding the underlying contrast mechanisms in the LC and thereby optimising its visualisation through multi-compartment spoiled gradient echo (SPGR) imaging. Firstly, the simulation of such a sequence through the extended phase graph with exchange (EPG-X) framework is performed in order to determine optimal sequence parameter values. After an experimentation phase, the outcomes are validated against the developed model. Simulation suggests that an optimal contrast can be achieved by maximising the power of the excitation pulse. It is expected that the use of optimal sequences compared to the one currently played out at the Wellcome Centre for Human Neuroimaging (WCHN) would improve the LC visualisation. Nonetheless, the lack of robust validation prevent the generalisation of these observations. Secondly, the SPGR model is extended by including a saturation pre-pulse for amplifying the MT effects. The contrast optimisation is realised through simulation according to the same formalism as previously while accounting for the MT pre-pulse. Optimal parameter values suggest that an improvement is achievable regarding the MT-weighted sequence currently played out through the maximisation of the power and the off-resonance frequency of the MT pulse as well as the time delay between the saturation and excitation pulses. Unfortunately, no validation was achievable for this configuration which should be investigated in future researches.

Because of the lack of knowledge about the contrast mechanisms in the LC, the optimisation of an MRI sequence effectively targeting the LC is complex. Therefore, due to the numerous parameters involved and the poor confidence regarding their impact, future studies should focus on a better characterisation of this structure and the inherent contrast mechanisms.

Acknowledgments

This master thesis was my first long term project and allowed me to experiment the world of research and the associated challenges. Despite the unfortunate Covid-19 pandemic crisis forcing me to work remotely and preventing me to acquire as much experimental data as expected, I always felt supported and helped by the right people through the progression of this project. I definitely would not have been able to complete this work without the contributions, from near and far, of various important people that I would like to sincerely thank.

First of all, I would like to express my gratitude to Mr. Christophe Phillips, my supervisor and professor at the University of Liège, for giving me the opportunity to work on such an interesting subject and spend two wonderful months in London. Besides the wise advice, he has always provided support regarding my project and the unexpected situation.

Furthermore, I am sincerely grateful for my London supervisors Martina Callaghan and Nadège Corbin. First, for including me to the lovely physics group but more especially for their precious guidance and support in my work from the very beginning. They were always available for answering any of my concerns and provided numerous insightful revisions on the report. I must say that I never learned as much as working under their instructive supervision. Despite the social distancing circumstances, we kept in strong contact with weekly meetings as if we were in the same room which allowed me to efficiently handle the finalisation of the project.

The realisation of this thesis was combined with an internship at the Wellcome Centre for Human Neuroimaging of the University College of London and I would like to express my gratefulness to the Physics team for the friendly atmosphere during and out of working hours.

Finally, I will never thank enough my family and friends for their continuous mental support during this project and more generally during all the steps of my studies. I feel very lucky to be surrounded by such inspiring and stimulating people. Particularly, I'm grateful for my parents confidence, never letting me think less of myself, pushing me at my maximum and getting me back on track when I was lost. This work is somehow their indirect achievement. I also thank them for offering my the multiple resources to go abroad and live this amazing experience in London.

Contents

List of Figures

List of Tables

Table of abbreviations

ABBREVIATION	FULL FORM
BWT	Bandwidth-Time Product
CSF	Cerebrospinal Fluid
EPG	Extended Phase Graph
EPG-X	Extended Phase Graph with Exchange
fMRI	Functional Magnetic Resonance Imaging
FOV	Field Of View
GRE	Gradient Echo
LC	Locus Cœruleus
MPM	Multi-Parametric Mapping
MR	Magnetic Resonance
MRI	Magnetic Resonance Imaging
MT	Magnetisation Transfer
NA	Noradrenaline
NM	Neuromelanin
NMR	Nuclear Magnetic Resonance
PD	Proton Density
PSR	Pool Size Ratio
RF	Radiofrequency
SAR	Signal Absorption Rate
SNR	Signal-to-Noise Ratio
SPGR	Spoiled Gradient Echo
SPM	Statistical Parametric Mapping
SR	Super-Resolution
TE	Echo time
TR	Repetition time
TSE	Turbo Spin Echo
WCHN	Wellcome Centre for Human Neuroimaging

Introduction

Among the numerous challenges that our society faces today, neurodegenerative diseases are one of the most important concerns in terms of population health and economy. Nowadays, more than 50 million people worldwide are suffering from dementia [2] and this number is expected to rise up to 135 million by 2050 as the population ages [5]. Alzheimer's disease is the most common cause of dementia leading to the impairment of cognitive functions such as memory. Yet, no effective treatments exist despite the multitude of studies and research conducted. The main challenge lies in the poor characterisation of the early stages of the disease progression often referred to as the prodromal phase [1]. Increasing our knowledge and understanding of this disease stage is crucial to the development of therapeutic interventions and halting the disease.

Multiple studies have repeatedly shown that the degeneration of the locus cœruleus, a small noradrenergic structure of the brain, was highly related to the early stages of neurodegenerative diseases such as Alzheimer's and Parkinson's diseases [9, 40]. The evolution of the LC neuronal population could therefore represent a reliable biomarker for noradrenergic dysfunction of the early disease processes. The high interest in the relation between the LC degeneration and the neurodegenerative disorder progression has therefore emphasised the need for a reliable *in vivo* characterisation of this structure in order to detect and treat the disease as early as possible.

Magnetic resonance imaging provides a means of non-invasively characterising these structures. However, imaging the LC is challenging because of its small size and because the contrast mechanisms by which visualisation can be achieved are not yet fully understood. In fact, there are many different influences on the measured signal intensity and relative contrast in the LC. Nevertheless, some techniques taking advantages of its macromolecular composition have demonstrated their efficiency in targeting the LC. While the underlying mechanisms for generating the contrast between this nucleus and its surroundings are still badly understood, neuromelanin-sensitive MRI exhibits promising results at depicting this structure [28, 38]. It is thought that the inherent magnetisation transfer effects combined with other complex mechanisms are the main source of the observed relative contrast in the LC [43].

The realisation of this project was motivated by the requirement for a better targeting of the LC in neuroscience. While several MRI sequences have been implemented and are currently available, none of them was provided as a robust tool for the LC delineation. During this work, the goal was to optimise existing sequences based on their parameters in order to define a standard protocol providing the maximum contrast for LC visualisation. Because of the key role of MT effects in contrast generation, two different types of sequences were investigated: the spoiled gradient echo sequence and the SPGR sequence including a MT saturation pre-pulse. First, the contrast was optimised based on an available SPGR sequence multi-compartment model and then validated through experiment. Second, the modelling and the optimisation of the contrast with SPGR sequence including a pre-saturation

MT pulse was realised. Unfortunately, the validation of the latter could not be achieved in the course of the internship realised at the Wellcome Centre for Human Neuroimaging (WCHN), UCL (London) due to restrictions imposed by the Covid-19 pandemic. However, the suggested results are discussed and put into perspective with the techniques currently used.

This thesis is divided in five different chapters. The first chapter aimed at describing the general background by reviewing theoretical notions considered during the work. Secondly, chapter two reports the methods for the optimisation of the SPGR sequence through simulation and validation of the model, and of the SPGR sequence with MT pre-pule with simulation. Results are then presented in the third chapter for both models investigated. The chapter four presents a critical analysis of the outcomes, while the limitations and the potential improvements of this project are mentioned emphasising the need of future work. Finally, this thesis concludes on the limitations of the study performed and the perspectives on the subject.

All the MATLAB codes developed during this project can be found in the following repository: `https://github.com/CyclotronResearchCentre/NeuromelaninImaging`

Chapter 1

Background

1.1 Locus cœruleus

This first background section is focused on the locus cœruleus, the biological structure of interest in this project. After having described its related anatomical and physiological properties, the current clinical interest for this nucleus in research is emphasised, particularly in the scope of neurodegenerative diseases. Challenges regarding its visualisation with MRI are subsequently discussed.

1.1.1 Anatomy and physiology

The locus cœruleus is a small elongated subcortical nucleus located in the brainstem region. More specifically, it is found along the lateral edge of the floor of the fourth ventricle in the pontine tegmentum. FIGURE 1.1 schematically represents this structure on a sagittal view of the brain (a) and through a 3-D reconstruction of the brainstem area (b) where the yellow dotted line highlights the position of the sagittal cut.

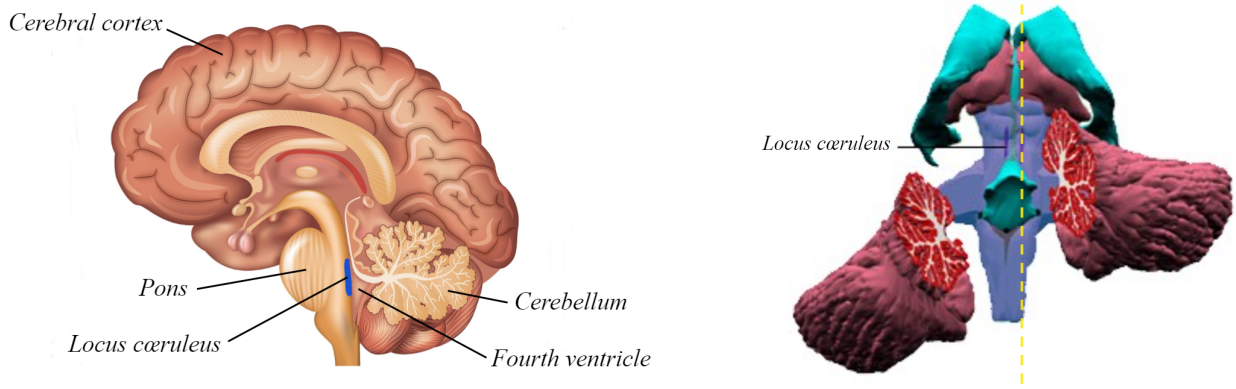

(a) Sagittal view (adapted from [33])

(b) 3-D reconstruction (adapted from [4])

Figure 1.1: Anatomical location of the locus cœruleus

A stereological study realised on 20 healthy human brainstems described the cylindrical shape of this structure with averages of 14.5 mm in length and 2.5 mm^2 in cross-section, dropping to 2 mm^2 in the central portion [21]. FIGURE 1.2 depicts the 3-D reconstruction of the LC of one individual from this cohort, allowing a better visualisation of the shape of the nucleus despite the high inter-subject

variability.

Figure 1.2: 3-D Image reconstruction of a human pair of locus cœruleus, shown in the coronal plane (adapted from [21])

Locus cœruleus is derived from the Latin translation of 'blue spot' and arises from its dark pigmented appearance identified through histological studies. This coloration comes from the neuromelanin (NM) molecule produced in this structure during the synthesis of noradrenaline (NA), a key neurotransmitter. In fact, the LC is the main source of noradrenaline in the brain comprising by itself half of the total noradrenergic cell population in the brain. LC neurons innervates numerous brain areas by releasing NA in the central nervous system and therefore regulating various anatomic and cognitive functions. It has been shown that LC neuronal activity varies considerably with functions such as arousal, attention, memory, pain and response to stress [6, 9, 11, 30]. In sum, despite its small size, this nucleus plays a significant role in the daily cognitive processes occurring in the brain.

1.1.2 Clinical interest

Through its multiple noradrenergic projections and the multitude of regulation processes in which noradrenaline is involved, the locus cœruleus is of strong interest in neuroscience. The LC is indeed thought to play a central role in many cognitive functions such as arousal, attention, learning, memory and decision making through its modulation of noradrenaline in the central nervous system [37]. However, its involvement in cognitive processes and its structure over the lifespan are not yet fully understood. The LC neuronal population seems to dependent on numerous factors as for instance the age, the sex and even the cognitive reserve [16]. More particularly, Liu et al. [29] described the age-related feature of the LC in healthy subjects as a quadratic relationship with a peak in the LC population occurring around 60 years old. These findings emphasise the complexity for characterising this structure in all generality.

In addition to its key neuromodulatory role in cognitive functions, studies have shown that a deterioration of the LC noradrenergic system was associated with various neurological disorders such as Alzheimer's disease, Parkinson's disease and multiple system atrophy [14, 32]. While the underlying mechanisms of these pathologies are still insufficiently defined, some studies assess that the *in vivo*

measurement of the LC integrity could be derived as a biomarker for the progression of such neurodegenerative disorders [9, 24, 40].

Therefore, improving our understanding of the role of the LC and thereby better characterising its microstructural organisation through its *in vivo* visualisation, are at present highly active areas of research.

1.2 Magnetic resonance imaging

Magnetic resonance imaging, more usually named MRI, is nowadays one of the most widely used medical imaging modalities mainly because of its high image quality and noninvasive features. The MRI invention dates back to the early 1970's when the chemist Paul C. Lauterbur considered to spatial encode the nuclear magnetic resonance (NMR) signal by using magnetic field gradients and thereby creating an image. This discovery marked the birth of nuclear magnetic resonance imaging. Yet, the *nuclear* denomination had a negative connotation in the general public's mind because of its association with nuclear radioactivity. However, unlike nuclear medicine imaging involving the use of radioactive substances, MRI signals arise from nuclear magnetic resonance properties of different tissues that is to say the spin behaviour of nuclei in an external magnetic field and is therefore a radiation-free technology. Nevertheless, this misleading 'nuclear' term was dropped in order to avoid any confusion.

First MRI scanners were installed in hospitals for clinical use in the early 1980's. Even since then, the scientific interest for this field was continuously growing through the development of new technologies and medical applications, improving each and every day our understanding of the anatomical and physiological functions of the body. Despite its relatively recent discovery, MRI is a powerful imaging technique used in most of classic clinical procedures mainly because of its high flexibility and its capacity to characterise a large range of tissue properties. This modality is nowadays recognised as one of the most important breakthrough of the century.

In the following sections, the theoretical aspects relative to the magnetic resonance imaging technique are developed. After setting the general context and reminding the basic principle of the modality, the contrasts mechanisms in MRI are developed. Finally, general sequences and pulse characteristics are presented.

1.2.1 Fundamentals [35]

1.2.1.1 Physical principles

Nuclear magnetic resonance is the underlying physical principle ruling the MRI technique. Like its denomination specifies, MRI is based on the evolution of nuclear spins in response to external magnetic fields. Nuclei of interest in MRI are hydrogen protons forasmuch as these are the most abundant atoms in the human body and as their non-zero spins provide them a magnetic moment. At a microscopic level and in the absence of an external B_0 magnetic field, spins are oriented randomly. Once placed in a strong external magnetic field, hydrogen spins are polarised and aligned to the B_0 direction around which they precess at the so-called Larmor frequency ω_0, such that $\omega_0 = \gamma B_0$ with γ the gyromagnetic ratio of the nuclei. Given the existence of two different levels of energy

for hydrogen atoms characterised as 'up' and 'down' and because there is a higher total number of spins 'up' than there is of spins 'down', a net longitudinal magnetisation M_z parallel to B_0 is generated. Note that while the spins are precessing at the same frequency, their phase is random which explains the absence of net transverse magnetisation M_{xy} for this configuration. The condition required for the existence of a transverse magnetisation is met when a perturbing magnetic field B_1 is applied at a frequency ω_{RF} matching the Larmor frequency such that $\omega_{RF} = \omega_0$ leading to the resonance phenomenon. This disturbance aims at tipping the initial magnetisation M_0 through the transverse plane where spins are now precessing at the same frequency and with the same phase, creating a macroscopic magnetisation $\mathbf{M(t)} = (M_x(t), M_y(t), M_z(t))$ perpendicular to the main field B_0 and consequently a detectable magnetic resonance (MR) signal.

1.2.1.2 Hardware

MRI scanners exists in various sizes and shapes but are always composed of the following building blocks: the main magnet, a set of coils and the electronic circuitry including the visualisation console. The most important component of this machine is the cylindrical magnet producing the strong static magnetic field B_0 in the bore of the scanner. As illustrated by FIGURE 1.3, different coils are then placed in a concentric arrangement within this magnet and can be distinguished in two categories: the gradient coils and the radiofrequency (RF) coils.

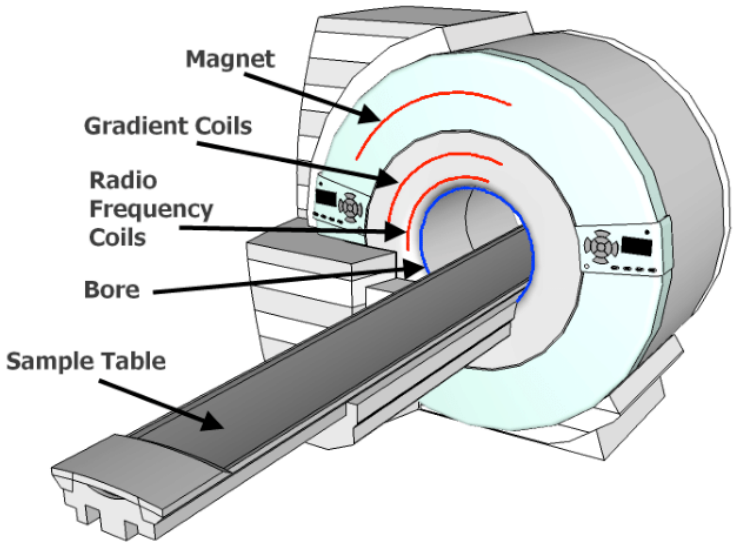

Figure 1.3: Schematic diagram of an MRI machine (reproduced from [25])

Usually, gradient coils are a combination of three orthogonal sets of coils, each oriented along a particular direction ($\hat{x}$, $\hat{y}$, $\hat{z}$) and producing a variable magnetic field such as the resulting main magnetic field in the bore is equal to

$$\mathbf{B} = (B_0 + G_x x + G_y y + G_z z)\hat{z}$$

In this expression, G_x, G_y and G_z are the gradient amplitude respective to each direction while it was assumed that gradients were switched on simultaneously [35]. Consequently, the magnitude of the main magnetic field B_0 is temporary modified as a function of the position enabling to spatial

encode the MR signal in the *k-space*. The generation and the recording of this MR signal results from the radiofrequency coils which are either used as transmitter or receiver coils, and sometimes handle both functions simultaneously. When acting as a transmitter, RF coils generate a time-varying B_1 magnetic field perpendicular to and up to 10^5 times smaller than the main B_0 field. This time, the RF magnetic field is not transmitted in a continuous way but through short pulses, called radiofrequency pulses in the order of the millisecond. Through the process of resonance, the net magnetisation of spins changes and an MR signal is detectable. Receiver RF coils catch the oscillating net magnetic flux coming from excited spins which in turn induce current according to Faraday's Law of induction. This current is then processed in order to extract relevant information and reconstruct the MR signal.

1.2.1.3 Relaxation times

After being excited by different pulses, tissue composing spins tend to go back to their equilibrium state through independent relaxation processes [10]. In fact, the interaction of spins with each others and with the external environment causes at a macroscopic level the magnetisation **M** to go back to its equilibrium configuration with time. The reestablishment of the thermal equilibrium $\mathbf{M} = M_0\hat{z}$ aligned to the magnetic field $\mathbf{B_0} = B_0\hat{z}$ is characterised by the relaxation times constants T_1 and T_2 as illustrated by FIGURE 1.4.

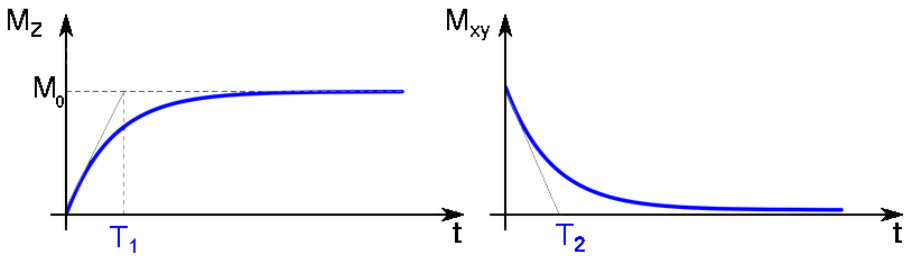

Figure 1.4: Representation of T_1 and T_2 relaxation times (adapted from [18])

In this representation, the longitudinal relaxation time T_1 is the time required for the regrowth of the longitudinal magnetisation M_z to 63% of its initial value M_0. Similarly, T_2 is the transverse relaxation time accounting for the decay of the transverse components M_x and M_y induced by the dephasing of spins. T_2 is defined as the time post excitation after which the transverse magnetisation has decreased to 37% of its initial value.

In addition to this dephasing phenomenon caused by local magnetic field inhomogeneities from spin-spin interactions and represented by T_2 time constant, the magnetic field inhomogeneity also accentuates this decay and therefore shortens the apparent transverse relaxation time constant. Defining T_2' as the relaxation time constant accounting for the external magnetic field inhomogeneities, the apparent relaxation time constant T_2^* is thereby given by following equation :

$$\frac{1}{T_2^*} = \frac{1}{T_2} + \frac{1}{T_2'} \tag{1.1}$$

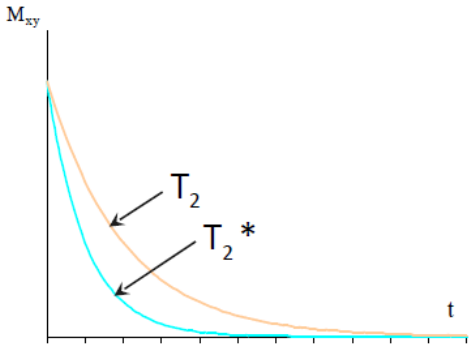

Figure 1.5: Representation of T_2^* and T_2 decays (reproduced from [7])

1.2.2 Contrast in MRI

1.2.2.1 Magnetisation transfer imaging

The magnetisation transfer mechanism relies on the heterogeneity of macromolecular tissue composition. The composition of brain tissues is complex but the use of simplified models enables the segregation of the proton environments into two distinct compartments: the bound pool and the free pool. In fact, each imaging voxel is considered as divided in two different pools. Regarding notations used during this project, tissue compartments were labelled as *a* and *b*, with compartment *b* being the smallest one and referred to as the bound pool. Compartment *a* corresponds to the free pool. In this context, the free pool includes the intra-cellular, extra-cellular and myelin water as well as the cerebrospinal fluid (CSF). The protons composing the free pool are characterised by a higher mobility than those in the bound pool. FIGURE 1.6 schematically represents the equilibrium configuration of these two pools in one imaging voxel which highlights the heterogeneity existing at such microscopic level and the complexity of the inherent macroscopic description. In this example, spins are modelled by arrows. Following this notation, the bound pool delineated by the orange area is composed of three hydrogen spins bound to the macromolecule while the free pool has four water molecules from which eight spins arise, all of them contributing to the MR signal.

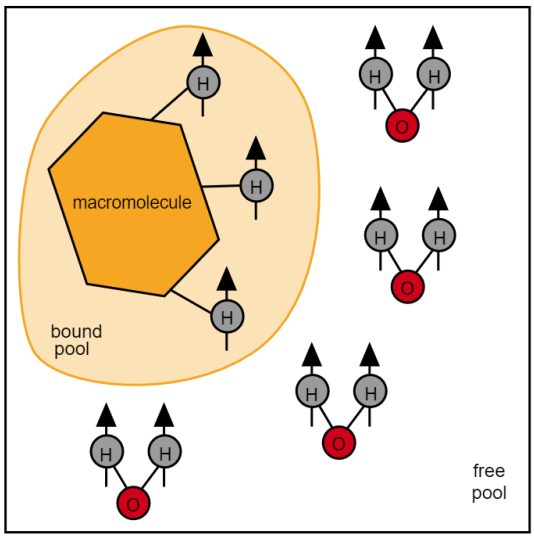

Figure 1.6: Simplified pools representation within one imaging voxel (adapted from [19])

The major difference between these pools lies in their spectral characteristics as illustrated in FIGURE 1.7. The free pool has a very narrow spectral line ranging from 10 to 100 Hz while the spectral line of the bound pool extends from 10 to 50 kHz. Furthermore, the transverse relaxation time constant in the free pool is quite long with T_2 times in the region of tens of milliseconds or larger and is very small in the bound pool with T_2 values of the order of microseconds [19]. Because of the microscopic scale and the extremely short relaxation time T_2 in the bound pool, the latter cannot be directly visualised through classic MRI sequences. In practice, the relaxation time decays so rapidly that it is impossible to record the MR signal arising straight from this pool which is then said to be invisible.

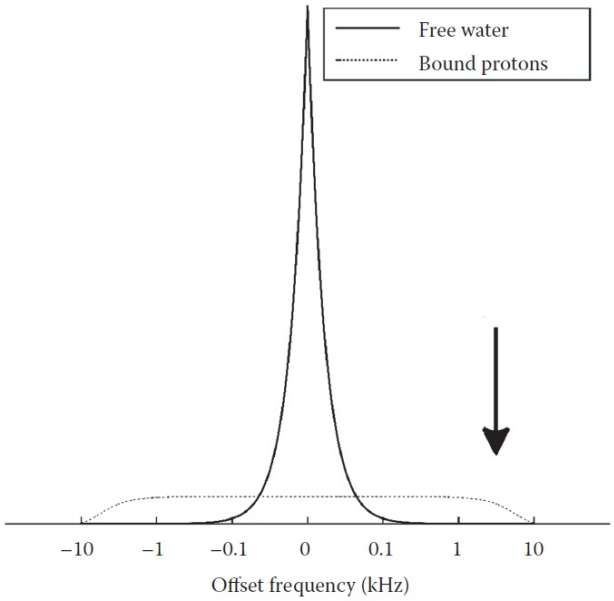

Figure 1.7: Schematic representation of the frequency spectrum in the bound and free pools. The arrow denotes the off-resonance RF excitation (reproduced from [13])

Magnetisation transfer imaging takes advantages of the much larger range of frequencies of the bound pool to selectively perturbed this compartment by an off-resonance pulse at $\omega \neq \omega_0$ which is represented by an arrow in FIGURE 1.7. Through this selective saturation process, the free water pool is effectively unaffected by the off-resonance pulse because of its narrow on-resonance spectrum.

The spins behaviour in one imaging voxel after this MT pulse is represented in FIGURE 1.8 following the same notations as previously and where an arrow pointing downwards represents a saturated spin. As a consequence of this off-resonance saturation pulse, the spins will tend to their equilibrium state. To do so, saturation is transferred from the bound pool to the free pool through different exchange mechanisms such as chemical exchange and cross-relaxation between pools. Because of this magnetisation transfer, the free pool becomes partially saturated which will alter the MR signal. The directly invisible bound pool is therefore made indirectly visible through its impact on the free pool.

Pools are represented in FIGURE 1.8a right after the selective saturation of the bound pool with the off-resonance pulse. The bulk magnetisation coming from the bound pool demonstrates a spin schematically pointing downwards reflecting the saturation effect. The equilibrium situation reached through magnetisation exchange from the bound pool to the free pool due to dipole-dipole interactions is illustrated in FIGURE 1.8b.

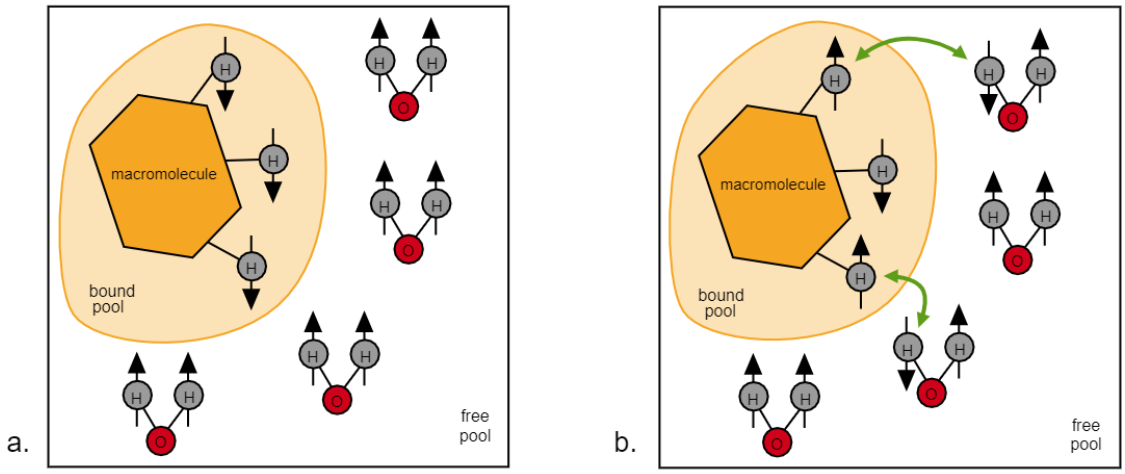

Figure 1.8: a. Selective saturation of the bound pool with an off-resonance MT pulse. b. Cross-relaxation phenomenon between pools resulting from the selective saturation of the bound pool at the level of one imaging voxel (adapted from [19])

The exchange phenomenon refers to as the transfer of magnetisation between the two pools and can be summarised by a directional exchange rate, i.e. k_{ba} indicating the exchange rate from the bound to the free pool according to previous notations. At the chemical equilibrium, exchange rates are defined such as:

$$k_{ba}\mathrm{M}_b = k_{ab}\mathrm{M}_a \tag{1.2}$$

where k_{ab} is the exchange rate from the free to the bound pool and M_a and M_b are the equilibrium magnetisations of free and bound pools respectively such that the concentration in each pool is fixed.

These pool-specific magnetisations M_a and M_b are referred to as the amount of free and bound protons composing each pool respectively. From these quantities, the compartments a and b can also be described by their fractional size f_a and f_b, respectively. The fractional size of the bound pool represents the relative amount of magnetisation in this pool compared to the overall magnetisation such as:

$$f_b = \frac{\mathrm{M}_b}{\mathrm{M}_a + \mathrm{M}_b} \tag{1.3}$$

and is often referred to as the bound pool fraction. By definition, the sum of both compartment sizes is unity:

$$f_a + f_b = 1 \tag{1.4}$$

Another way of quantifying the size of the compartments is given by the pool size ratio (PSR). The PSR is defined as the ratio of the equilibrium magnetisations between compartments b and a such as:

$$\mathrm{PSR} = \frac{\mathrm{M}_b}{\mathrm{M}_a} \tag{1.5}$$

In other words it represents the proportion of macromolecular bound protons relative to free water protons. According to the previous definition of the fractional size of the bound pool in EQUATION (1.3), the PSR can easily be linked to the expression of f_b as follows:

$$f_b = \frac{\mathrm{PSR}\cdot\mathrm{M}_a}{\mathrm{M}_a + (\mathrm{PSR}\cdot\mathrm{M}_a)} = \frac{\mathrm{PSR}}{1+\mathrm{PSR}} \tag{1.6}$$

Depending on the degree of coupling between the free and the bound pools, their respective fractional sizes f_a and f_b and their exchange rates k_{ab} and k_{ba}, the free pool becomes partially saturated. Therefore, the signal obtained from traditional MRI sequence with MT preparation pulse would manifest as a reduction in the observable signal amplitude of the free pool and result in the enhancement of the overall contrast between voxels that have different fractional bound pool sizes as illustrated by FIGURE 1.9 [20].

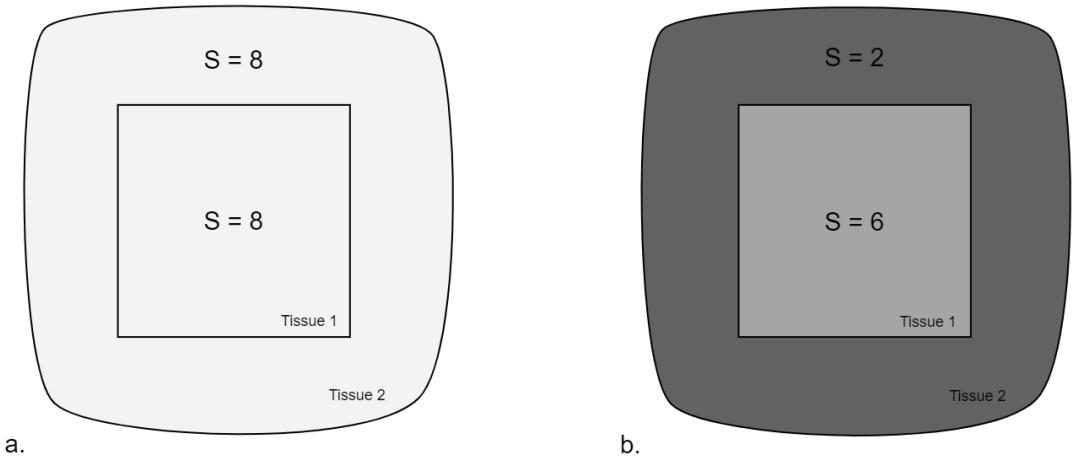

Figure 1.9: Contrast enhancement achieved with magnetisation transfer between two tissue types with different bound pool fractions. Signals configuration a. before and b. after the application of the MT pre-pulse (adapted from [19])

1.2.3 Sequences in MRI

An MRI sequence defines how the components of the MRI system are altered in time to manipulate the magnetisation and produce an image. Typically, it is composed of radiofrequency pulses and gradients waveforms allowing the application of different strategies for data acquisition and image reconstruction. The specification of the sequence parameters is a crucial concern in MRI since it dictates the type of data acquired. In this section, the characteristics of RF pulses are first described. Then, the spoiled gradient echo and the spoiled gradient echo with MT preparation pulse sequences used in the scope of this project are presented.

1.2.3.1 Radiofrequency pulses characteristics

Radiofrequency pulses are one of the main building blocks of MRI pulse sequences, with gradients waveforms and data acquisition. An RF pulse is characterised by its flip angle α_{RF}, i.e. the angle by which the magnetisation will be tilted after the application of the pulse, and its energy W_P. Both are determined by the amplitude of the B_1 magnetic field, the shape and the duration of the pulse τ_{RF}. RF pulses are played out in time and have a corresponding frequency bandwidth that dictates for which environments the resonance condition $\omega_{\mathrm{RF}} = \omega_0$ will be met. A pulse can then be characterised by the product of its bandwidth and duration, referred to as the bandwidth-time product (BWT). In turns, the energy of the pulse defines the signal absorption rate (SAR) computation of the subject undergoing

an MRI scan. For safety purposes, this parameter is subject to a maximum value which subsequently defines limitation on the RF pulse energy.

While many different RF pulse shapes are used in MRI sequence design, the focus will be on the rectangular, sinc and Gaussian pulse shapes since these are the ones encountered during this work [8, 12].

In a general case, the energy and the flip angle associated to an RF excitation pulse are described by the following expressions:

$$\alpha_{\mathrm{RF}} = \gamma \int_0^{\tau_{\mathrm{RF}}} B_1(t)dt \tag{1.7}$$

$$W_p = \int_0^{\tau_{\mathrm{RF}}} B_1^2(t)dt \tag{1.8}$$

with

- α_{RF} the flip angle of the RF pulse;
- γ the gyromagnetic ratio;
- τ_{RF} the RF pulse duration;
- B_1 the amplitude of the RF magnetic field;
- W_P the energy of the RF pulse.

▸ Rect **pulse**

A rectangular pulse is shaped as a rect function in the time domain. Usually brief, the equivalent of this rect pulse in frequency domain is a sinc function. The rect pulse presents a very broad spectrum in the frequency domain preventing to perform slice-selective excitation but rather whole brain acquisition, giving it the adjective of non-selective pulse.

A rect pulse is defined by:

$$B_1(t) = B_{1,r}\mathrm{rect}\left(\frac{t}{\tau_{\mathrm{rect}}}\right) \tag{1.9}$$

with $\mathrm{B}_{1,r}$ the peak amplitude of the pulse and τ_{rect} its duration as represented in FIGURE 1.10.

The flip angle and the energy of this rect pulse found by the integration of EQUATIONS (1.7) and (1.8) are given by:

$$\alpha_r = \gamma B_{1,r}\tau_{\mathrm{rect}} \tag{1.10}$$

$$W_{P,r} = B_{1,r}^2\tau_{\mathrm{rect}} \tag{1.11}$$

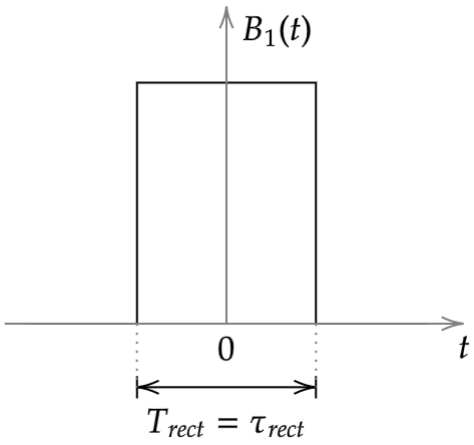

Figure 1.10: Theoretical representation of a rect pulse

▸ Sinc **pulse**

The sinc pulse has the shape of a truncated sinc function as represented in FIGURE 1.11. In an ideal configuration, the pulse would be defined infinitely in the time domain. According to the Fourier transform, the corresponding excitation profile in frequency domain would therefore have the shape of a perfect rect function. However, it is necessary to truncate this pulse in order to use it in practice which results in a non-ideal rectangular excitation profile caused by the Gibbs phenomenon in the frequency domain. FIGURE 1.11 illustrates this phenomenon for two different sinc pulses with a bandwidth-time-product of 6 and 10.

From the latter figure, it can be seen that the higher the number of side lobes of a sinc pulse, the more the overshoots decrease in the frequency domain. This criteria is crucial in RF pulses design and is expressed in terms of bandwidth-time-product. The BWT is equal to the number of zero crossing of the pulse envelope on each side of the central lobe before truncation. Therefore, the higher the BWT, the more precise the slice profile.

According to the schematic representation of the sinc pulse envelope and its associated parameters in FIGURE 1.12, the time evolution of the B_1 amplitude is theoretically given by:

$$B_1(t) = B_{1,s}\mathrm{sinc}\left(\frac{\pi t}{\tau_{\mathrm{sinc}}}\right) \tag{1.12}$$

where $B_{1,s}$ is the B_1 peak amplitude of the sinc pulse and τ_{sinc} its characteristic time constant.

The total duration of the pulse is denoted by T_{sinc} while τ_{sinc} represents the time between the maximum B_1 amplitude of the pulse, in $t = 0$, and the first zero crossing with the x-axis. From the previous definition of the bandwidth-time-product, the following expression can be derived:

$$T_{\mathrm{sinc}} = \mathrm{BWT} \cdot \tau_{\mathrm{sinc}} \tag{1.13}$$

Finally, the integration of EQUATIONS (1.7) and (1.8) gives as results:

$$\alpha_s = \gamma B_{1,s} \tau_{\mathrm{sinc}} \tag{1.14}$$

$$W_{P,s} = B_{1,s}^2 \tau_{\mathrm{sinc}} \tag{1.15}$$

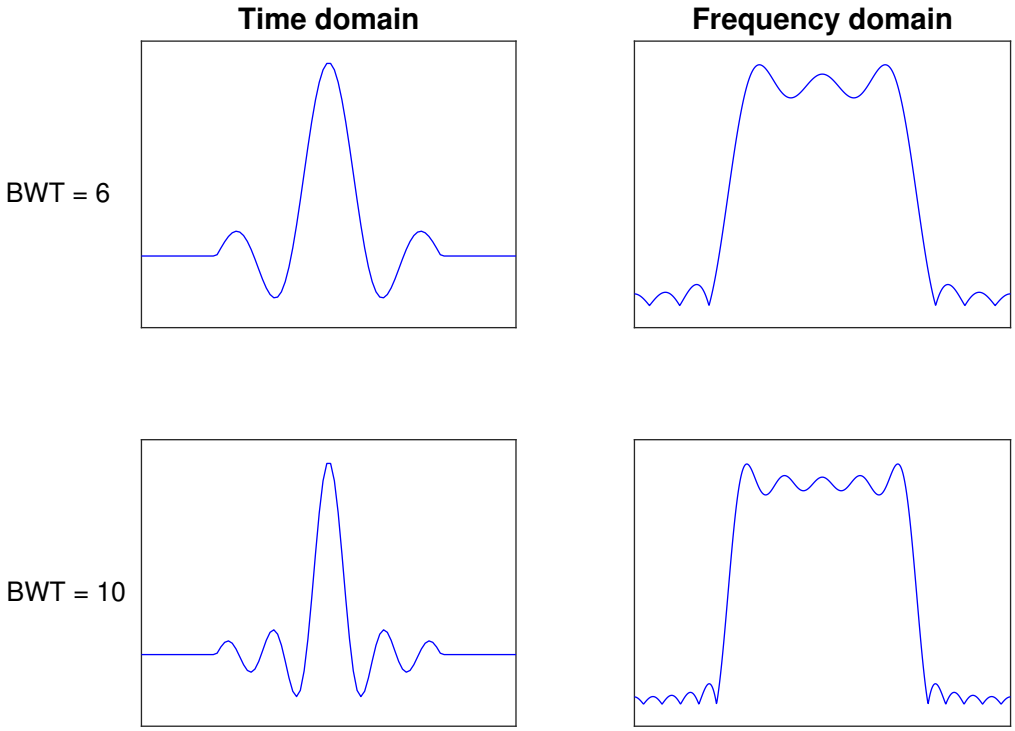

Figure 1.11: Sinc excitation pulses with a bandwidth-time-product of 6 and 10 in time domain and their corresponding slice profile

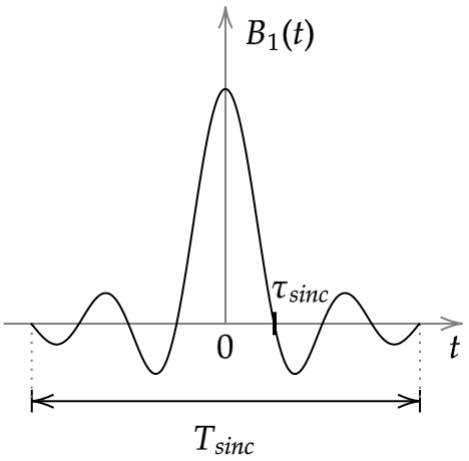

Figure 1.12: Theoretical representation of a sinc pulse

From these equations, the impact of the BWT of the pulse is highlighted. Indeed, for a given pulse duration T_{sinc}, increasing the BWT involves a decrease in the characteristic time constant τ_{sinc}. The same flip angle α_s is reached if a higher B_1 magnetic field is delivered during the scan. For that reason, it is important to pay attention to technical limitations of scanners when defining a pulse since a large BWT is not achievable in practice.

▸ Gaussian pulse

Depending on the application, Gaussian pulses can be useful. The frequency profile of such a pulse is a Gaussian function itself. This kind of pulse is often employed when dealing with MT sequence with off-resonance saturation pulses. Given the modelling presented in FIGURE 1.13, the envelope of such a Gaussian pulse is described as:

$$B_1(t) = B_{1,g} e^{-t^2/(2\tau_{\text{gauss}}^2)} \tag{1.16}$$

with $B_{1,g}$ the peak B_1 amplitude of the Gaussian pulse and τ_{gauss} its characteristic time constant.

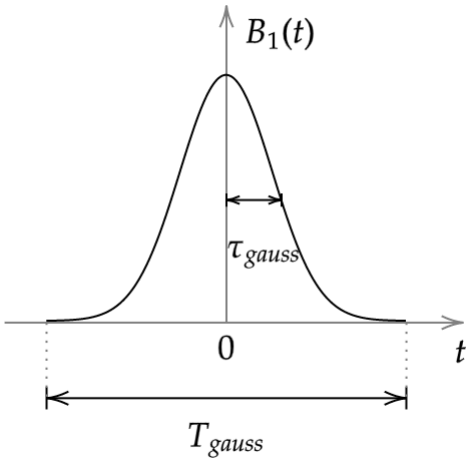

Figure 1.13: Theoretical representation of a Gaussian pulse

In this representation, τ_{gauss} is defined such that the pulse decays at e^{-1} of its peak B_1 amplitude in $t = \sqrt{2}\tau_{\text{gauss}}$.
According to Bernstein development [8], the Gaussian pulse is assumed to be non zero only within the interval $t \in [-\frac{T_{\text{gauss}}}{2}, +\frac{T_{\text{gauss}}}{2}]$ where $\frac{T_{\text{gauss}}}{2}$ is the time at which the amplitude of the Gaussian pulse undergoes 60dB attenuation. The pulse width is therefore assumed to be:

$$T_{\text{gauss}} \approx 7.434 \cdot \tau_{\text{gauss}} \tag{1.17}$$

Considering the previous notations, the flip angle and the energy are obtained by solving the EQUATIONS (1.7) and (1.8) which gives

$$\alpha_g = \sqrt{2\pi}\gamma B_{1,g}\tau_{\text{gauss}} \tag{1.18}$$

$$W_{P,g} = \sqrt{\pi} B_{1,g}^2 \tau_{\text{gauss}} \tag{1.19}$$

▸ **Summary**

From previous developments, it has been shown that pulse characteristics vary depending on the shape of the pulse. In RF pulse design, restrictions are set on the B_1 amplitude from a safety perspective to protect the participant. An additional limit exist by virtue of the fact that a coil can only produce a B_1 magnetic field of a finite amplitude. TABLE 1.1 summarises the different expressions of total duration, pulse envelope, flip angle and energy respective to each pulse shape.

Pulse shape	Pulse duration, T	Pulse envelope, $B_1(t)$	Flip angle, α_{RF}	Energy, W_P
rect	τ_{rect}	$B_{1,r}\text{rect}\left(\frac{t}{\tau_{\text{rect}}}\right)$	$\gamma B_{1,r}\tau_{\text{rect}}$	$B_{1,r}^2\tau_{\text{rect}}$
sinc	$\text{BWT}\cdot\tau_{\text{sinc}}$	$B_{1,s}\text{sinc}\left(\frac{\pi t}{\tau_{\text{sinc}}}\right)$	$\gamma B_{1,s}\tau_{\text{sinc}}$	$B_{1,s}^2\tau_{\text{sinc}}$
gauss	$7.434\cdot\tau_{\text{gauss}}$	$B_{1,g}e^{-t^2/(2\tau_{\text{gauss}}^2)}$	$\sqrt{2\pi}\gamma B_{1,g}\tau_{\text{gauss}}$	$\sqrt{\pi}B_{1,g}^2\tau_{\text{gauss}}$

Table 1.1: Rect, sinc and gauss pulses characteristics

1.2.3.2 Spoiled gradient echo sequences

One of the basic pulse sequences widely used in MRI is the gradient echo (GRE) sequence. The main particularity of this sequence is the successive application of dephasing and rephasing gradient fields aiming at creating a transverse magnetisation and subsequently an MR signal. In the scope of this project, a specific type of GRE sequences was considered: the spoiled gradient echo sequence.

The SPGR sequence relies on the full destruction of the transverse magnetisation at the end of each repetition period. This is achieved by gradient and radiofrequency spoiling. The gradient spoiling consists in playing a gradient at the end of the repetition time (TR) with a large moment that induces decoherence between constituent spins and a reduction in magnetisation. RF spoiling involves the variation of the B_1 magnetic field phase, that is to say of the RF pulse, across repetitions. The most common implementation of this spoiling strategy is a quadratic incrementation such as:

$$\phi_n = \phi_{n-1} + n\phi_0 \qquad \text{with } n = 1,2,3,... \tag{1.20}$$

where ϕ_n is the phase of the B_1 field for the n^{th} RF pulse [8] and ϕ_0 is the RF spoiling increment.

The SPGR sequence can schematically be represented by the configuration depicted in FIGURE 1.14. The sequence is described for one repetition period TR during which excitation, signal acquisition and spoiling are realised. First, the spins excitation is achieved by an RF pulse with a flip angle of α_{RF} degrees and a duration of T_{RF}. A set of gradients is subsequently applied inducing a dephasing and then a rephasing between those. As a result, a visible MR signal is recorded at the echo time TE through gradients readout. Finally, the RF spoiling is achieved before the end of the repetition period. These successive events are then repeated along the duration of the acquisition period.

Note that this configuration depicts an SPGR sequence with an unique echo but the technique can be extended to the acquisition of several echoes. In that case, the acquisition strategy is qualified of multi-echo SPGR sequence.

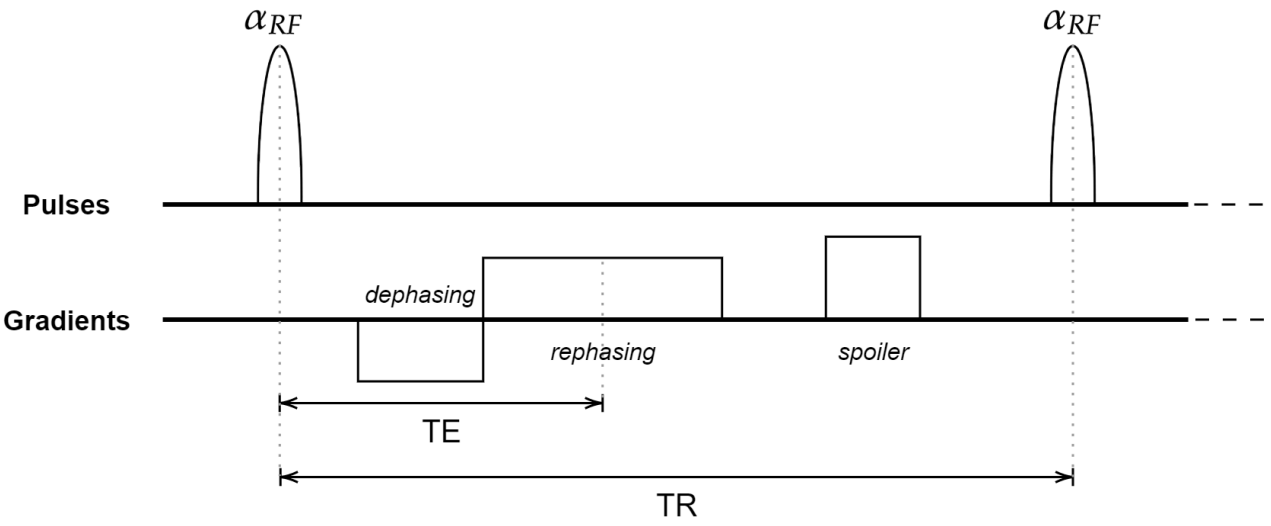

Figure 1.14: Schematic representation of the classic SPGR sequence

1.2.3.3 SPGR with MT pulse

When performing magnetisation transfer imaging, the application of an off-resonance saturation pulse prior to the excitation RF pulse is required. The SPGR with MT pulse simply consists in the SPGR sequence previously described with the prior application of an MT saturation pulse characterised by its flip angle α_{MT}, its duration T_{MT} and its off-resonance frequency f_{MT}. A spoiler gradient is also added between the saturation and the excitation pulses in order to disrupt any undesired magnetisation. During this period, exchanges occur between respective pools of tissues, partially saturating the free pool. The excitation pulse is subsequently applied for acquiring the MR signal in TE. After that the transverse magnetisation is fully destroyed by the RF spoiler, a new repetition period may start.

The main components of this sequence are schematically represented in FIGURE 1.15 with a unique echo. As previously, this configuration can easily be extended to a multi-echo SPGR sequence with MT pre-pulse.

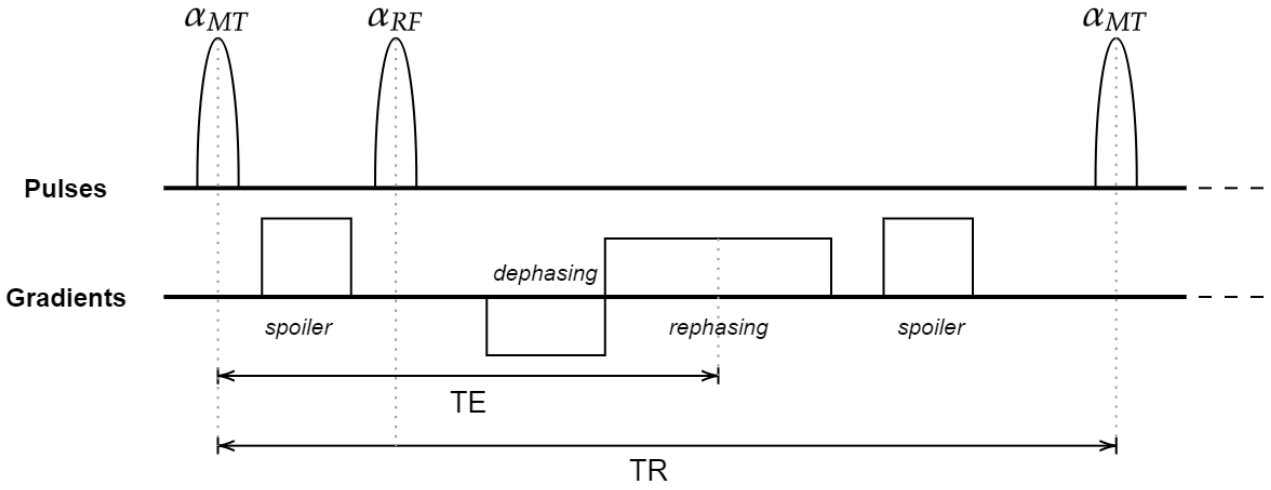

Figure 1.15: Schematic representation of the SPGR sequence with MT pre-pulse

The optimisation of MRI sequences and of the resulting signals is therefore ruled by the definition of its constituents. The precise determination of the pulses characteristics and the various timings involved in the acquisition strategy are crucial to optimise.

1.3 Locus cœruleus visualisation with MRI

The visualisation of the locus cœruleus with MRI techniques is not straightforward. First, the size of this nucleus dictates the requirement for high resolution images. Current MR scanners generally allow such spatial resolution but the impact of the noise is thereby increased, making the targeting of the LC even more complex. Second and of main concern, the contrast mechanisms inherent to this tissue type are poorly understood.

1.3.1 Existing sequences

The visualisation of the locus cœruleus with MRI is suggested by the presence of neuromelanin, this dark pigmented macromolecule and by-product of the noradrenaline synthesis. So-called neuromelanin sensitive sequences have previously been used to visualise the LC but the exact mechanisms by which the contrast is generated remain unclear [38]. In fact, the LC is a complex structure and its tissue properties are insufficiently characterised. In such sequences, the LC appears as a hyper-intense spot on the edges of the fourth ventricle as pointed out by yellow arrows in FIGURE 1.16.

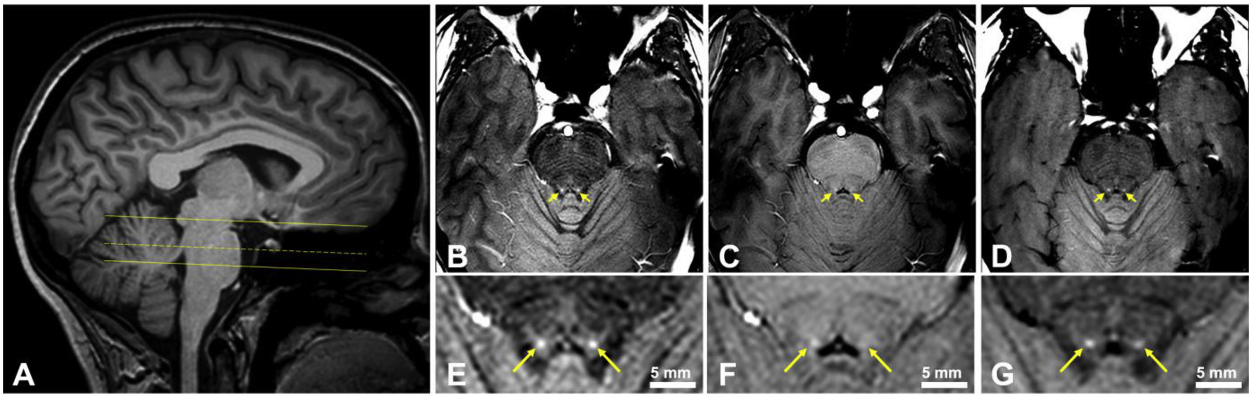

Figure 1.16: Visualisation of the locus cœruleus. A: T_1-weighted image. B, E : MT-weighted images acquired with MT prepared SPGR sequences. C, F: Reference SPGR image without MT weighting. D, G: T_1-weighted images acquired with 2D multi-slice TSE. The yellow arrows indicate the location of the LC (reproduced from [42])

The visualisation of this structure has been realised through different sequences primarily: multi-slice turbo spin echo (TSE) and gradient echo sequences. While T_1-weighted acquisition schemes were used, the slice selective nature of the acquisitions led to incidental MT effects that have complicated the interpretation of the key contrast mechanism underlying LC visualisation [38]. These MT effects are nowadays thought to be the main source of contrast in the LC [36]. LC imaging was also performed through MT-weighted gradient echo sequence with the application of specific MT preparation pulses prior to the excitation. The latter method reported improved performances in terms of LC visualisation [15].

FIGURE 1.16 depicts the different images acquired with such sequences aiming at visualising the LC. In the axial view, MT-weighted images acquired through GRE MT-prepared sequences (B, E) show significant improvement in the contrast compared to the classic multi-slice TSE acquisition (D, G). Furthermore, these results highly suggest the key role of MT effects in contrast generation seeing the decrease in signal intensity in the LC through GRE sequences without MT-prepared pulses (C, F) [42].

Therefore, sequences implying MT effects, either incidental or direct, have shown to provide a good visualisation of the LC. In order to effectively determining through which sequence parameters the contrast in the LC region is optimised, a better understanding of the LC structure mechanisms and tissue-dependent parameters is required.

1.3.2 Available LC parameters

Currently, there is limited quantitative MR information available in literature about relaxation and exchange properties of the LC. Watanabe et al. [46] report T_1 relaxation times of 1.18 ± 0.13 s, and T2 relaxation times of 95.6 ± 4.2 ms at 3T. Also at 3T, Trujillo et al. [42] report T_1 values of 1.579 ± 0.262 s. This study used a range of different off-resonance pulses (at different frequencies, sampling the so called z-spectrum [44]) to additionally explore the PSR, for which they report a value of 0.09 ± 0.009 within the LC.

From EQUATION (1.6), the value of the bound pool fraction in the LC is given by:

$$f_b = \frac{0.09}{1 + 0.09} = 0.0826 \tag{1.21}$$

FIGURE 1.17 depicts the MT-weighted image (A, D), the PSR (B, E) and the T_1 map (C, F) in the LC region relative to these results.

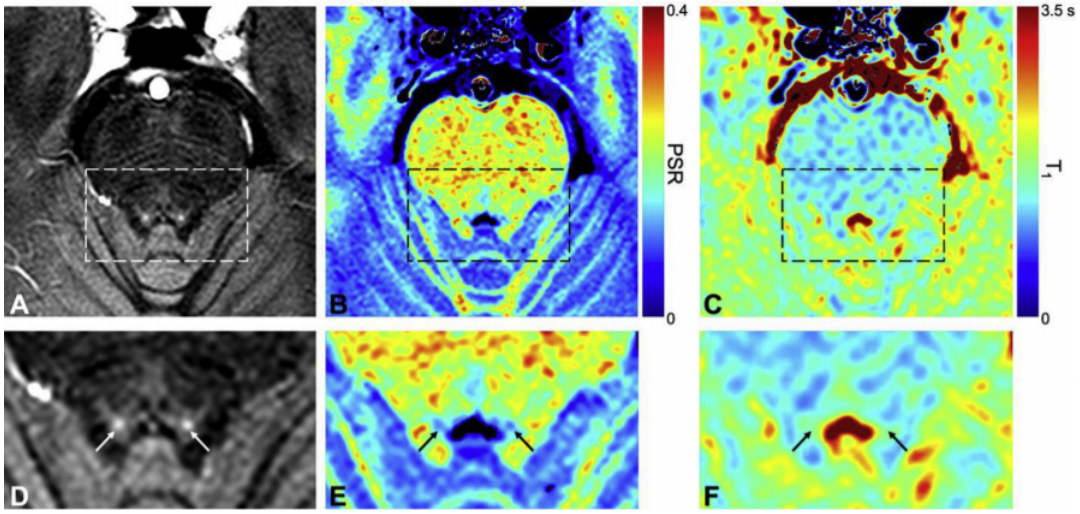

Figure 1.17: (A) Axial MT-weighted image at the level of the LC. (B) PSR map. (C) T_1 map. The area around the LC indicated by the dashed rectangle is magnified in (D), (E) and (F) respectively. The arrows indicate the location of the LC. (Reproduced from [42])

The MT-weighted image (A) shows the LC indicated by arrows as hyper-intense spots on the edges of the fourth ventricle. The fact that the LC appears bright indicates that the MT-related decrease in signal intensity is greater in the surrounding tissue than within the LC, suggesting a larger pool size ratio in the surroundings than within the LC as captured by the PSR map (B).

TABLE 1.2 summarises the relevant MR parameter values reported in literature for the characterisation of the LC and the corresponding study specifications realised on n subjects.

	n	Age	T_1 (s)	T_2 (s)	f_b	k_{ba} (Hz)
Watanabe et al., 2019	6	31.5 ± 7.5	1.18 ± 0.13	0.096 ± 0.004	/	/
	6	28.5 ± 2.3	1.02 ± 0.09	0.091 ± 0.010	/	/
Trujillo et al., 2019	26	41 ± 19.1	1.58 ± 0.26	/	0.0826	12.5

Table 1.2: Tissue-dependent parameter values for the LC reported in literature [42, 46]

Through these results, the lack of available and reliable information about the LC properties is highlighted. Furthermore, when comparing T_1 values obtained in both papers, a significant difference can be noticed, which makes the interpretation and the use of these values hard to confirm with strong confidence. The potential sources of discrepancies include the acquisition schemes and cohort characteristics such as age.

1.4 Aims of the thesis

The visualisation of the locus cœruleus is of main concern in neuroscientific research given its important involvement in neurodegenerative diseases. In opposition to its significance in numerous cognitive processes, the characterisation of this nucleus and the inherent contrast mechanisms are still insufficiently understood. Magnetisation transfer effects, which is presumably the major source of contrast in this structure, is based on the tissue representation as a two-compartment model with exchanges. For a few years, MRI takes advantages of this phenomenon to visualise the LC. However, targeting a structure that is poorly characterised is challenging. Besides optimising the contrast between the LC and its surroundings with SPGR sequence, one of the underlying goal of this thesis is the improvement of our knowledge about the locus cœruleus properties. The following work is provided as initial tool for better understanding the contrast mechanisms in the LC.

Chapter 2

Methods

This chapter describes the methods used in this project. Since the MT effect seems to drive the contrast in the LC we focused on the optimisation of the SPGR sequence with and without off-resonance pre-pulse while accounting for the MT effects introduced by both the excitation and dedicated MT pre-pulse if present. Consequently, this chapter is divided in two main sections. First, the focus is put on the optimisation of the SPGR sequence where simulations are performed and the resulting model is validated. Second, the optimisation of the SPGR sequence with a MT preparation pulse is investigated through simulations.

2.1 Optimisation of SPGR sequence: simulation and validation

This section details the general procedure applied when optimising the SPGR sequence for LC visualisation. Firstly, the simulations performed are described together with the used model parameters. Then, the procedure for the data acquisition is given. Afterwards, the description of the image processing requirements is presented. The last part of this section discusses the methods employed for contrast quantification and in a further extend model validation.

2.1.1 Simulations

Simulations were performed in MATLAB with the code `Simu_SPGR.m` based on the extended phase graph (EPG) formalism, and more particularly through the extension of the EPG framework to multi-compartment systems accounting for magnetisation transfer and exchange as developed by Malik et al. [31]. From this so-called EPG-X approach, the already implemented `EPGX_GRE_MT.m` function was used for simulating spoiled gradient echo sequences in a two-compartment model considering exchange.

2.1.1.1 EPG-X framework

The EPG formalism is a highly effective tool commonly used for modelling MR signals acquired through various MRI sequences. This method basically relies on solving the Bloch equations in the Fourier domain [48].

The purpose of the EPG-X model is to improve the characterisation of complex biological tissues through its coupled two-compartment model behaving like two distinct single-compartment EPG models interacting with each other through magnetisation transfer and exchange processes. Within

this model, the saturation of the bound pool by the RF pulse is described by the saturation rate $\overline{W(f_z)}$ proportional to the RF pulse energy and to the absorption lineshape $G(f_z)$ in this compartment [23]. The latter is defined as follows:

$$\overline{W(f_z)} = \frac{\pi\gamma^2}{\mathrm{T_{RF}}} \int_0^{\mathrm{T_{RF}}} B_1^2(t)\, dt\, G(f_z) \tag{2.1}$$

where $\mathrm{T_{RF}}$ is the RF pulse duration, $\mathrm{B_1(t)}$ is the pulse amplitude, $G(f_z)$ is the absorption lineshape and f_z is the off-resonance frequency of the RF pulse. The absorption lineshape is defined by a Super-Lorentzian function and considered at the on-resonance frequency $f_z = 0$ because of the absence of saturation pulse in this configuration [22]. This singular value was computed through the extrapolation of the Super-Lorentzian function at the on-resonance frequency by assuming $\mathrm{T}_{2,b} = 12\,\mu\mathrm{s}$, which corresponds to $G(0) = 15.1\,\mathrm{Hz}$, the default value used by Malik et al. [31].

The EPG-X framework requires the specification of several parameters that can be divided in two different categories: sequence-dependent or tissue-dependent.

2.1.1.2 Sequence-dependent parameters

The default SPGR protocol currently in place at the WCHN aiming at targeting the LC was used as a starting point for the simulations. The objective was to improve the contrast in the LC while maintaining the same acquisition time. For that reason the repetition time TR was fixed but a range of different values for the RF pulse characteristics were investigated. Note that a sinc pulse characterised by the EQUATION (1.13) was used to model the excitation. Given EQUATION (2.1), the flip angle α_{RF} and the energy W_P of the pulse are both required to assess the MR signal arising from MT effects. As previously explained and described by EQUATIONS (1.7) and (1.8), they can both be computed from the $\mathrm{B_1}$ peak amplitude and the characteristic time constant of the pulse type, τ_{RF}. Since these four parameters are linked together, only two of them were considered as free parameters within simulations: α_{RF} and τ_{RF}. The RF spoiling increment ϕ_0 as developed by EQUATION (1.20) was also investigated. These parameters were studied over dedicated ranges while keeping their value achievable in practice.

As a standard consideration, an existing $\mathrm{T_1}$-weighted protocol from the WCHN used for LC visualisation was examined. The sequence was defined with the following parameters:

- $\mathrm{TR} = 24.5\,\mathrm{ms}$;
- $\alpha_{\mathrm{RF}} = 21^\circ$;
- $\mathrm{T_{RF}} = 560\,\mu\mathrm{s}$;
- BWT= 6;
- $\phi_0 = 137^\circ$.

Because of the sinc shape of the RF pulse and the BWT set to 6, the corresponding characteristic time constant is equal to $\tau_{\mathrm{RF}} = \frac{560}{6} = 93\,\mu\mathrm{s}$ according to EQUATION (1.13). From the described sequence, the repetition time was fixed to $\mathrm{TR} = 24.5\,\mathrm{ms}$ in this project. In line with this protocol, the following ranging values of the three free parameters were tested:

- $\alpha_{\mathrm{RF}} \in [0.5\ 50]^\circ$, with intervals of 0.5°;

- $\tau_{RF} \in [10\ 1000]$ µs, with intervals of 10 µs;
- $\phi_0 \in [1\ 180]^\circ$, with intervals of 0.5°.

A further restriction was imposed on the B_1 amplitude, which was limited to 20 µT to ensure it could be achieved in practice given the hardware limitations. In fact, a maximum B_1 amplitude value of 28.27 µT was computed for the 3T Prisma scannerused during this project.

▸ Specifications

Another important consideration regarding the hardware was the efficiency of the B_1 magnetic field delivered by the scanner in the region of interest. This $B_{1,eff}$ factor accounts for the inhomogeneities in the B_1 magnetic field observed in practice and characterises the B_1 amplitude actually achieved. From data previously acquired at the WCHN with similar T_1-weighted sequence on the 3T Prisma scanner used for the experimentation part in this project, $B_{1,eff}$ was estimated in the LC region to 119.33%. This value was computed based on the B_1 efficiency map acquired through the multi-parametric mapping (MPM) protocol. One property of this parameter is its dependence on both shape and location of the brain, making it subject-dependent. As an additional assumption and seeing the small degree of variability across individuals, this value was assumed fixed during this project to $B_{1,eff} = 1.19$. The interpretation of this factor can be expressed as follows: when specifying a pulse with a flip angle of α° and a duration of τ milliseconds to the scanner console, it is equivalent to the application of a pulse with a flip angle of $(\alpha \cdot 1.19)^\circ$ during τ milliseconds in the LC region. The simulation results were therefore analysed according to this factor such that the following equation is satisfied:

$$B_{1,nominal} = \frac{B_{1,actual}}{B_{1,eff}} \tag{2.2}$$

where $B_{1,nominal}$ is the amplitude of the B_1 magnetic field specified at the scanner and $B_{1,actual}$ is the B_1 amplitude actually achieved in the LC region and modelled by the simulation parameters α_{RF} and τ_{RF} through EQUATION (1.7).

It appears clearly that the limitations previously set in terms of B_1 amplitude to 20 µT was applicable to the $B_{1,nominal}$ value since the maximum B_1 amplitude is hardware-dependant. The corresponding maximum B_1 amplitude value in the LC computed by the EPG-X simulations and accounting for the efficiency is then equal to $20 \cdot 1.19 = 23.8$ µT. This was implemented in the code `Optimal_Param.m` which returns the optimal parameter values while meeting the condition on B_1 maximum amplitude.

As a result, these constraints combined together dictate the optimal parameter values for α_{RF} and τ_{RF}.

2.1.1.3 Tissue-dependent parameters

Since the goal of this project is to quantify the contrast between the LC and its surroundings, it was crucial to differentiate these two tissue types in terms of parameters. Hence, values of tissue-dependent parameters had to be specified for both the LC and the surrounding areas. These parameters include the relaxation times $T_{1,a}$, $T_{1,b}$, $T_{2,a}$ and $T_{2,b}$ in respective compartments a and b, the bound pool fraction size f_b and the exchange rate k_{ab}. Parameters set for each tissue type are defined

with the subscript 'LC' or 'surr' to denote the locus cœruleus or its surroundings, respectively. Note that in the scope of this project the definition of the surrounding region is given by the voxels directly adjacent to the LC, corresponding to a thin layer of one voxel away from the structure, following previous studies [41].

First, in order to determine these values, available literature on the locus cœruleus was reviewed. While the scientific interest for this brain structure is growing since the past years, the specific quantitative information about the LC is still lacking. Additional unpublished data from quantitative imaging studies of the LC ongoing at WCHN were used to augment what could be found in the literature in order to specify estimates for all of the required model parameters. The specified parameter values used in simulations for characterising both the LC and the surroundings and their respective origin are reported in TABLE 2.1.

	LC		***Surroundings***	
	Compartment a	*Compartment b*	*Compartment a*	*Compartment b*
T_1 (ms)	1254.4 [(1)]	1245.4 [(1)]	1294.2 [(1)]	1294.2 [(1)]
T_2 (ms)	95.6 [(2)]	0.012 [(3)]	110 [(5)]	0.012 [(3)]
f	$1 - f_b = 0.9174$	0.0826 [(4)]	$1 - f_b = 0.7$	0.3 [(5)]
k_{ab} (Hz)	1.125 [(4)]		1.125[(5)]	

Table 2.1: Tissue-dependent parameter values specified in the SPGR simulations. (1): from MPM data; (2): from [46]; (3): from [31]; (4): from [42]; (5): assumed value.

In the LC, T_2, f_b and k_{ab} were suggested by literature on previous LC studies. T_1 values had to be estimated according to other strategies and were provided by the analysis of unpublished quantitative data from the WCHN.

In the surroundings, no literature data was available for characterising this particular tissue type. Therefore, parameters were estimated either based on the quantitative data available (T_1), either via additional assumptions (T_2, f_b and k_{ab}).

Furthermore, no differentiation appeared in literature about T_1 values in the distinct compartments.

The justifications for each parameter values are detailed in the following sections.

▸ Literature review

Based on literature values previously described and summarised in TABLE 1.2, the following parameters were used for characterising the LC in the EPG-X framework:

- $T_{2,\mathrm{LC}} = 95.6\,\mathrm{ms}$ [46];
- $f_{b,\mathrm{LC}} = 0.0826$ [42];
- $k_{ba,\mathrm{LC}} = 12.5\,\mathrm{Hz}$ [42].

A bound pool fraction of $f_{b,\text{surr}} = 0.3$ was estimated for the surroundings based on the reading of the colour bar of the PSR map (FIGURE 1.17) published in Trujillo et al. and the assumption that its value should be greater than the one for the LC given the observed contrast.

Additionally, the exchange rate $k_{ab,\text{LC}}$ from the compartment a to b in the LC structure was also derived from the reported literature value of $k_{ba} = 12.5\,\text{Hz}$. Indeed, by combination of EQUATIONS (1.2) and (1.5), the value of this parameter in the LC is defined by:

$$k_{ab} = k_{ba} \cdot \text{PSR}_{\text{LC}} = 12.5 \cdot 0.09 = 1.125\,\text{Hz} \tag{2.3}$$

No information regarding the surroundings was found in the literature. Furthermore, the T_1 relaxation times were also missing for both tissues.

▸ MPM data

Given the lack of literature details, a manual analysis of a quantitative multi-parametric mapping data set from four different subjects allowed to estimate T_1 values in both tissues. After defining the LC and surrounding region through specific masks, the relaxation times were extracted in both tissues and are $T_{1,\text{LC}} = 1254.4\,\text{ms}$ and $T_{1,\text{surr}} = 1294.2\,\text{ms}$. The differentiation between compartment in a given tissue was not allowed through this manual analysis.

Data acquired through the MPM protocol were provided by Dr. Dorothea Hämmerer, a collaborator on this project who has run previous studies at the WCHN aiming at visualising the LC. This multi-parameter mapping protocol provides high-resolution quantitative maps of the longitudinal relaxation rate $R_1 = \frac{1}{T_1}$, the effective transverse relaxation rate $R_2^* = \frac{1}{T_2^*}$, the effective proton density PD^* and magnetisation transfer saturation MT_{sat}. The strength of MPM protocol lies in the sensitivity of MR parameter measurements and their high comparability across sites and time points [49]. Data analyses were performed in MATLAB R2017B using the Statistical Parametric Mapping (SPM) software SPM12 and the `MPM_data.m` code [3].

The selected data set comprised multiple runs for four participants of different ages with a priori a good LC visibility. Participants were arbitrarily named from 1 to 4. For each subject, 3 runs were available and contained different quantitative maps (R_1, R_2^*, PD, MT_{sat}) and weighted images (with T_1-, PD- and MT-weighting) with a resolution of $0.6 \times 0.6 \times 3\,\text{mm}^3$. Manually drawn masks for the LC were also provided by two raters, i.e. neuroscientists familiar with the anatomy of the LC and surrounding structures capable of delineating the LC from MRI data using an established protocol based on anatomical landmarks. These masks were presented through two distinct forms : LC_CONJ, being voxels marked by both of two raters, and LC_UNION, corresponding to voxels marked by any of the two raters. Following this definition, the conjunction mask was more restrictive than the union one. The use of the appropriate mask depends on the application and desired output. FIGURE 2.1 shows examples of available data for participant 2. Reported images are a $40 \times 40 \times 40\,\text{mm}^3$ zoom in on the LC region of (a) the MT-weighted images, (b) the union and (c) conjunction LC masks. The locus cœruleus appears brighter than its surroundings on the MT-weighted image and is pointed out by red arrows. Masks are displayed without interpolation between voxels, explaining the irregular shape appearance of the LC mask given the anisotropic data. The anisotropic voxel shape aimed at fitting better the elongated shape of the LC and maximise the signal-to-noise ratio (SNR). The voxels distinction realised by the raters is easily observable when comparing the union and conjunction masks together.

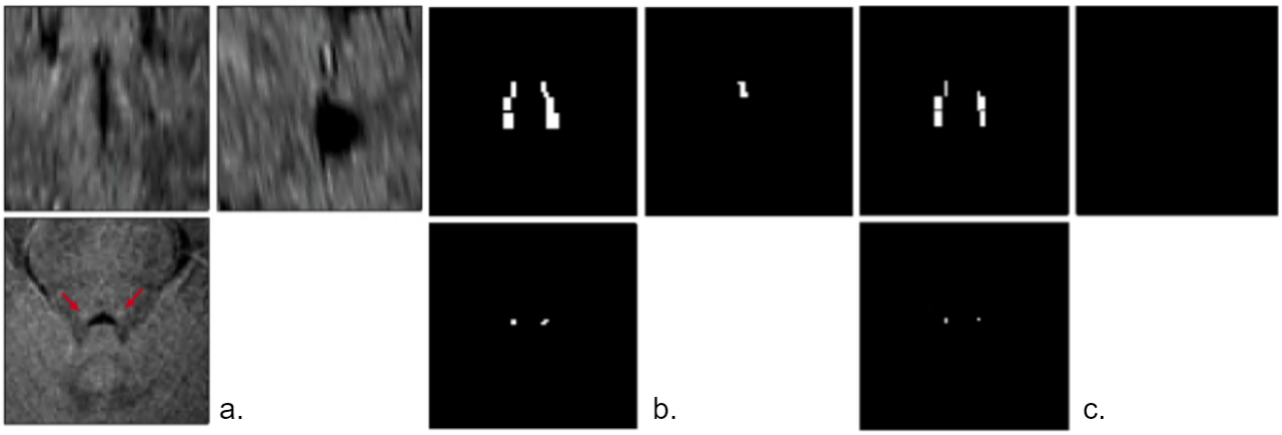

Figure 2.1: Data from the first run of participant 2. a. MT-weighted image, b. LC union mask, c. LC conjunction mask. Red arrows indicate the LC on the axial view. Zoom $40 \times 40 \times 40$ mm^3 on the LC region

The definition of the LC for extracting the quantitative parameter values was based on the conjunction mask since the latter gives us more confidence in the fact that the extracted voxels were effectively within the LC. As illustrated by FIGURE 2.1b and c, the union mask is more likely to include other tissues compared to the conjunction one. On the other hand, surroundings region was estimated by expanding the union mask by one voxel and then subtracting the dilated mask from the original one. In this way, the LC is totally excluded from this mask thereby defining the surrounding region as a thin layer of one voxel of size $0.6 \times 0.6 \times 3\,\text{mm}^3$ around the structure of interest. The definition of these masks came with the rejection of the potential influence of cerebrospinal fluid in parameters quantification. This was ensured by the segmentation of the fourth ventricle via the `Segment` module in the GUI Batch interface of SPM which categorises brain tissues in different classes such as grey matter, white matter and CSF. However, the precise definition of the CSF mask was quite challenging. The limited spatial coverage and the anisotropic resolution of the data led to numerous segmentation failures of the SPM `Segment` tools. Consequently, the segmentation procedure had to be specifically optimised for these data which involved the rejection of one of the four participants for which no valid results could be derived. In the `Segment` Batch interface, means of quantitative maps R_1, R_2^* and MT_{sat} across the 3 runs of each participant were specified in a multi-channel segmentation approach. The regularisation parameter of the bias field was set to '`very heavy regularization, 1`' to account for the fact that these inputs are quantitative maps in which the received field has already been removed through application of the signal models. The CSF mask outcome for participant 1 is exemplified in FIGURE 2.2b.

Through the superimposition of the inverse of the created CSF mask to the previously defined LC and surroundings ones, the CSF is totally excluded from the LC and surroundings masked voxels. FIGURE 2.2c shows the corresponding surrounding mask. The sagittal view of the surroundings mask highlights the removal of the fourth ventricle. The MT-weighted image in FIGURE 2.2a is provided for anatomical orientation of the masked structures.

The masking procedure consisted of superimposing, that is to say multiplying, the respective mask with the quantitative image of interest. This methodology was applied for each repeat of each of the three individuals. Given the specific definition of the LC and its surroundings masks in the MPM data, the quantitative parameter values R_1, R_2^*, PD and MT_{sat} were extracted in each voxel with confidence,

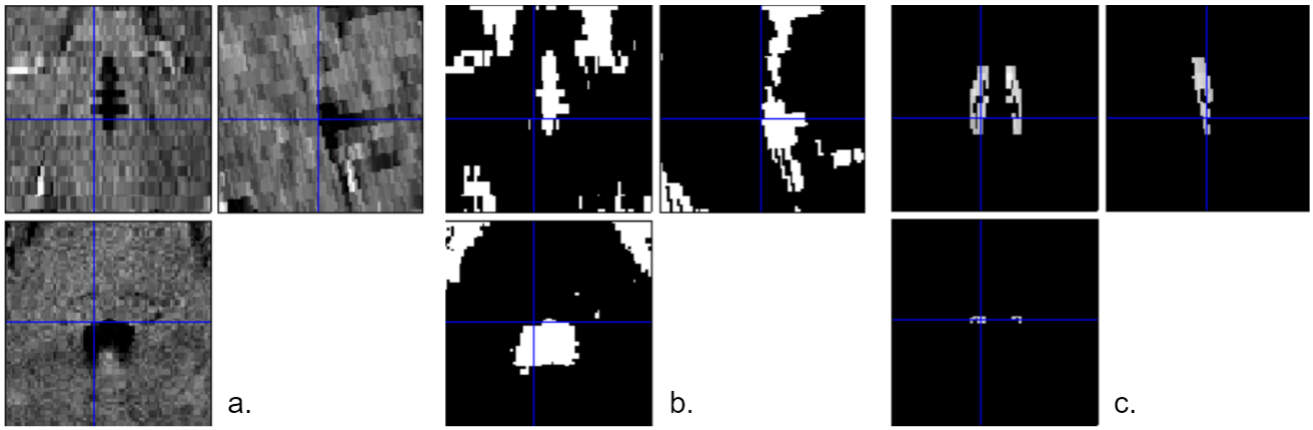

Figure 2.2: Data from participant 1. a. MT-weighted image, b. CSF mask created from segmentation of data in SPM, c. Surroundings mask without the CSF. (Zoom $40 \times 40 \times 40$ mm^3 on the LC region)

using the MATLAB code `MPM_data.m`. The respective parameter values were subsequently averaged across voxels. The means and standard deviations across voxels associated to each repeat of each participant are presented in TABLE 2.2. Finally, a global average was computed across all available data relative to a specific quantitative parameter.

As a first illustration of the computed data, FIGURE 2.3 shows clearly the impact of CSF on parameter values estimation and the necessity to remove it as much as possible from the studied data. In fact, it is known that the CSF has a very long T_1 value usually greater than 3 s [17]. Given that the MPM protocol is not optimised for tissue with long T_1 component, the precision of the quantification in the CSF was poor, affecting the precision in the surroundings when the CSF was not properly excluded. Regarding the estimation of the PD content, it is less straightforward to accurately set a value for both the LC structure and its surroundings seeing the high variability observed within runs and participants. Furthermore, PD evaluation requires received field removal which caused the segmentation to fail and normalisation, that is to say scaling, which is very difficult to do with this restricted field of view.

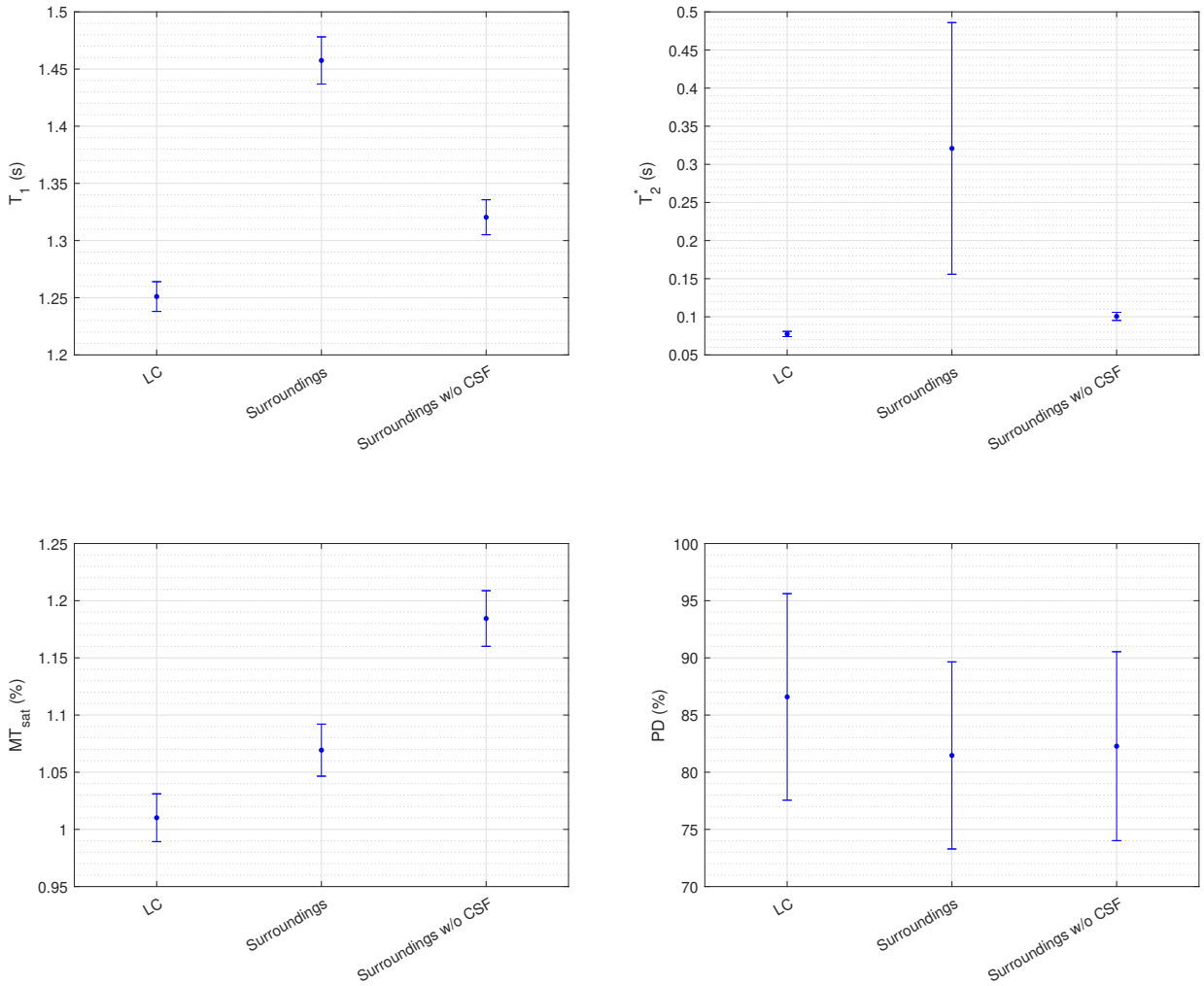

Figure 2.3: Mean and standard deviation of quantitative parameter values in the LC, its surroundings and its surroundings excluding the CSF computed from the mean value across voxels of each run of participants 1, 2 and 3

From data reported in TABLE 2.2, the first observation is that mean T_1 values computed across multiple runs in the LC were in line with the literature findings summarised in TABLE 1.2. Second, subject 1 presents infeasible proton density values, probably reflecting a failure of the algorithm to accurately estimate PD* for this participant since a value higher than 100 percent is unrealistic. The estimation of the quantitative PD parameter requires the segmentation of the white matter during the process. It is conceivable that this delineation process failed given the complexity of the segmentation of the CSF previously mentioned. Still, the high variability in the measured proton density within the two other subjects indicates that this result is not reliable. Where an accurate proton density is assumed, this quantitative value can be linked to the fractional size of the water pool of the two-compartment MT model. Indeed, this so-called free pool is composed of aqueous protons unrestricted in the tissue environment, as opposed to the bound pool. Since the computation of the quantitative PD map does not account for the bound protons, the PD content is equal to the fractional size of the free pool, f_a. Therefore, if the PD estimation in those data was reliable, we could have compared the tissue-dependent parameter f_b found in literature to the mean quantitative PD value coming from MPM data.

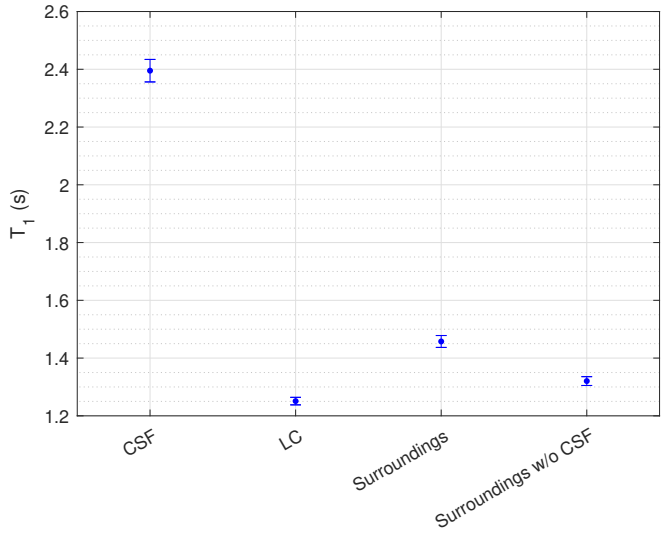

Figure 2.4: Mean and standard deviation of T_1 value in the CSF, the LC, its surroundings and its surroundings without the CSF computed from the mean value across voxels of each run of participants 1, 2 and 3

Finally, as third observation, a general conclusion about parameter values can be drawn. In fact, it is possible to distinguish between the surroundings and the LC in terms of parameter values, as expected according to previous studies aiming at visualising the LC. Thereby, while T_1, T_2^* and MT_{sat} are reported to be lower in the LC voxels compared to the surrounding ones, the PD content shows the opposite trend with higher proportion of aqueous protons in the nucleus.

▸ Additional assumptions

Up to this point, literature review and MPM data did not provide the entire information required to perform simulations. Indeed, no clear differentiation was made between the bound and the free pools of tissues studied in terms of parameter values while this had to be specified in the EPG-X code because of its two-compartment feature. Missing values were then determined based on additional assumptions as listed below.

First of all, a single value of the spin-lattice relaxation time T_1 was used for both the free and the bound pools such as $T_{1,a} = T_{1,b}$ in each tissue type, that it to say either the LC or the surroundings. The latter was estimated based on the MPM data analysis. This assumption is obviously not accurate but is made as a necessary simplification based on what is done in existing quantitative MT models, i.e. [42].

Second, the transverse component in the bound pool is reasonably assumed to be null within the EPG-X framework. However, the saturation of the longitudinal component is dictated by the absorption factor G which needs an estimation of $T_{2,b}$, here of 12 microseconds. Therefore, an underlying assumptions that is made is that the T_2 value in the free pool is equivalent to the T_2 value characterising the whole tissue.

Third, the exchange rate k_{ab} given by literature in the LC was hypothesised to be identical in its surroundings, mainly because of a lack of information about this feature in the literature reviewed and

LC				
Participant	$\mathbf{T_1}$ (s)	$\mathbf{T_2^*}$ (s)	$\mathbf{MT_{sat}}$ (%)	**PD** (%)
1	1.321 ± 0.102	0.069 ± 0.025	1.024 ± 0.166	157.96 ± 6.96
	1.315 ± 0.106	0.081 ± 0.035	0.968 ± 0.228	79.96 ± 3.31
	1.286 ± 0.115	0.086 ± 0.049	0.863 ± 0.180	141.48 ± 9.81
2	1.201 ± 0.136	0.102 ± 0.049	1.001 ± 0.143	60.47 ± 3.87
	1.253 ± 0.105	0.068 ± 0.019	0.961 ± 0.104	76.80 ± 4.70
	1.231 ± 0.099	0.075 ± 0.038	1.076 ± 0.190	61.95 ± 3.59
3	1.220 ± 0.070	0.066 ± 0.015	1.151 ± 0.225	91.04 ± 3.86
	1.192 ± 0.095	0.063 ± 0.020	1.031 ± 0.183	90.51 ± 6.01
	1.188 ± 0.111	0.077 ± 0.019	1.010 ± 0.179	66.04 ± 4.37
Mean $\pm$ std	**1.245 ± 0.051**	**0.076 ± 0.012**	**1.009 ± 0.079**	**91.80 ± 34.91**

Surroundings				
Participant	$\mathbf{T_1}$ (s)	$\mathbf{T_2^*}$ (s)	$\mathbf{MT_{sat}}$ (%)	**PD** (%)
1	1.343 ± 0.189	0.090 ± 0.066	1.184 ± 0.302	147.70 ± 10.00
	1.330 ± 0.195	0.104 ± 0.149	1.203 ± 0.290	75.02 ± 5.52
	1.302 ± 0.194	0.086 ± 0.052	1.161 ± 0.348	131.98 ± 9.61
2	1.261 ± 0.124	0.098 ± 0.078	1.221 ± 0.227	59.64 ± 4.03
	1.292 ± 0.119	0.089 ± 0.061	1.231 ± 0.241	73.84 ± 4.40
	1.290 ± 0.134	0.150 ± 0.243	1.322 ± 0.264	59.25 ± 4.06
3	1.292 ± 0.132	0.097 ± 0.063	1.337 ± 0.304	87.85 ± 6.45
	1.267 ± 0.137	0.082 ± 0.051	1.151 ± 0.222	86.23 ± 5.78
	1.270 ± 0.139	0.085 ± 0.073	1.132 ± 0.245	63.40 ± 4.45
Mean $\pm$ std	**1.294 ± 0.028**	**0.098 ± 0.021**	**1.216 ± 0.072**	**87.21 ± 31.82**

Table 2.2: Means and standard deviations across voxels of quantitative parameter values specified for each run of participant 1, 2 and 3 both in the LC and in its surroundings. The means and standard deviations over all runs of all participants are reported in the last table row for each parameter.

the poor knowledge about the macromolecular composition of the LC neighbourhood.

The relaxation time $T_{2,a}$ in the free pool of the surroundings was still unknown. Considering the previous assumption, the T_2 value characterising the entire surrounding tissue is studied. T_2 is a

difficult parameter to measure and not included in the MPM protocol. It has been set to 110 ms since a T_2^* of 98 ms was measured in the surroundings with MPM data and T_2 is by definition longer than T_2^*, according to EQUATION (1.1).

2.1.1.4 Metrics definition

Each tissue was therefore independently modelled through the EPG-X framework as a two-compartment system with exchange. This phenomenon influences independently the signal intensities of both tissues.

Signal intensity value computed in the LC and in its surroundings for the various range of parameters specified were respectively denoted by S_{LC} and S_{SURR}. The contrast between these two tissue signals was then computed. In alignment with analysis methods described in former studies aiming at quantifying the contrast in this structure [30, 41], a new variable C_n was introduced and defined as

$$C_n = \frac{S_{LC} - S_{SURR}}{S_{SURR}} \cdot 100 \tag{2.4}$$

with S_{LC} and S_{SURR} being the signal intensity in the LC and in the surroundings, respectively. In fact, when talking about signal intensity in a particular tissue, this corresponds to the mean of signal intensities across all the voxels included in the tissue mask.

This C_n variable represents the relative contrast, expressed in percent, between the locus cœrueleus and the surroundings. A risk is that if the signal amplitudes are small relative to the measurement noise then even a large percent improvement in contrast may be undetectable. The SNR therefore needs also to be considered. Noise quantification in MRI is a complex task which was not carried out during this project.

With the objective of optimising the observable contrast in the locus cœruleus and accounting for the SNR issue, a new variable C_w was introduced. The latter was created accounting for the trade-off required between the normalised contrast and the amount of signal in the LC. This weighted contrast is described as

$$C_w = S_{LC} \cdot C_n \tag{2.5}$$

Where this variable was maximum, the best trade-off could be expected between the amount of LC signal and the relative contrast C_n between the LC and its surrounding areas.

Note that while the optimisation of the SPGR sequence was based on the maximisation of the so-called weighted contrast C_w, this variable is not interpretable in terms of absolute values. A more representative metrics is the normalised contrast C_n, actually quantifying the relative difference between LC and surroundings signal intensities.

2.1.2 Data acquisition

From simulation results, optimal parameter values could be derived to theoretically best visualise the locus cœruleus with spoiled gradient echo sequences. In order to verify these outcomes and to assess for the good model representation of the *in vivo* mechanisms, an MRI acquisition protocol was defined with the aim of acquiring experimental data. Given the unexpected situation of Covid-19 and the unfortunate closure of the UCL buildings during this crisis, only one data set was acquired based on the simulation of the SPGR sequence. These data were acquired on one participant on a

3 T Siemens Magnetom Prisma scanner at the WCHN, London. The protocol of this experiment was based on the optimal parameter values reported by the simulation outcomes analysis of the SPGR sequence, that is to say $\alpha_{RF} = 10.5^\circ$, $\tau_{RF} = 30\,\mu s$ and $\phi_0 = 90^\circ$. The positioning of the field of view (FOV) was realised such that the selected slab is orthogonal to the locus cœruleus. Because some of the acquisitions are anisotropic, the low resolution direction needs to aligned with the long axis of the LC in order to maximise the SNR in each voxel.

In this section, the specifications required for the accurate fulfilment of the data acquisition are first reported. Then, the protocol and methods applied for the realisation of the experiments are presented.

2.1.2.1 Specifications

Simulations performed are characterised by the tissue properties of the LC and the surroundings. Because ideal conditions are considered with homogeneous B_1 amplitude across tissues, the parameter value entered at the console differs from the one given by simulations. The $B_{1,eff}$ factor in the LC region had to be accounted for when determining the flip angle value specified at the scanner following EQUATION (2.2). The latter translates into a flip angle $\alpha_{nominal}$ specified at the scanner such as:

$$\alpha_{nominal} = \frac{\alpha_{actual}}{B_{1,eff}} \tag{2.6}$$

where α_{actual} is the flip angle actually achieved in the LC region. The simulation results refer to as the actual values α_{actual} and in a further extend $B_{1,actual}$.

Furthermore, the optimal pulse duration τ_{RF} was converted into a pulse duration according to the pulse shape. From the developments summarised in TABLE 1.1, the total pulse duration was specified to the scanner based on the time characteristic given by the simulations such as:

- $T_{rect} = \tau_{RF}$ for a rect pulse,
- $T_{sinc} = BWT \cdot \tau_{RF}$ for a sinc pulse.

2.1.2.2 Protocol

Protocol parameters are presented in TABLE 2.3. Henceforth, BWT is the bandwidth-time-product of the sinc pulse, $\alpha_{nominal}$ is the actual flip angle specified in the console taking into account the B_1 efficiency and computed according to EQUATION (2.6), and T_{sinc} is the total duration of the sinc pulse as established by EQUATION (1.13). After defining the RF spoiling increment ϕ_0 and the image resolution, the expected normalised contrast C_n and the weighted contrast C_w from the performed simulations are also reported. Note that the analysis of the data acquired will be referred to as their respective sequence label in th following sections.

In this experiment, data were acquired using the standard PD- and T_1-weighted protocol settings used in ongoing studies of the LC at WCHN. Given their known expected contrast in practice, they provide a good data set to refer to when deciding if the simulation results can be used to improve over existing protocols. The protocol predicted by simulations to provide optimal contrast was also acquired. To investigate the effect of the BWT on the sinc pulse which is required to achieve slab-selection, data were acquired with values of 6 and 10. To examine the effect of RF spoiling increment, two values were used: $\phi_0 = 90^\circ$ predicted by simulations to be optimal, and $\phi_0 = 137^\circ$ the standardly

used phase increment. The effect of resolution and pulse selection were also investigated by acquiring data with 0.8 mm isotropic resolution and by subsequently expanding the coverage to the whole brain enabling non-selective excitation and therefore comparison with a rect pulse.

The main drawback of the non-selective brain acquisitions is the long scan time required. However, these allow general brain characterisation without focusing solely on the LC. The latter could be efficiently incorporated into a whole brain MPM protocol or used in combination with functional magnetic resonance imaging (fMRI) data for structures alignment.

Anisotropic voxels are considered in standard LC visualisation protocols in order to average the signal along its cylindrical shape and thereby maximise the SNR. Indeed, due to the small axial size of this nucleus, a high in-plane resolution is required which leads to long scan time as well as low SNR. Another limitation of the anisotropic protocol is given by the requirement on the excited slab to be perpendicularly aligned with the LC so that it can be visible. Considering the small and elongated shape of the LC, these acquisitions are extremely vulnerable to the field of view (FOV) position and to participant motion if the LC is repeatedly imaged, as it is generally the case to improve SNR or facilitate quantitative MRI investigation of its microstructure. These drawbacks concerning the anisotropic resolution motivated the study of the impact of the voxel shape on LC visualisation through isotropic acquisitions. In general, going from anisotropic to isotropic voxel size increases the image resolution but reduces the SNR and requires a higher acquisition time. However the benefit of isotropic voxels for LC visualisation is that the field of view does not have to be aligned with its cylindrical structure, contrary to the anisotropic case.

#	Sequence label	BWT	α_{nominal} (°)	T_{sinc} (µs)	ϕ_0 (°)	Voxel size (mm^3)	C_n (%)	C_w
1	Localiser							
2	PD_BWT6	6	6	160	137	$0.6 \times 0.6 \times 3$	44.33	3.46
3	T_1_BWT6	6	21	560	137	$0.6 \times 0.6 \times 3$	35.25	2.36
4	PD_BWT10	10	6	160	137	$0.6 \times 0.6 \times 3$	51.25	3.84
5	T_1_BWT10	10	21	560	137	$0.6 \times 0.6 \times 3$	38.75	2.51
6	Opt_FA7	10	7	300	90	$0.6 \times 0.6 \times 3$	45.68	3.71
7	Opt_Inc137	10	7	300	137	$0.6 \times 0.6 \times 3$	44.61	3.68
8	Opt_Iso_FA7	10	7	300	90	$0.8 \times 0.8 \times 0.8$	45.68	3.71
9	B_1 map							
10	Opt_FA11	10	11	300	90	$0.6 \times 0.6 \times 3$	47.95	4.01
11	Opt_Iso_SincNS	10	7	300	90	$0.8 \times 0.8 \times 0.8$	45.68	3.71
12	Opt_Iso_RectNS	10	7	300	90	$0.8 \times 0.8 \times 0.8$	45.68	3.71

Table 2.3: Experimental protocol and associated sequence characteristics

For each sequence, a repetition time TR = 24.5 ms was used and the oversampling was set to 0% to aid visualisation of the slab profile with 24 phase-encoded points per slab.

Note the localiser and B_1 map acquisition sequences allowing the definition and the alignment of

the scan plane, and the mapping of the B_1 amplitude, respectively.

Simulations predicted that the optimal flip angle would be that with maximum B_1 amplitude (see results TABLE 3.1). While, the optimal flip angle predicted by the simulations was 9 degrees, this was erroneously specified as 7 degrees in the protocol. However, experimentally the B_1 constraint set to 20 µT could also be relaxed allowing a flip angle of 11 degrees to be obtained. Inadvertently this led to good sampling of the B_1 range

α_{nominal}	C_n	C_w
7°	45.68 %	3.71
9°	47.62 %	4.01

Table 2.4: Comparison of the expected simulated contrasts C_n and C_w resulting from optimal sequence with $\alpha_{\text{nominal}} = 7^\circ$ and 9°

2.1.3 Image processing

The co-registration of the acquired data, the segmentation of the locus cœruleus and the resulting masks determine the accuracy of the contrast quantification. Therefore, an imprecise manipulation of the data can lead to biased contrast values.

Given the small size of the LC and the variable resolution used across protocols, the aim was to define the LC in a common, high resolution space. This was done using a Super-Resolution (SR) technique developed at the Centre [47] and was integrated into the co-registration step. Representing data on an alternative spatial grid requires the data to be resampled (referred to as `Reslice` in the SPM software used) after co-registration (`Estimate` in the SPM software). The super-resolution algorithm had an additional capacity to de-noise. Given the low SNR of these data, this option was additionally explored. The LC segmentation was then performed on the outcomes of the Super-resolution algorithm, creating the corresponding masks which were finally resampled to the appropriate space.

All data were processed in SPM12 thanks to the existing toolboxes of the Batch interface.

2.1.3.1 Co-registration – Estimate

The co-registration of the images was performed in order to spatially realign the data by transposing it into one identical coordinate space called the world space. This was done by using the `Coregister - Estimate` module in the SPM Batch. The image considered as reference was the first echo generated with the Opt_Iso_FA7 sequence characterising the optimal isotropic acquisition (see TABLE 2.3). While this manipulation ensured the alignment of data in the same space, the image and the contained information were not affected by this process, contrary to the effect of the `Coregister - Reslice` module which resamples the data based on the transformation matrix defined by the coregistration.

2.1.3.2 Super-resolution algorithm

The Super-resolution algorithm is a new tool developed at the WCHN [47] and implemented in the SPM12 software on `Matlab` which provides an efficient solution for denoising and super-resolving multi-contrasts MR images. As the name states, this approach allows to grab the input data into a finer grid, therefore improving the resolution while removing the noise from processed images. By providing a better data quality, the segmentation of the LC is expected to be more accurate which in turns improves the contrast quantification in this structure.

Therefore, after being co-registered, realigned data were super-resolved using the `Denoising/Super-Resolution` toolbox in the GUI Batch of SPM software. This algorithm was applied concurrently to the first echo of all acquisitions, which were assumed in this context to have the same contrast weighting, i.e. contrast of 1 in the toolbox. The voxel size to which the data would be super-resolved was specified to $0.6 \times 0.6 \times 0.6\,\mathrm{mm}^3$ and the slice gap was set to 0. Regularisation and number of iterations were set to 5 and 10, respectively. Because the co-registration was already performed independently to the SR algorithm, the `Coregister` option was disabled. All other parameters were kept to their default value.

The SR algorithm was also applied to individual data acquired through one specific sequence in order to observe the impact of the algorithm on the image quality. From these observations (see Results FIGURE 3.12), the SR approach was integrated into the data processing procedure of this project.

2.1.3.3 LC segmentation

Segmentation of the LC based on the SR output was performed by Dr. Dorothea Hämmerer and by Dr. Matthew Betts, a second collaborator on this project and a neuroscientist at the DZNE in Magdeburg.

Each rater manually segmented the LC independently according to the following guidelines: either include all voxels potentially within the LC or conservatively identify only those voxels highly likely to be within the LC. In addition, the segmentation of the fourth ventricle was performed for masking the CSF and rejecting the potential influence of this tissue in the contrast quantification.

FIGURE 2.5 shows the definition of the LC structure according to the two guidelines. (a) shows the conservative mask, depicting LC voxel with strong confidence while (b) appears as more general mask which provides an excellent idea of the overall anatomical position of this structure. (c) depicts the delineation of the CSF in the fourth ventricle and (d) illustrates the super-resolved data provided for the LC segmentation.

The conservative mask was subsequently used to describe the LC whereas the general one was preferred to define the surroundings in order to minimise the risk of partial volume effects biasing the contrast measures. Practically, the mask was obtained by the dilation of the LC mask by one voxel of the same size to which the original mask was subtracted.

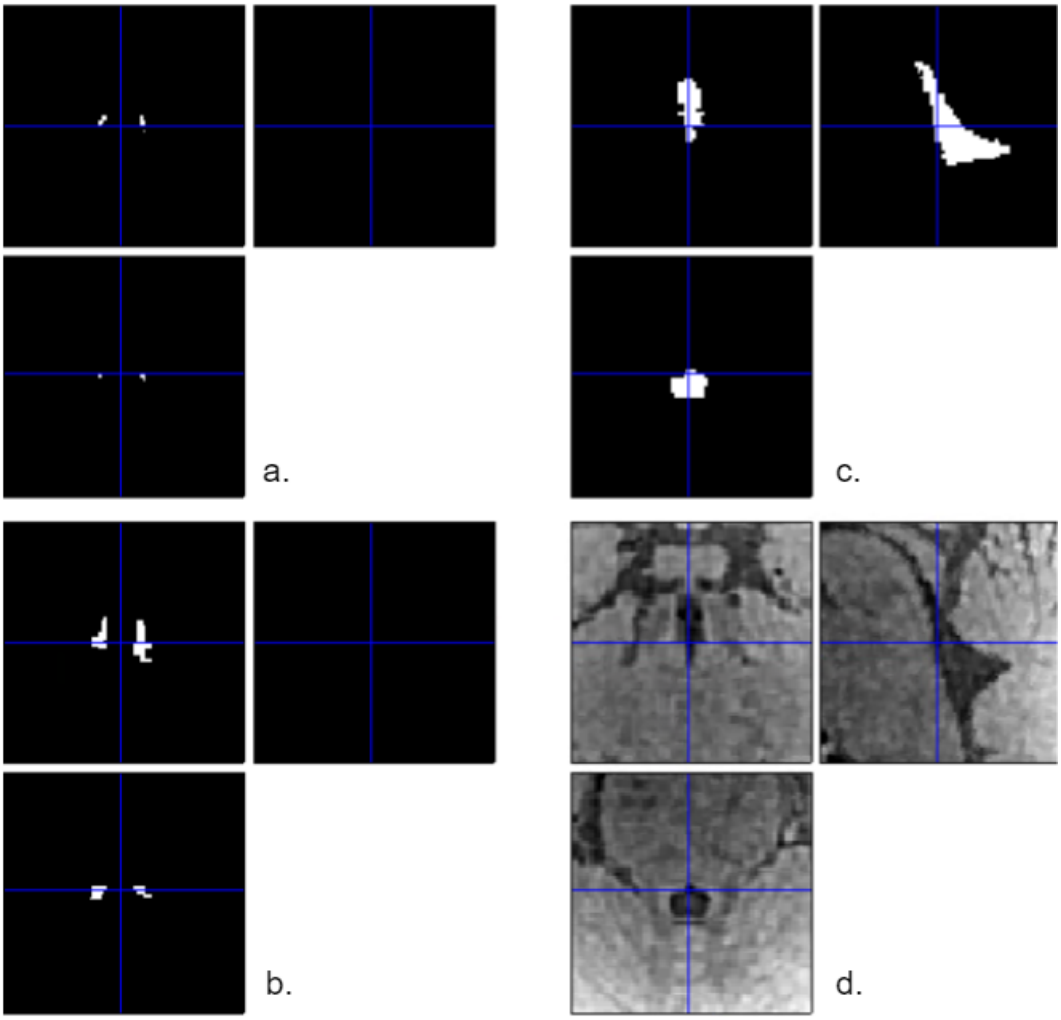

Figure 2.5: a. Conservative LC mask, b. General LC mask, c. CSF mask, d. Output of the SR algorithm used for the segmentation process. Zoom $40 \times 40 \times 40$ mm^3 in the LC region.

2.1.3.4 Co-registration – Reslice

Through the process of Super-resolution, the created masks based on the segmentation of the LC were computed in a space differing from the original space of the acquired data. Therefore, the co-registration of these masks to the grid of each respective original image was realised. The mask was hence modified through the reslice module to match the grid of the non super-resolved data. This was achieved through the `Coregister - Reslice` module in the GUI of SPM for each individual image. Note that the order of interpolation was set to the highest possible, corresponding to the 7th order B-spline interpolation, with the purpose to optimise the fit of the data and the inherent precision. This only comes at computational time costs because of the higher number of neighbour points considered and is suggested when the data was subjected to participant motion. This data processing results in 10 different masks one for each sequence played out in the scanner.

2.1.4 Contrast quantification

The quantification of the contrast arising from the *in vivo* experiment was realised in MATLAB with the `LC_data.m` code following a similar methodology to the one applied for the extraction of parameter values in the MPM data set in SECTION 2.1.1.3.

For each of the 10 sequences played out, the signal in the LC and its surroundings were extracted from each voxel included in the corresponding mask. Then, the mean and the related standard deviation of the signal intensities across the LC and surroundings voxels were computed for each sequence. Through the EQUATIONS (2.4) and (2.5), the normalised and weighted contrast were finally determined. The estimation of the uncertainty on the evaluation of the contrast in the experimental data set was calculated based on the theoretical formula of the error propagation [27] such as:

$$\sigma^2_{C_{\text{exp}}} = C^2_{\text{exp}} \cdot \left(\frac{\sigma^2_{\text{LC}} + \sigma^2_{\text{surr}}}{(S_{\text{LC}} - S_{\text{surr}})^2} + \frac{\sigma^2_{\text{surr}}}{S^2_{\text{surr}}} \right) \tag{2.7}$$

where σ is the standard deviation on computed means across voxels, C_{exp} is the mean contrast measured experimentally across voxels and 'LC' and 'surr' subscripts characterise the signal in the LC and the surroundings, respectively.

The correlation between the contrast predicted by the simulations and that measured experimentally was subsequently estimated.

2.2 Optimisation of SPGR sequence with MT pre-pulse: simulation

Applying an MT pre-pulse allows the selective saturation of the bound pool and amplification of MT-based contrast. This was explored in simulation by extending the EPG-X(MT) framework previously used to additionally model the application of such an off-resonance prepulse in the SPGR sequence.

2.2.1 Simulations

Along the same lines as for the optimisation of the SPGR sequence, simulations were realised in MATLAB with the code `Simu_SPGR_MT.m` based on the EPG-X(MT) framework [31]. However, because of the addition of a saturation pulse to the model, the implementation of a new code had to be realised for simulating the SPGR sequence with MT pre-pulse. The description of the algorithm implemented is first provided, then parameters involved in this model are specified. The distinction between sequence-dependent and tissue-dependent parameters is also made.

2.2.1.1 EPG-X framework

The EPG-X(MT) modelling framework with a single pre-pulse at the outset of the acquisition was modified to model an MT-weighted acquisition with a pre-pulse and excitation pulse each repetition time TR. While the excitation acted on both pools as before, the pre-pulse acted only on the bound pool, with the degree of saturation dictated by the Super-Lorentzian absorption lineshape $G(f_z)$ [22] now evaluated at the off-resonance frequency used for the pulse in the code `SL.m`. Finally, dedicated time periods, labelled TR_1 and TR_2 such that $TR = TR_1 + TR_2$ were incorporated to allow for differential periods of exchange and relaxation between the pre-pulse and excitation (TR_1) and between the excitation and the subsequent pre-pulse (TR_2). The implementation of these changes are found in the new code version called `EPGX_GRE_prepMT.m`. The simulations are implemented in the code `Simu_MT.m`.

In practice, it is usual that MT preparation pulses are shaped like Gaussian pulses when played out in scanners and so were used in these simulations through the expressions (1.17) and (1.18). A sinc pulse characterised by the expression (1.13) was used to model the excitation. Sequence-dependent and tissue-dependent parameter values chosen for this SPGR with MT pre-pulse model are described in the following sections.

2.2.1.2 Sequence-dependent parameters

Like for the SPGR sequence optimisation case, the repetition time TR was set to 24.5 ms. In addition to the parameters characterising the RF excitation pulse ($B_{1,RF}$, τ_{RF}, ϕ_0), the off-resonance MT saturation pulse had to be defined through the specification of four new parameters: the amplitude of the MT pulse $B_{1,MTC}$, the characteristic time of this pulse τ_{MTC}, its off-resonance frequency f_{MTC} and the time delay TR_1 between the saturation and the excitation pulses. As a result, seven degrees of freedom were investigated in order to optimise the visualisation of the LC.

The following parameter ranges were investigated:

- $B_{1,RF} \in [2\ 26]$ μT, with intervals of 4 μT;

- $\tau_{RF} \in [10\ 100]$ µs, with intervals of 10 µs;
- $\phi_0 = 90^\circ, 137^\circ$;
- $B_{1,MTC} \in [2\ 26]$ µT, with intervals of 4 µT;
- $\tau_{MTC} \in [100\ 1000]$ µs, with intervals of 100 µs;
- $f_{MTC} \in [2000\ 10000]$ Hz, with intervals of 2000 Hz;
- $TR_1 \in [TR_{1,min}\ TR_{1,max}]$ ms, with intervals of 1 ms.

The determination of ranges of values was based either on the previous simulations or on the MT-weighted protocol currently used at WCHN for LC visualisation. Note the coarser sampling of the parameters used for computational efficiency. The maximum B_1 amplitude for both pulses was limited to 26 µT to account for hardware limitations. This value was increased compared as before since experiments revealed a higher achievable B_1 amplitude.

The MT-weighted acquisition currently being used to visualise the LC at WCHN has the following parameters:

- TR = 24.5 ms;
- $\alpha_{RF} = 12^\circ$;
- $T_{RF} = 320$ µs;
- BWT= 6;
- $\phi_0 = 137^\circ$;
- $\alpha_{MTC} = 220^\circ$;
- $T_{MTC} = 4000$ µs;
- $f_{MTC} = 2000$ Hz.

Because of the relations (1.13) and (1.17), the characteristic times of the RF and MT pulses for the MT-weighted protocol are respectively given by $\tau_{RF} = \frac{320}{6} = 53$ µs and $\tau_{MTC} = \frac{4000}{7.434} = 538$ µs. Through the EQUATIONS (1.14) and (1.18), the corresponding B_1 amplitude of the excitation and preparation pulses are given by $B_{1,RF} = \frac{12}{\gamma \cdot 53} = 14.77$ µT and $B_{1,MTC} = \frac{220}{\sqrt{2\pi}\gamma \cdot 538} = 26.68$ µT, respectively. From these values, sensible parameter ranges were set. Moreover, the analysis of the RF spoiling increment was realised on two values corresponding to the optimal one from previous simulations (see Results 3.1.1) and the one currently used in the MT-weighted protocol.

Through the review of several studies performed with MT preparation pulses, the achievable limits for the duration and the off-resonance frequency of the saturation pulse were established and set to $\tau_{MTC} \in [100\ 1000]$ µs with steps of 100 µs and $f_{MTC} \in [2\ 10]$ kHz with steps of 2 kHz [23, 30]. Finally, the time delay between the MT saturation and RF excitation pulses was mainly determined by the timing specifications of the SPGR sequence implemented at the WCHN. This sequence is represented in a schematic way by FIGURE 2.6.

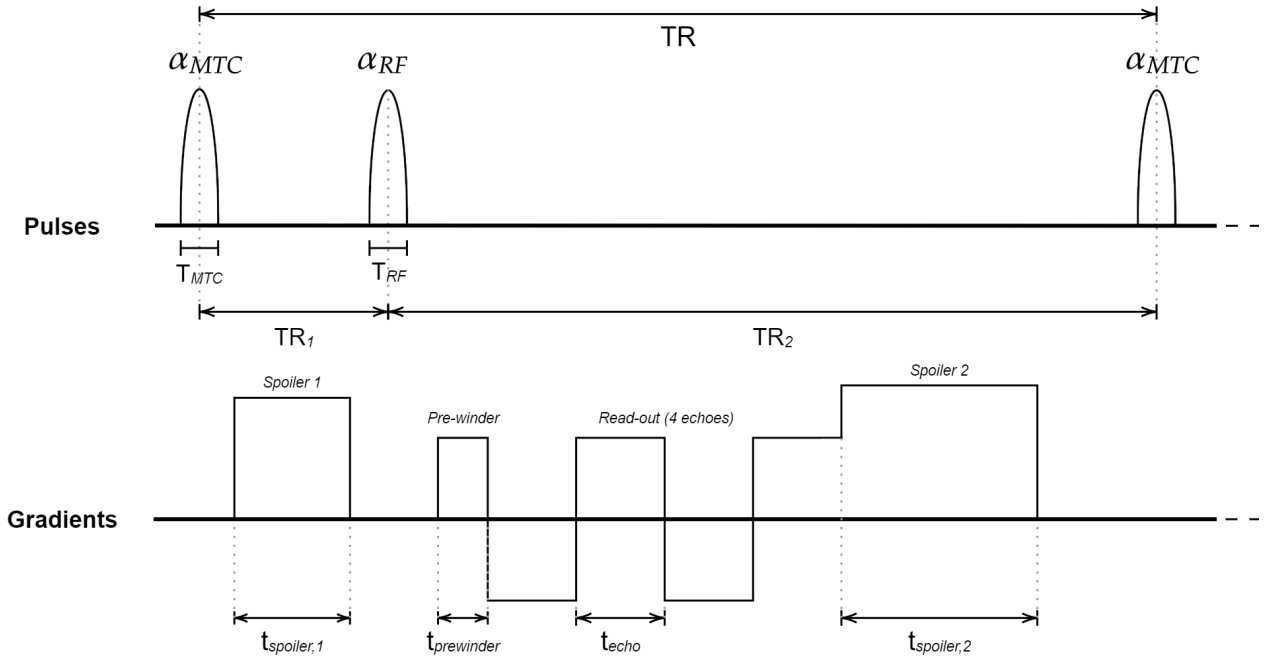

Figure 2.6: Schematic representation of the SPGR sequence with MT pre-pulse and corresponding timing parameter notations

Similarly to what is done in Helms et al. paper [26], TR_1 is defined as the time delay between the saturation and the excitation pulse. During this time period, exchange processes related to the MT effects will occur. This time period is subjected to a minimum value dictated by the minimum duration of the pulses and gradients composing it. The SPGR sequence with MT pre-pulse is implemented at the WCHN in such a way that the following constraints exist on the minimal TR_1 parameter value:

$$\mathrm{TR}_{1,\min} = \frac{\mathrm{T_{MTC}}}{2} + \frac{\mathrm{T_{RF}}}{2} + t_{\mathrm{spoiler},1} + t_{\mathrm{prep}} \tag{2.8}$$

where T_{MTC} is the duration of the MT saturation pulse, T_{RF} is the duration of the RF excitation pulse, $t_{\mathrm{spoil},1}$ represents the length of the spoiler 1 between these two pulses which is equal to 1.2 ms and t_{prep} is time required to prepare the coil and gradients, not represented in FIGURE 2.6. The latter is imposed by the slew rate limitations and the coil control lead time of the scanner and is at least equal to 100 µs for the 3T Prisma scanner from the WCHN.

Because the repetition time TR is fixed, the time period TR_2 corresponding to the time delay between the excitation pulse and the next MT pulse is trivially expressed by

$$\mathrm{TR}_2 = \mathrm{TR} - \mathrm{TR}_1 \tag{2.9}$$

Similarly, TR_2 is subjected to a minimal value given by

$$\mathrm{TR}_{2,\min} = \frac{\mathrm{T_{MTC}}}{2} + \frac{\mathrm{T_{RF}}}{2} + t_{\mathrm{spoiler},2} + t_{\mathrm{prewinder}} + t_{\mathrm{readout}} + t_{\mathrm{prep}} \tag{2.10}$$

where $t_{\mathrm{spoil},2}$ is the duration of the spoiler 2 at the end of the sequence, $t_{\mathrm{prewinder}}$ is the time required for the prewinder to be played out and t_{readout} is the readout time required by the gradients to acquire the echoes. The duration of the spoiler 2 and the prewinder taken together is set to 5.71 ms based

on existing sequences. Moreover, t_{readout} is defined by the number of echoes n_{echo} composing the sequence such that

$$t_{\text{readout}} = n_{\text{echo}} \cdot t_{\text{echo}} \tag{2.11}$$

with $t_{\text{echo}} = 2.8\,\text{ms}$, the readout duration for a single echo.

Because of the relation (2.9) existing between TR_1 and TR_2, the maximum admissible value for TR_1 is linked to the minimum value $TR_{2,\text{min}}$ imposed by the sequence characteristics in (2.10) such that

$$TR_{1,\text{max}} = TR - TR_{2,\text{min}} \tag{2.12}$$

Boundaries for TR_1 values achievable are therefore defined in an interval $[TR_{1,\text{min}}\ TR_{1,\text{max}}]$ according to EQUATIONS (2.8) and (2.12) for each pair of (τ_{RF}, τ_{MTC}) values. Through the implementation of the former timings within the EPG-X framework, the range of achievable values for the time delay between the saturation and the excitation pulse was then defined for every duration of RF and MT pulses. The incremental step considered when varying the balance between TR_1 and TR_2 was set to 1 ms. This step value allowed a precise division of the TR_1 interval while minimising the simulation time costs.

2.2.1.3 Tissue-dependent parameters

Because the tissues modelled within this EPG-X framework are identical to previously, the tissue-dependent parameters determined in the LC and the surroundings from the first simulations were used. However, a notable modification was the value of the fractional size of the compartment *b* in the surroundings which was changed to $f_b = 0.13$ based on the validation of the SPGR model. TABLE 2.5 outlines the specific values used during this part of the project.

	LC		***Surroundings***	
	Compartment a	*Compartment b*	*Compartment a*	*Compartment b*
T_1 (ms)	1254.4 (1)	1245.4 (1)	1294.2 (1)	1294.2 (1)
T_2 (ms)	95.6 (2)	0.012 (3)	110 (5)	0.012 (3)
f	$1 - f_b = 0.9174$	0.0826 (4)	$1 - f_b = 0.87$	0.13 (5)
k_f (Hz)	1.125 (4)		1.125 (5)	

Table 2.5: Tissue-dependent parameter values specified in the SPGR simulations with MT pre-pulse. (1): from MPM data; (2): from [46]; (3): from [31]; (4): from [42]; (5): from the validation of the SPGR model

Chapter 3

Results

3.1 Optimisation of SPGR sequence: simulation and validation

In this section, the results of the EPG-X simulations, the data acquisition and the validation through contrast quantification are presented for the SPGR model with the aim of obtaining the best visualisation of the LC.

3.1.1 Simulation results

Through EPG-X simulations, it was feasible to evaluate and quantify signal intensities expected in the locus cœruleus and in its neighbourhood while accounting for exchange between compartments within a given tissue type, i.e. voxel. The results presented hereunder were obtained through the MATLAB code `Simu_SPGR.m`.

The optimisation of the LC visualisation was achieved based on the maximisation of the weighted contrast C_w, as developed in the Methods chapter. This SPGR model with three degrees of freedom (α_{RF}, τ_{RF} and ϕ_0) was therefore optimised accordingly. The set of parameters providing the highest C_w value for a maximum B_1 amplitude of 20 µT taking into account a B_1 efficiency of 1.19 was given by:

- $\alpha_{RF} = 10.5^\circ$
- $\tau_{RF} = 30\,\mu s$
- $\phi_0 = 90^\circ$

The impact of parameter values on the signal intensities in the LC and in the region around it were investigated by fixing two out of three degrees of freedom to their optimal value previously reported while varying the third one in its respective range of values.

FIGURE 3.1 depicts the respective signal intensity expected in the LC and its surroundings for ϕ_0 ranging from 1 to 180°, with $\alpha_{RF} = 10.5^\circ$ and $\tau_{RF} = 30\,\mu s$ fixed. The first observation is the lower signal intensity values in the surroundings than in the LC. This result is in line with the brighter appearance of the LC in MT-weighted images compared to its surroundings. Second, the variation of the RF spoiling increment does not have a huge impact on the respective signal values.

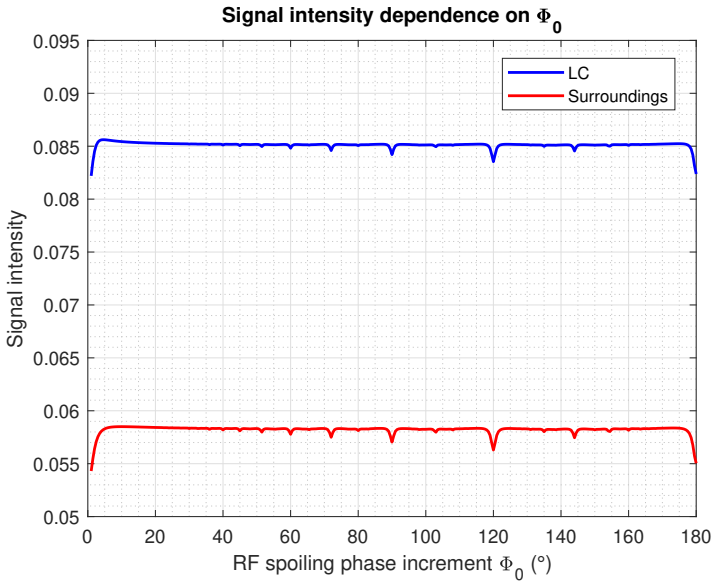

Figure 3.1: Signal intensities in the LC and in its surroundings as a function of ϕ_0, for $\alpha_{\mathrm{RF}} = 10.5^\circ$ and $\tau_{\mathrm{RF}} = 30\ \mu$s

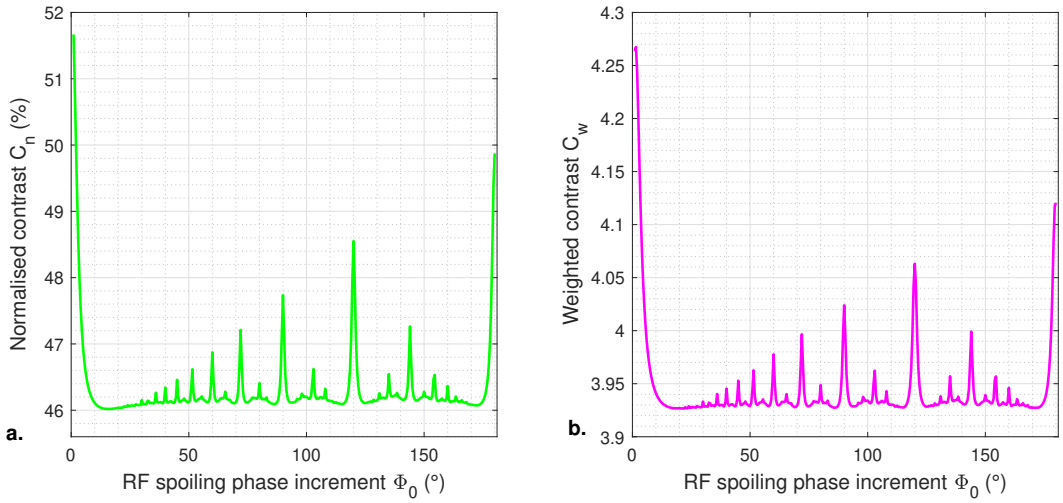

Figure 3.2: a. Normalised contrast C_n and b. weighted contrast C_w between the LC and the surroundings as a function of ϕ_0, for $\alpha_{\mathrm{RF}} = 10.5^\circ$ and $\tau_{\mathrm{RF}} = 30\ \mu$s

After the computation of the normalised and weighted contrasts C_n and C_w, FIGURE 3.2 is obtained. The normalised contrast is depicted in FIGURE 3.2a as a function of the RF spoiling increment. Similarly, FIGURE 3.2b illustrates the weighted contrast as a function of ϕ_0. Since the goal of these simulations was to find the set of parameters giving rise to the optimal contrast in the LC region, the optimisation of the SPGR sequence in terms of RF spoiling increment was realised through the maximisation of the weighted contrast C_w. The analysis of this variable reported maxima in C_w for $\phi_0 = \{0, 180, 120, 90, 144\}^\circ$, listed in a decreasing order of weighted contrast magnitude. However, these optimal values are ones that are in highly unstable regions given the high change of signal with respect to ϕ_0. As a compromise, value such that $\phi_0 \in [0\ 20]^\circ$,$\phi_0 = 120^\circ$ and $\phi_0 \in [160\ 180]^\circ$ corresponding to large peak values were excluded. The rejection of the solution $\phi_0 = 120^\circ$ was supported by results established by Preibisch and Deichmann (2009) [34] stating that particular RF spoiling

increments, including $\phi_0 = 120^\circ$, led to instabilities and very large errors in T_1 quantification. The RF spoiling increment $\phi_0 = 90^\circ$ for α_{RF} and τ_{RF} fixed was then considered as a good compromise for balancing stability and effect size.

Additionally, FIGURES 3.3 and 3.4 show that the RF spoiling increment has a much smaller impact on signals than both the flip angle α_{RF} and the characteristic time τ_{RF} do. These plots depict the dependence of the variable C_w on α_{RF} and ϕ_0, for τ_{RF} fixed to 0.02 ms and 0.1 ms respectively. These τ_{RF} values were chosen as extrema within the parameter range to illustrate that the optimisation of ϕ_0 is not determined by the flip angle and the RF pulse duration time since maxima were identifiable for $\phi_0 = \{0, 180, 120, 90, 144\}^\circ$ in both graphs as previously. Note that the weighted contrast is amplified for α_{RF} values between 5 to 20°.

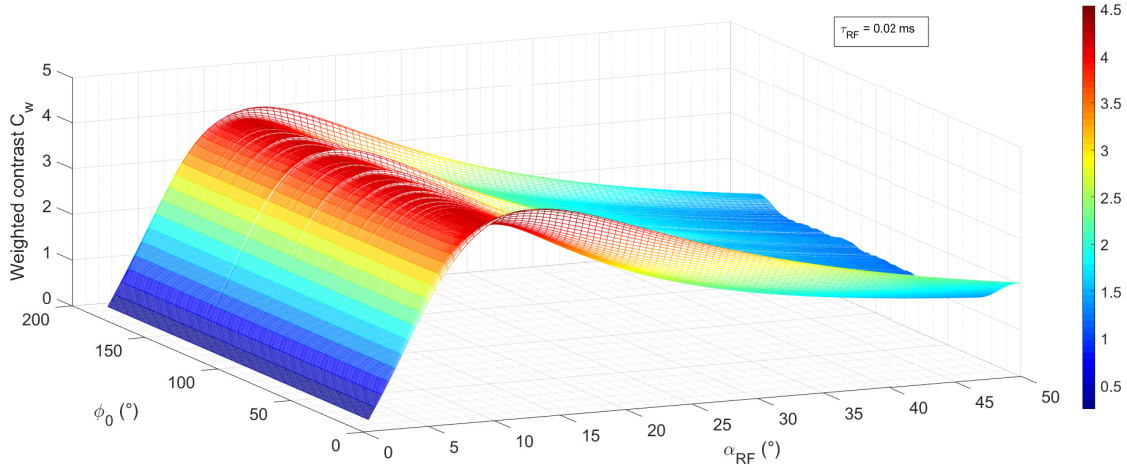

Figure 3.3: Weighted contrast simulated between the LC and its surroundings for a pulse duration of $\tau_{RF} = 0.02$ ms

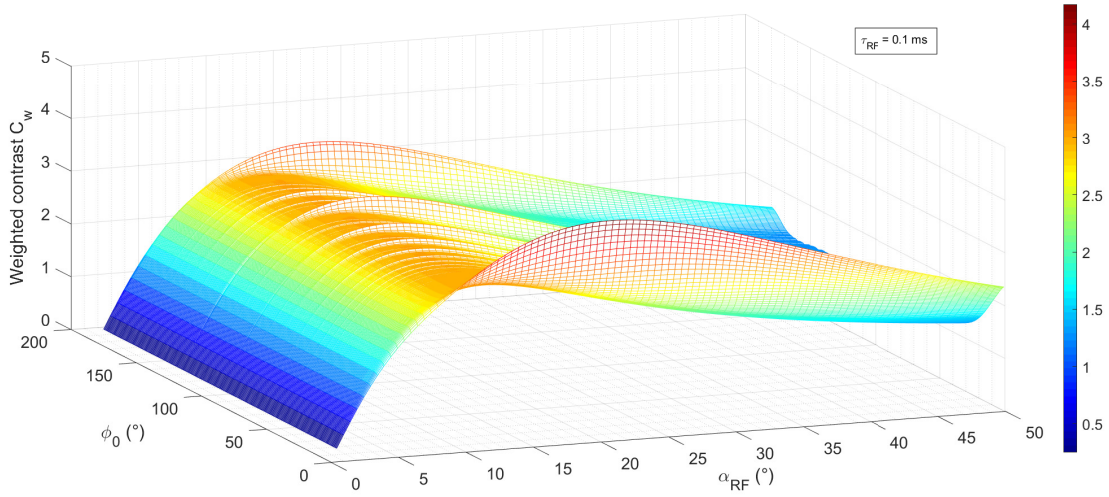

Figure 3.4: Weighted contrast simulated between the LC and its surroundings for a pulse duration of $\tau_{RF} = 0.1$ ms

The influence of α_{RF} and τ_{RF} on the normalised and weighted contrasts for an RF spoiling increment fixed to 90° is presented in FIGURES 3.5 and 3.6.

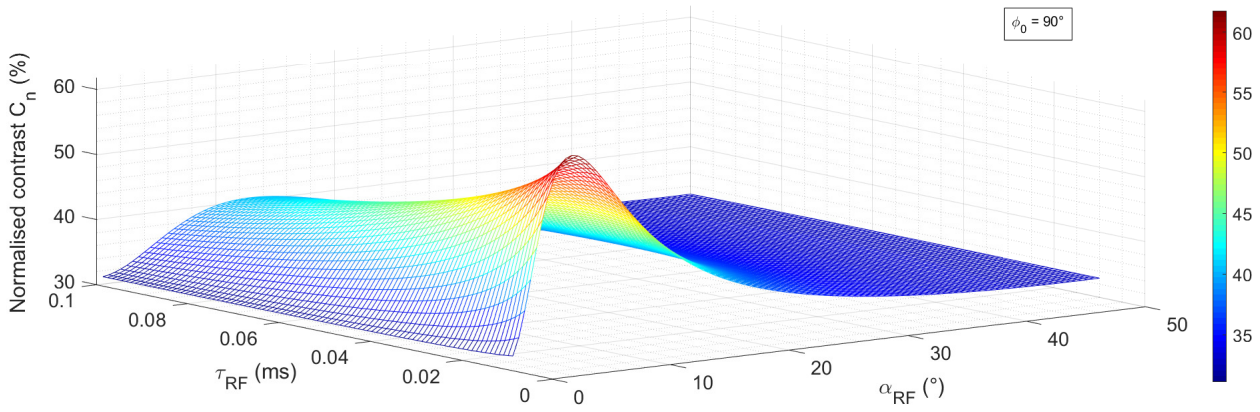

Figure 3.5: Normalised contrast simulated between the LC and its surroundings for an RF spoiling increment of $\phi_0 = 90°$

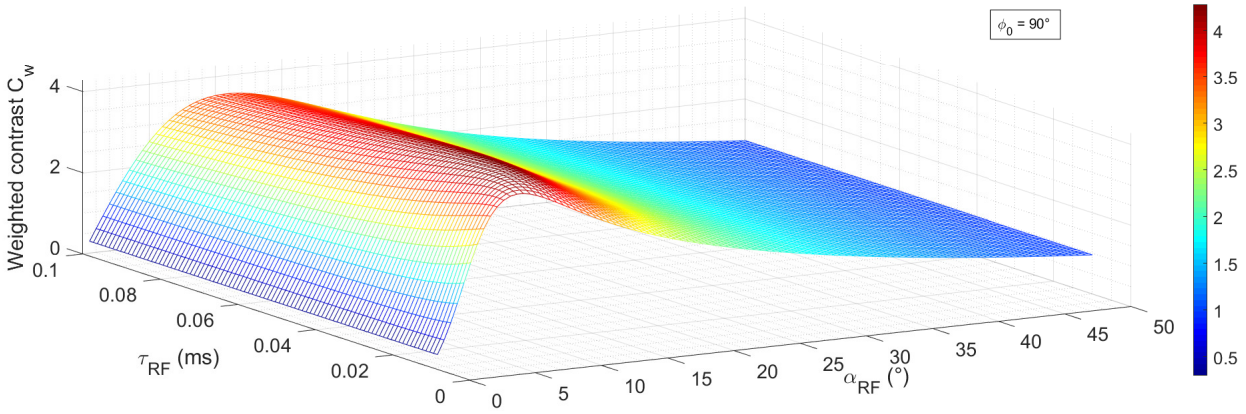

Figure 3.6: Weighted contrast simulated between the LC and its surroundings for an RF spoiling increment of $\phi_0 = 90°$

Given the normalised contrast predicted by simulation, FIGURE 3.5 suggests that the RF pulse duration should be made as short as possible with a flip angle of about 10 degrees in order to maximise the contrast between the LC and its surroundings. However, FIGURE 3.6 illustrates the drawbacks for such short pulses with a decrease in the weighted contrast for $\tau_{RF} < 0.02\,\text{ms}$ approximately by taking into account the SNR. In other words, the optimum saturation of tissues is achieved at the maximum RF pulse power reflected by the minimum RF pulse duration in the normalised contrast. But at the same time, this maximised saturation yields to the destruction of the signal in the LC which makes it non-optimal for visualisation purposes and results in a decrease in C_w.

Therefore, the optimisation of the LC visualisation is provided by a subtle trade-off between the contrast actually achieved through saturation effects and the SNR. The optimal configuration will thereby corresponds to an RF pulse duration as small as possible while considering this SNR concern

and a flip angle of about 5 to 20°. Note that all the simulated values are displayed without any restrictions on the maximum B_1 magnetic field which is an additional restriction to account for in the parameter optimisation.

The maximum weighted contrast values for which the parameters α_{RF} and τ_{RF} meet the $B_{1,max}$ constraint in FIGURE 3.6 are reported in TABLE 3.1. Since the highest contrast is achieved in the range of short RF pulse duration, τ_{RF} values ranging from 10 to 100 µs were considered. This table was established according to the following method implemented in the code `Optimal_Param.m`:

- τ_{RF} is ranging from 0.01 ms to 0.1 ms,
- For each τ_{RF}, the corresponding value of α_{RF} proving the highest contrast in terms of C_w, while giving rise to a nominal B_1 amplitude value smaller than $B_{1,max} = 20\,\mu T$ is determined.

τ_{RF} (ms)	α_{RF} (°)	$\alpha_{nominal}$ (°)	$B_{1,nomimal}$	$B_{1,actual}$ (µT)	C_n (%)	C_w
0.01	3.5	3	19.14	22.83	45.22	2.18
0.02	7.0	6	19.14	22.83	48.80	3.64
0.03	**10.5**	**9**	**19.14**	**22.83**	**47.62**	**4.01**
0.04	12.5	10	17.09	20.39	44.88	3.87
0.05	12.5	10	13.67	16.31	42.27	3.70
0.06	13.0	11	11.85	14.14	40.26	3.56
0.07	13.0	11	10.15	12.12	38.48	3.42
0.08	13.0	11	8.88	10.60	36.98	3.32
0.09	13.0	11	7.90	9.42	35.71	3.22
0.10	13.0	11	7.11	8.48	34.61	3.13

Table 3.1: Optimal flip angle values for each τ_{RF} based on simulations for $\phi_0 = 90°$, with maximum nominal B_1 amplitude specified at the scanner such as $B_{1,max} = 20\ \mu T$ and by maximising the weighted contrast.

In the latter table, the B_1 efficiency was accounted for and applied to the simulation results through the EQUATION (2.6) giving rise to a flip angle $\alpha_{nominal}$ that should be specified at the scanner. Note that the flip angle was constrained to integer values at the scanner. In the same way, the corresponding $B_{1,nominal}$ amplitude is reported and corresponds to the B_1 amplitude specified at the scanner as described by EQUATION (2.2). Because the restriction on the B_1 amplitude is a hardware limitation, the upper $B_{1,max}$ limit of 20 µT was applied to the $B_{1,nominal}$ amplitude, as reflected by values in TABLE 3.1. Therefore, simulations suggest that the optimal contrast is achieved for a short RF pulse with a B_1 amplitude maximised.

From this table, the optimal SPGR sequence was defined with a flip angle, a characteristic time constant and an RF spoiling increment: $\alpha_{RF} = 10.5°$, $\tau_{RF} = 30\,\mu s$ and $\phi_0 = 90°$.

A normalised contrast of 47.62% is expected when visualising the LC with such an optimal SPGR sequence, corresponding to the maximum weighted contrast value $C_w = 4.01$.

3.1.2 Experimental data analysis

From the acquired set of data, a first qualitative analysis was conducted to determine the general trend regarding the contrast and LC visualisation. This interpretation is relevant in the scope of the project since its aims are to understand the contrast mechanisms and provide an efficient tool for improving the targeting of the LC in a data set with the naked eye.

Data acquired during the experiment following the protocol presented in TABLE 2.3 emphasise the improvement of LC visualisation through the use of optimal parameters suggested by simulations. Images were displayed with interpolation between voxels as commonly used in SPM for visualisation. The same data, without interpolation, are presented in APPENDIX A.1 for both the anisotropic (Opt_FA7) with a voxel size of $0.6 \times 0.6 \times 3\,\text{mm}^3$ and isotropic acquisition (Opt_Iso_FA7) with a voxel size of $0.8 \times 0.8 \times 0.8\,\text{mm}^3$ based on the same sequence parameters.

Moreover, the position of the cursor and the zoom in the LC region were realised in order to provide the best visualisation of the LC structure. FIGURE 3.7 illustrates the data acquired with the sequence Opt_FA7 without zoom. Orange squares delineate the LC region displayed in the following figures with a zoom of $40 \times 40 \times 40\,\text{mm}^3$. The expected position of the LC is marked in red. The specific position of the FOV orthogonal to the LC is shown on the sagittal view. Note that in the following figures, the red arrows indicates the LC when it is properly visible.

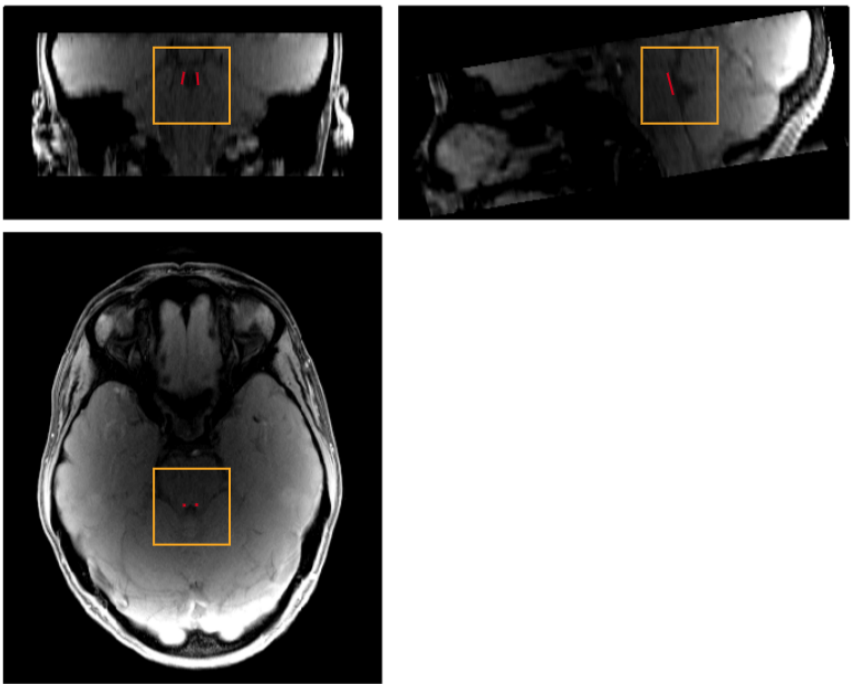

Figure 3.7: Data acquired with the Opt_FA7 protocol. The expected position of the LC is marked in red and the orange square denotes the zoom $40 \times 40 \times 40$ mm^3 on the LC region shown in the following figures

Increasing the BWT from 6 to 10 in the PD-weighted standard sequence enabled a better visualisation of the LC with a slight enhanced contrast, shown in FIGURE 3.8. More particularly, the left LC appears as hyper-intense in both the axial and coronal views. The contrast enhancement occurring at higher BWT is the result of the shorter t_0 characteristic time and therefore the higher B_1 amplitude required for the same pulse duration and flip angle. Moreover, by increasing the BWT less slices were affected by the aliasing artefacts at the edges of the FOV.

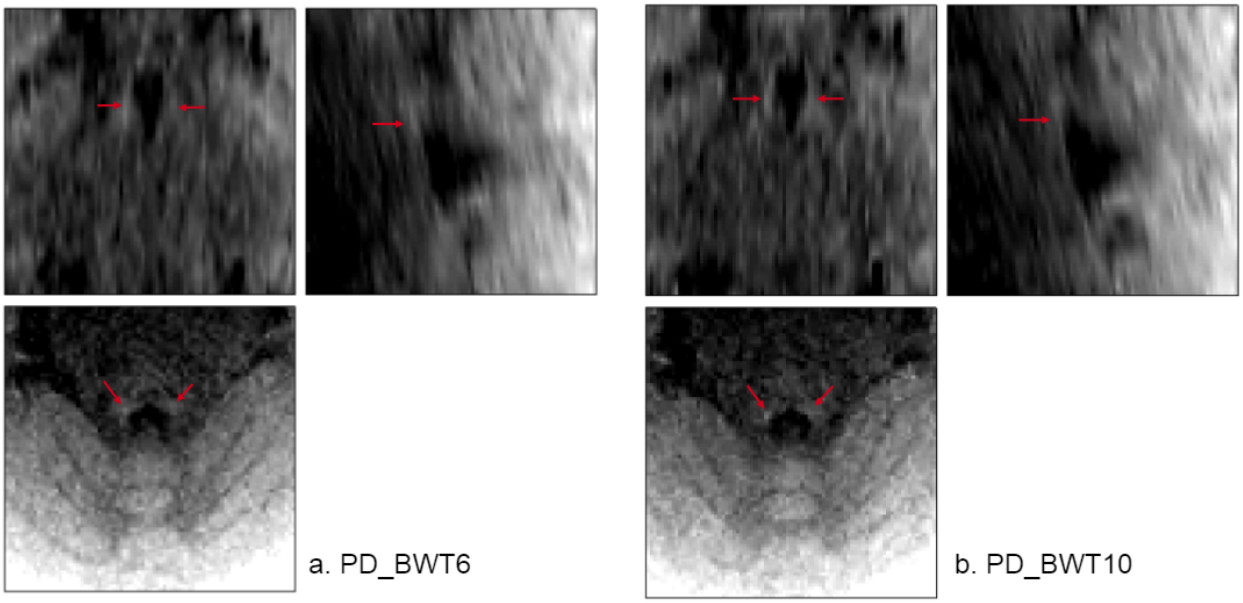

Figure 3.8: Data acquired with PD-weighted protocols with a. BWT= 6, and b. BWT= 10. Red arrows point at the LC. $40 \times 40 \times 40$ mm^3 zoom in the LC region.

Contrary to the PD-weighted case, increasing the BWT from 6 to 10 in the T_1-weighted sequence did not show significant improvement in the LC contrast (see APPENDIX A.2).

In agreement with simulation results, data generated through the optimal sequence 'Opt_Aniso' seems to improve the LC visualisation compared to standard T1- and PD-weighted sequences. FIGURE 3.9a shows the LC structure hyper-intense in each of the three view. Furthermore, the impact of the RF spoiling increment is relatively small as illustrated in FIGURE 3.9b. This observation is consistent with the numerical simulations (FIGURE 3.3). While the axial and sagittal views allow a similar delineation compared to the optimal protocol, the coronal view do not present clear appearance of the locus cœruleus.

Among the data acquired, the clearest depiction is given by the sequence corresponding to optimal parameters while using a flip angle of $\alpha_{RF} = 11^\circ$, as FIGURE 3.10a illustrates. However, in this case the visualisation appeared to be hampered by participant motion between the positioning of the FOV (carefully aligned with the long axis of the LC) and this acquisition. This shows the limitation of the anisotropic acquisition which requires a specific FOV position, not compatible with participant movement. FIGURE 3.10b provides the isotropic data acquired with the optimal set of parameters given the constraint on maximum $B_1 = 20\,\mu$T. Comparing the latter to the anisotropic acquisition with the same parameters, despite the notable decrease in the image SNR, a visible improvement of the LC delineation can be highlighted in the coronal view where this structure can be visualised along its full length.

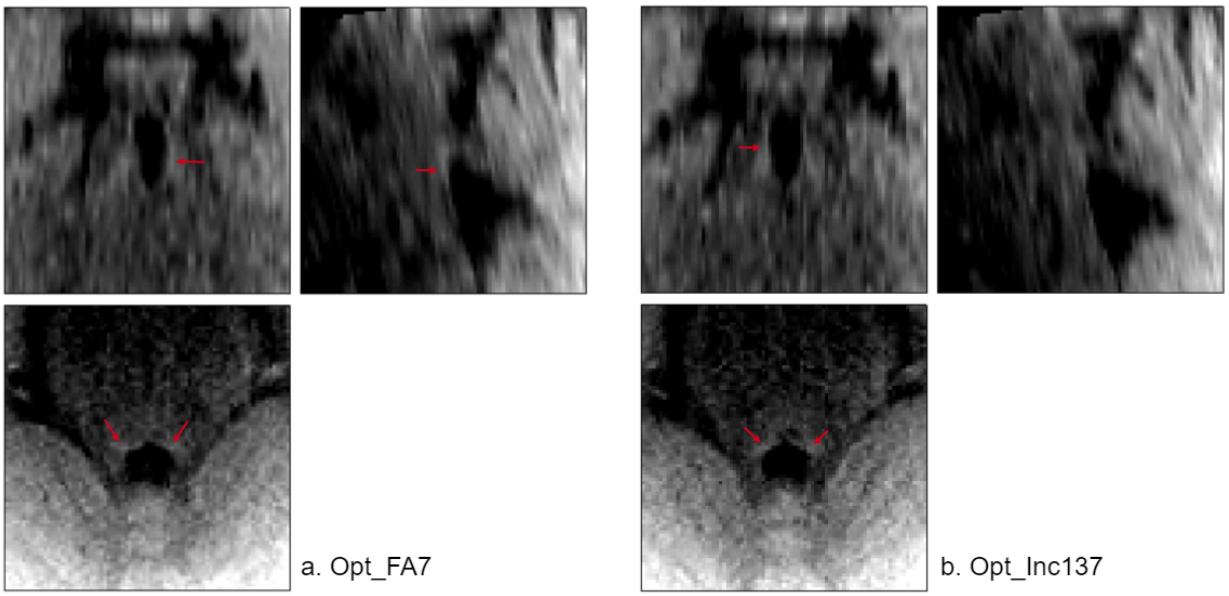

Figure 3.9: Data acquired with a. optimal anisotropic protocol, b. optimal anisotropic protocol with $\phi_0 = 137°$. Red arrows point at the LC. $40 \times 40 \times 40$ mm^3 zoom in the LC region.

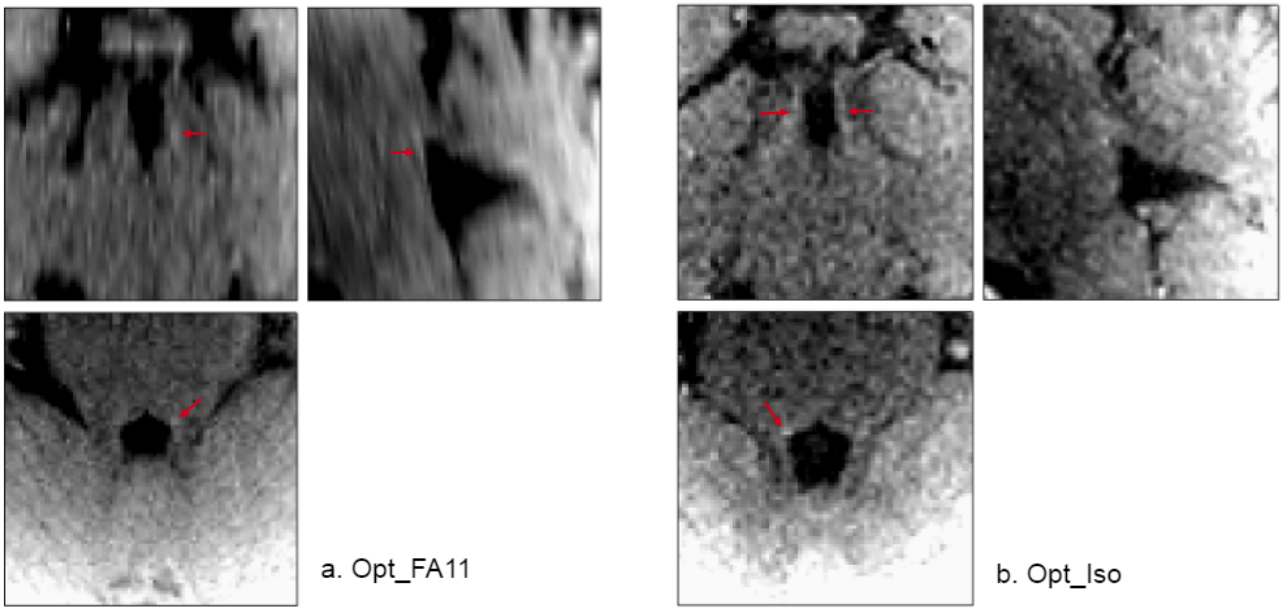

Figure 3.10: Data acquired with a. anisotropic optimal protocol with $\alpha_{RF} = 11°$, b. isotropic optimal protocol. Red arrows point at the LC. $40 \times 40 \times 40$ mm^3 zoom in the LC region.

Finally, whole brain acquisitions shown in FIGURE 3.11 did not dramatically alter the contrast observed while increasing the acquisition time by a considerable amount. The main advantage of these sequences is the larger spatial coverage that allows other structures of interest to be visualised. These acquisitions also had isotropic resolution. This characteristic provides better resolution along the long axis of the LC and improves its alignment with other data types such as functional MRI. In addition, the acquisition through a sinc non-selective pulse showed slightly better LC delineation than the one acquired with the rect non-selective pulse.

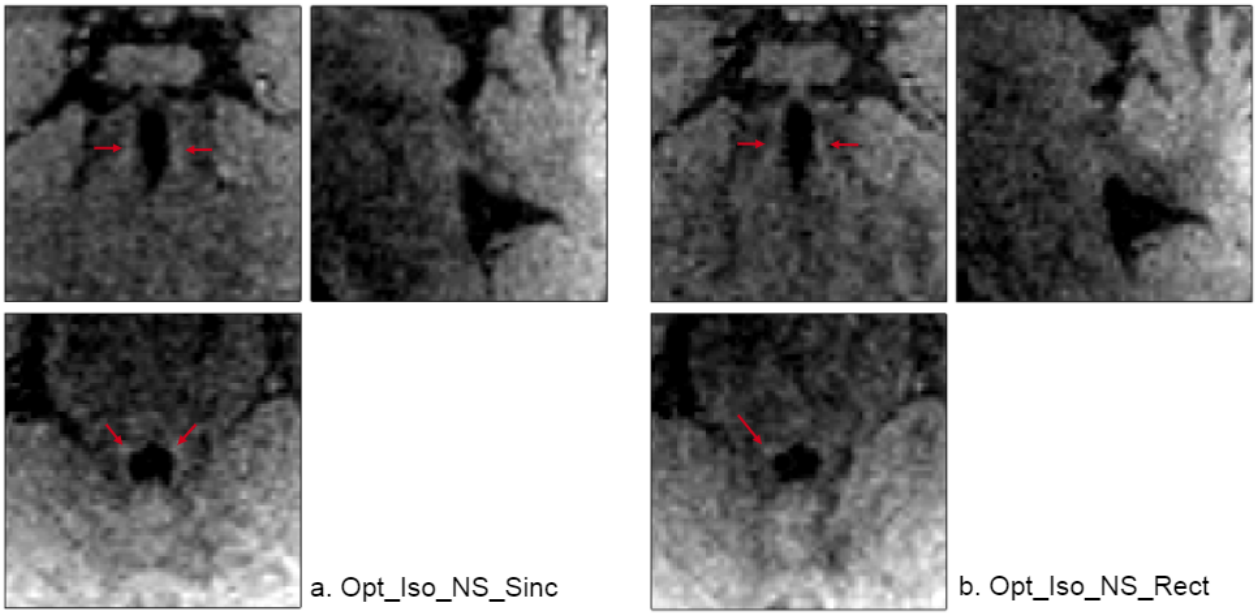

Figure 3.11: Data acquired through the non-selective protocols a. with a sinc pulse, and b. with a rect pulse. Red arrows point at the LC. $40 \times 40 \times 40$ mm^3 zoom in the LC region.

From this qualitative analysis, the optimal set of parameters determined through both simulations and scanner specifications maximising the achievable B_1, i.e. $\alpha_{\text{nominal}} = 11^\circ$, $\tau_{\text{RF}} = 30\,\mu\text{s}$, $\phi_0 = 90^\circ$, seemed to improve the contrast and provide a better visualisation of the LC compared to standard protocols. These results are in agreement with simulation predictions. The voxel size has also an important impact on the LC due to its cylindrical shape. It is however not clear which resolution, i.e. anisotropic or isotropic, should be preferred. Quantitative analyses were subsequently carried out to provide a more objective assessment (SECTION 3.1.3).

▸ Super-resolution outputs

The use of the Super-resolution algorithm drastically improved the data quality. FIGURE 3.12 illustrates the impact of the algorithm on data providing the clearest LC visualisation, i.e. acquired with the sequence Opt_FA11. Data is displayed without interpolation between voxels in order to point out the resolution improvement. In comparison with the original data, the result coming from the Super-resolution algorithm contains much less noise which enables a better depiction of the various brain structures. This effect can be particularly noticed when looking at the cerebellum in the sagittal view. Moreover, the increase in resolution allows a smoother representation of brain structures at such small scale while still preserving anatomical detail.

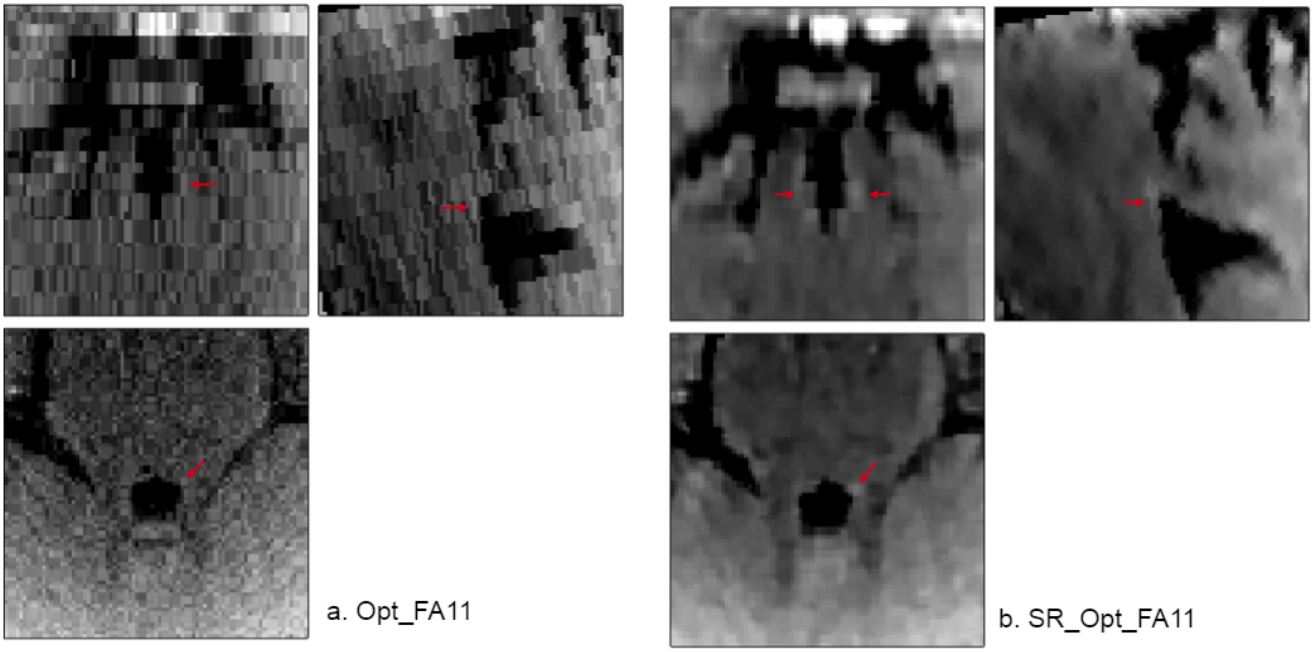

Figure 3.12: Impact of the Super-resolution algorithm on the data resolution. a. Original data Opt_FA11, b. Processed data Opt_FA11 with the SR algorithm (voxel size $0.6 \times 0.6 \times 0.6$ mm^3). Images displayed without interpolation between voxels. Red arrows point at the LC. $40 \times 40 \times 40$ mm^3 zoom in the LC region.

3.1.3 Model validation

In this section we seek to assess the agreement between our model predictions and the experimental observations. This will allow the validity of the assumed tissue properties to be investigated.

To proceed to this model validation, the contrast was first evaluated in the region of interest using the computed masks. The extracted values were then compared to the simulation predictions. Presumed optimal parameter values were computed according to the maximisation of the weighted contrast. However, because of its definition, the C_w variable presents arbitrary units complicating the quantitative comparison with empirical data. In fact, because of the difference in voxel size across protocols, the experimental data are characterised by different level of signal whether the acquisition was anisotropic or isotropic. By computing the weighted contrast and therefore multiplying the normalised contrast by the signal intensity in the LC makes the isotropic acquisitions incomparable to the anisotropic ones. Following that logic, FIGURE 3.13a depicts the weighted contrast measured in the anisotropic experimental data. Note the high values in C_w referring to the arbitrary units previously mentioned.

Because of this counter-intuitive result, the analysis of the normalised contrast C_n was preferred. FIGURE 3.13b evaluates the normalised contrast values for each sequence of the protocol (TABLE 2.3) experimentally measured. The comparison with the simulation prediction for two different bound pool fraction size for the surroundings is illustrated in FIGURE 3.13c. Note that the value of $f_{surr} = 0.3$ corresponds to the bound pool fraction initially assumed within the developed model on which the focus is made at first. The detailed weighted and normalised contrast values for each sequence either experimentally measured or predicted by simulation are found in APPENDIX B.1.

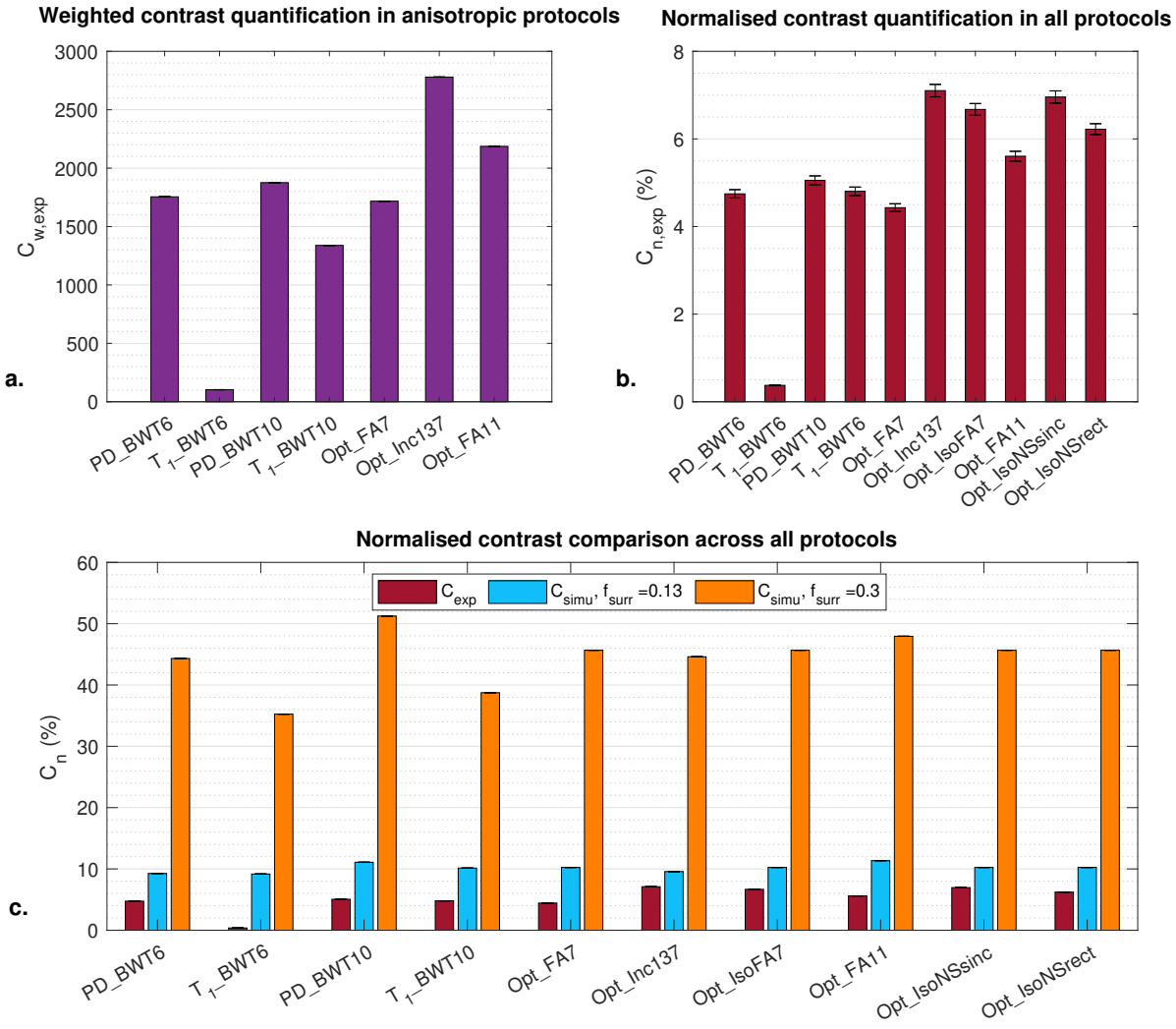

Figure 3.13: Contrast quantification in the LC region. a. Weighted contrast quantification measured in the anisotropic protocols, b. Normalised contrast quantification measured in all protocols, c. Normalised contrast comparison across all protocol either measured experimentally or predicted by simulation with $f_{\text{surr}} = 0.13$ and $f_{\text{surr}} = 0.3$

The first observation refers to the weighted contrast in FIGURE 3.13a where Opt_FA11 was expected to maximise the C_w variable while in practice Opt_Inc137 shows a higher value. However, from data Opt_FA7 and Opt_FA11, an increase in the flip angle of the RF pulse seems to indicate a better visualisation of the LC, as predicted.

By focusing the analysis on the normalised contrast, FIGURE 3.13c shows huge discrepancies of about one order of magnitude between simulation predictions with $f_{\text{surr}} = 0.3$ and experimental results. This significant difference may suggest an inaccuracy in the model representation.

Third, the propagated error on the measured normalised contrast is reported as relatively low for each and every protocol in FIGURE 3.13b.

Fourth, increasing the BWT of both the PD- and the T_1-weighted sequences from 6 to 10 provides a respective greater C_n value. However, the measured contrast for T_1_BWT6 is unexpectedly low. Given its small variance and the associated predicted contrast, this experimental result may indicate an inaccurate representation of the sequence characteristics. Therefore, T_1_BWT6 was rejected from

the analysis as an outlier. Furthermore, PD_BWT10 was predicted by simulations with the highest normalised contrast across protocols (see TABLE 2.3) while this trend does not appear in the acquired data.

Fifth, it was expected from simulation that relative differences between so-called optimal protocols (Opt) would appear as small. However, notable disparities can be observed experimentally in FIGURE 3.13b where Opt_Inc137 is reported with a surprisingly high C_n value on the contrary to Opt_FA7 which was believed to provide a slightly better normalised contrast from simulations. Similarly, Opt_FA11 was supposed to provide a higher normalised contrast than Opt_Inc137 but does not appear as so in practice.

Finally, the anisotropic and isotropic acquisitions with equal parameter values were predicted with an identical normalised contrast while the impact of the voxel size is clearly shown experimentally through sequence Opt_FA7 and Opt_IsoFA7 in FIGURE 3.13b. The same observation can be made regarding the pulse shape which seems to impact the LC visualisation whether the excitation pulse is a sinc or a rect pulse. However, the isotropic acquisitions relative to the same flip angle $\alpha_{RF} = 7^\circ$ (Opt_IsoFA7, Opt_IsoNSsinc and Opt_IsoNSrect) seem to form a cluster with high measured normalised contrast.

The validity of the model was also assessed with a correlation analysis illustrated in FIGURE 3.14.

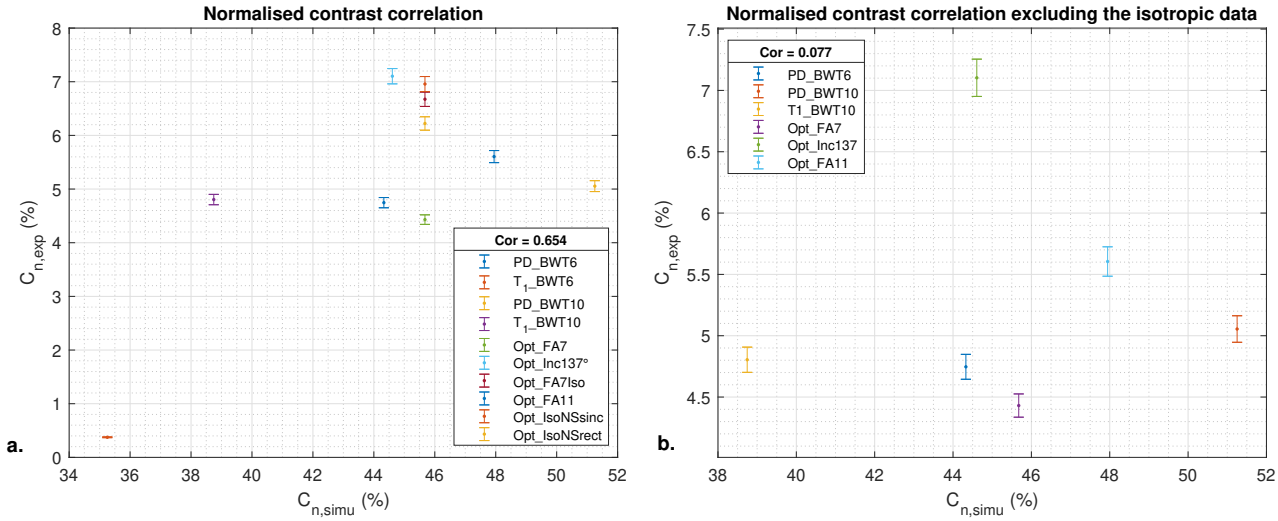

Figure 3.14: Predicted and measured normalised contrast correlation between a. all sequences including the outlier, b. all sequences excluding the isotropic and outlier data

The correlation between the C_n normalised contrast values of each sequence is first represented in FIGURE 3.14a. with a correlation coefficient of 0.654. Although this value is relatively large given the low quality and noisy experimental data, much of the correlation seems to be driven by the extremely low contrast evaluated in the T_1_BWT6 acquisition. This data was thereby discounted from the correlation analysis as an outlier. Moreover, given the heterogeneity in terms of resolution resulting in differential signals level and the poor delineation of the LC in the data set, the focus was made on the study of the anisotropic sequences according to both simulations and qualitative analysis, i.e. excluding the isotropic protocols Opt_Iso, Opt_Iso_NSsinc, Opt_Iso_NSrect. FIGURE 3.14b. illustrates the correlation relative to the anisotropic optimal and standard sequences. It appears that the correlation

coefficient drops to 0.077 when not driven by the outlier and the isotropic acquisitions. This low value may be interpreted as an inaccurate model.

FIGURE 3.15 shows the relationship between the measured and predicted weighted contrasts in the anisotropic data set only.

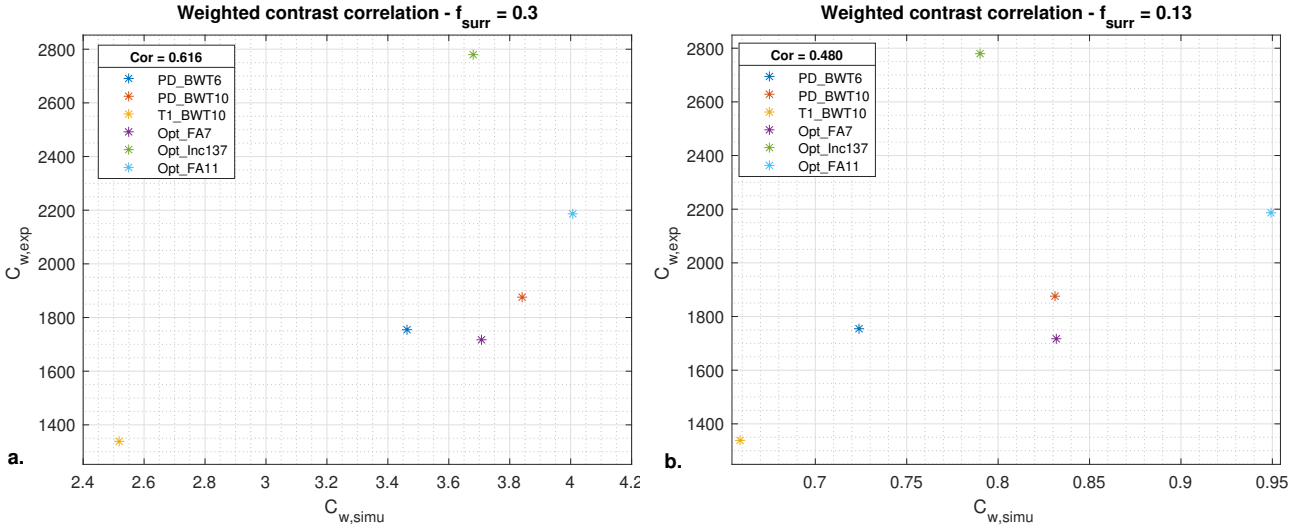

Figure 3.15: Predicted and measured weighted contrast correlation between the anisotropic sequences excluding the outlier with different bound pool fraction sizes: a. $f_{\text{surr}} = 0.3$, b. $f_{\text{surr}} = 0.3$.

The analysis of the correlation in weighted contrasts focuses on the anisotropic data excluding the outlier given the justifications previously stated. In the current model implementation, that is to say with $f_{\text{surr}} = 0.3$, the correlation between experimental and predicted data is of 0.616 (FIGURE 3.15a). This value, much higher than the correlation in normalised contrast in the same conditions, may indicate a reasonable representation of the trend in weighted contrast by the model. However, one have to keep in mind the small data set available and the poor quality in the acquisitions.

Given the multiple evidences collected regarding the imprecision of the current model representation of the LC contrast mechanisms, the potential sources of discrepancies were studied. The impact of tissue-dependent parameter previously defined was investigated as any errors in tissue properties would alter the simulated signals and lead to discrepancy between simulation and experiment. The choice was made on the bound pool fractional size parameter characterising the surroundings given the low precision regarding its initial estimation from the PSR map (FIGURE 1.17B) of Trujillo et al. [42]. Moreover, differential magnetisation transfer effects are likely to be a primary source of contrast between the LC and surrounding tissues, implying a large influence of the compartments fraction size on the signal intensities. It was found through simulations that the parameter f_{surr} had a huge impact on the signal in the surroundings and therefore in the resulting predicted contrast. By decreasing the fractional size value in the surroundings, the expected normalised and weighted contrast drop significantly while still leading to the same optimal sequence parameter values according to simulations. FIGURE 3.13c illustrates the considerable decrease in normalised contrast expectations with a $f_{\text{surr}} = 0.13$ compared to the simulations with $f_{\text{surr}} = 0.3$. The corresponding predicted values are reported in APPENDIX B.1 with a median value of about 10% for the normalised contrast across

the entire data set. This parameter value leads to more relevant normalised contrasts which seems in greater absolute agreement with the experimental results, suggesting that the first estimation of the bound pool fraction size was overestimated. Regarding the weighted contrast C_w, FIGURE 3.15b illustrates the correlation within anisotropic acquisitions between experiment and simulation. The coefficient of correlation decreases to 0.48 compared to the previous situation where the f_{surr} was set to 0.3 but is still maintained at a decent value. However as already mentioned, no actual conclusions can be drawn from this correlation coefficient being unrepresentative of as such small data set.

Based on these results, f_{surr} was set to 0.13 for the modelling of the SPGR sequence including MT preparation pulse. This new assumption is suggestive of a better alignment with experimental results (FIGURE 3.13c) while remaining consistent with literature and to the statement that LC is characterised by a lower bound pool fraction than its surroundings. Nonetheless, this value stays an important hypothesis and still requires further evidences that this bound pool fraction size is more representative of the MT effects in the surroundings.

3.2 Optimisation of SPGR sequence with MT pre-pulse: simulation

3.2.1 Simulation results

In order to validate the modifications in the `EPGX_GRE_MT.m` code for including the saturation pulse prior to each excitation pulse, a sanity check was performed on the `Simu_MT.m` code. The latter consisted in considering a null B_1 magnetic field amplitude for the pre-pulse, implying that no MT saturation pre-pulse was played out, and observing if the signal amplitudes obtained with the `EPGX_GRE_prepMT.m` code were identical to the ones reported by the simulation without MT pulse with the original `EPGX_GRE_MT.m` code. FIGURE 3.16 shows identical signal amplitudes were obtained with both simulation outputs, confirming the correct implementation of the desired sequence configuration. The signals in the LC and in its surroundings expected by the simulation of the classic SPGR sequence are denoted by 'LC' and 'Surr', respectively while they are called 'LC_{MT}' and '$Surr_{MT}$' in the new MT-weighted simulation, albeit with a pre-pulse of zero amplitude.

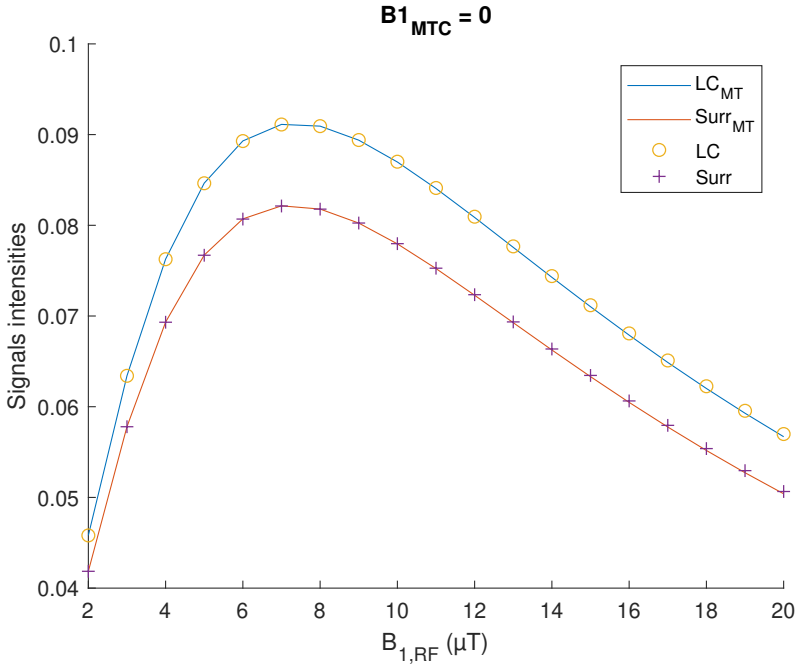

Figure 3.16: Matching between simulations without the implementation of an MT pre-pulse and with the implementation of a null MT pre-pulse for the same set of RF parameters

▸ Optimal parameters

The EPG-X simulations realised with the MATLAB code `Simu_SPGR_MT.m` allowed the optimal parameter values characterising the SPGR sequence with MT pre-pulse for LC visualisation to be determined. Note identical tissue properties were used here as for the SPGR simulations with no pre-pulse with the exception of the fractional bound pool size of the surroundings being reduced to 0.13 based on the previous empirical results.

The parameter values suggested as optimal by the simulations when spanning the 7-D space and using C_w as the optimisation criterion were:

- $B_{1,RF} = 6\,\mu T$;
- $\tau_{RF} = 0.1\,ms$;
- $\phi_0 = 90^\circ$;
- $B_{1,MTC} = 26\,\mu T$;
- $f_{MTC} = 10\,kHz$;
- $\tau_{MTC} = 0.2\,ms$;
- $TR_1 = 14.7\,ms$.

According to theoretical relations from TABLE 1.1, the corresponding flip angles for the RF and the MT pulses are computed from the value of the B_1 amplitudes and τ_{RF} or τ_{MTC} respectively. After considering the RF pulse as a sinc pulse and the MT pulse as a Gaussian one, the corresponding optimal flip angle values are given by $\alpha_{RF} = 9.2^\circ$ and $\alpha_{MTC} = 199.79^\circ$. The total duration of respective pulses are given by $T_{RF} = 6 \cdot 0.1 = 0.6\,ms$ since the sinc pulse is specified with a BWT of 6 and $T_{MTC} = 7.434 \cdot 0.2 = 1.49\,ms$. The expected normalised and weighted contrasts are respectively equal to $C_n = 14.91\%$ and $C_w = 1.09$. The current MT-weighted sequence used at WCHN is characterised by simulations with the expected values such as $C_n = 12.32\%$ and $C_w = 0.39$. The optimal set of parameters suggested by the simulations thereby provide a theoretical improvement in the contrast currently achieved through standard sequences.

The set of optimal parameters determines the global maximum in weighted contrast in the 7-D plan of parameter values investigated. The impact of varying each parameters around its value at this global maximum was then studied. To do so, six parameters out of the seven ones were kept fixed to their respective optimal value while the seventh was varied within its range of values. FIGURE 3.17 depicts the impact of the pulse parameters $B_{1,RF}$, τ_{RF}, ϕ_0, $B_{1,MTC}$, τ_{MTC}, f_{MTC} and TR_1 on the weighted contrast around this global maximum. The influence of these parameters on the respective signals in the LC and surroundings and on the normalised contrast are given in APPENDIX C.1 and C.2.

Through these results, simulations suggest that one should use the longest possible duration for the excitation pulse and a relatively small flip angle of about 9 degrees. The RF spoiling increment of $\phi_0 = 90^\circ$ was preferred to the one currently used in standard protocols. However, the impact of this parameter on the signal intensities and the resulting contrast seems quite low (FIGURE 3.17b).

The optimal MT pulse recommended is characterised with maximum B_1 amplitude and off-resonance frequency. It is also worth noticing that because of the timing restrictions implemented in EQUATIONS (2.8) and (2.10), only two values of τ_{MTC} out of its specified range were possible when TR_1 was fixed at the global maximum value as illustrated in FIGURE 3.17d. In these conditions, the duration of the MT pre-pulse is suggested to be the longest possible which results in this case in a relatively small value of $\tau_{MTC} = 0.2\,ms$, thereby involving a total duration of 1.4 ms given the Gaussian pulse shape. As a result, the MT pre-pulse is indicated as powerful but with a relatively short duration. Finally, the delay between the saturation and the excitation is given by $TR_1 = 14.7\,ms$ allowing an relatively long period for the magnetisation exchange processes to occur regarding the

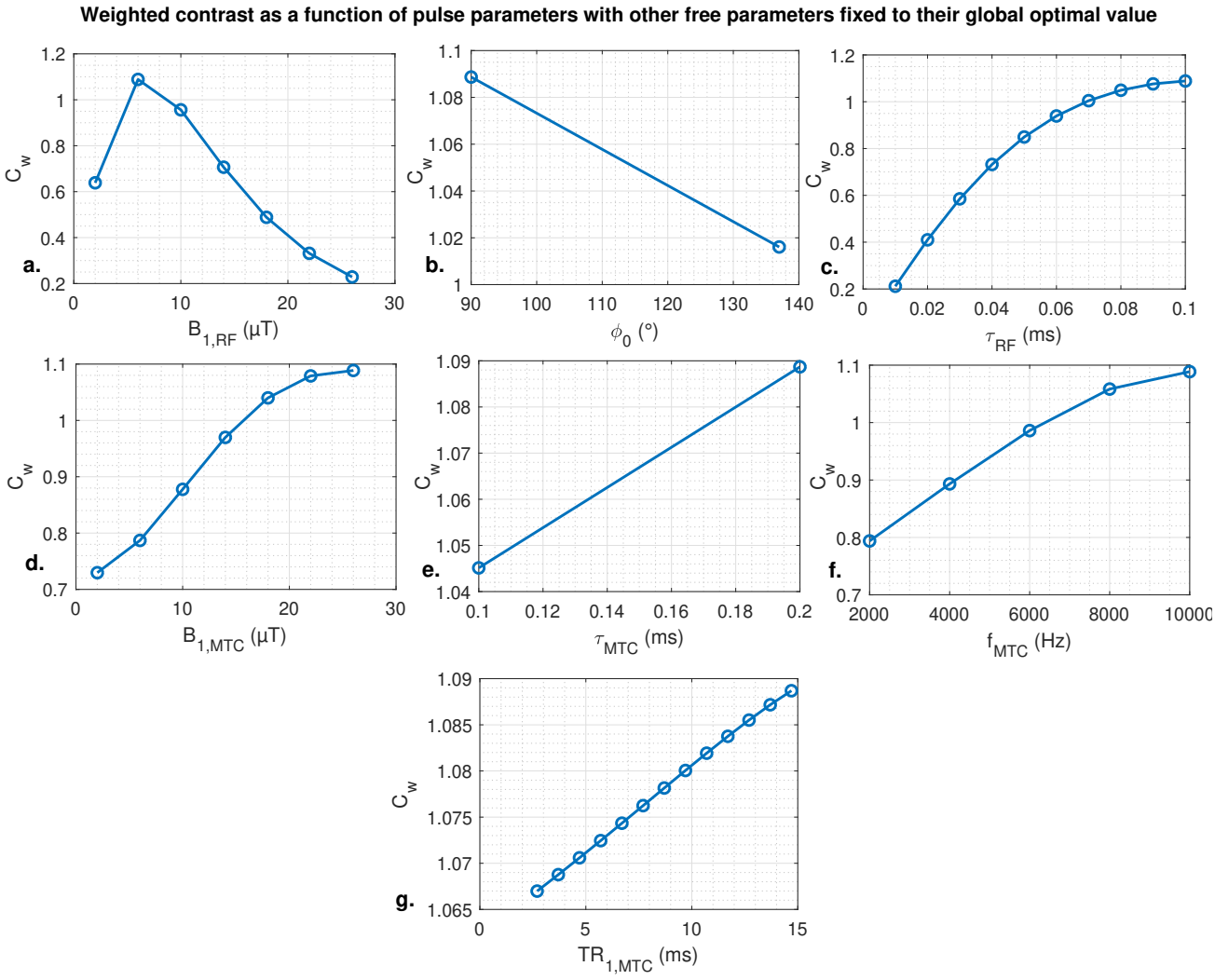

Figure 3.17: Weighted contrast as a function of $B_{1,RF}$, τ_{RF}, ϕ_0, $B_{1,MTC}$, τ_{MTC}, f_{MTC} and TR_1 around its global maximum value

repetition time of 24.5 ms. Note the optimal values of τ_{RF}, $B_{1,MTC}$ and f_{MTC} reaching their upper limit in the range of permitted simulated values given the restrictions imposed by the implementation.

Chapter 4

Discussion

The WCHN provides protocols allowing the visualisation of the LC but the underlying contrast mechanisms are yet not fully understood. Many properties are thought to be involved in the contrast generation processes such as the iron content, the neuromelanin or the macromolecular composition of this noradrenergic structure but the understanding of their common interactions is still under investigation and requires further researches. In this context, the optimisation of MRI sequences for targeting the LC is a real challenge given the lack of knowledge and characterisation of the LC structure. However, the description of the LC and its surroundings as two-compartment models ruled by magnetisation transfer effects seems to be the main justification for the hyper-intense contrast in MR images. Here this mechanism was studied in the scope of spoiled gradient echo sequences either including or not MT pre-pulse with the aim of improving our knowledge about contrast mechanisms in the LC and subsequently optimising its visualisation.

4.1 Optimisation of SPGR sequence: simulation and validation

Through the simulation results, the SPGR sequence characterised by the highest power excitation pulse while being restricted by the scanner limitations was predicted to provide an optimal contrast between the LC and its surroundings. This power maximisation is indicated by the increase in the BWT, the B_1 amplitude and the short pulse duration. This suggests that maximising the saturation effect by using high power pulse helps increasing the normalised contrast. However, through the weighted contrast, it has been noticed that maximising the saturation would result in small signal intensities although the contrast is improved. Therefore, the visualisation of the LC would not be optimal in this configuration (FIGURE 3.6). A trade-off has to be realised between SNR and contrast. The RF spoiling increment of the SPGR sequence showed low impact on the simulated contrast as against the flip angle and the duration of the pulse (FIGURES 3.3 and 3.4). The predicted contrast values were nonetheless already predicted as large with one order of magnitude higher compared to the findings of Tona et al. at 3T [41].

The qualitative analysis of the experimental data collected based on the suggested optimal results seemed to confirm these predictions by providing a clear delineation of the LC structure. In fact, maximising the power by reducing the pulse duration, or equivalently by increasing the BWT, and increasing the flip angle was visualised as an improvement of the contrast as suggested by simulations. While there is insufficient experimental data to validate this observation with strong evidence, the relative comparison of the optimal sequence Opt_FA11 with existing ones currently used at the WCHN seemed to show an improvement in LC visualisation.

Furthermore, the resolution of the acquisition was also studied through the use of identical optimal sequences either with anisotropic or isotropic voxel sizes. The main advantage of anisotropic voxels with high in-plane resolution is their matching features with the cylindrical shape of the LC. Therefore, the SNR in these voxels is maximised which theoretically improves the visualisation of the structure. As experimental results demonstrated, these kind of acquisitions are highly sensitive to the position of the field of view and thereby the participant motion, which makes it unsuitable for lengthy acquisition protocols. This presumably explains the difference in intensity between the left and the right LC visualised through the optimal sequence with a flip angle of 11° (FIGURE 3.10a) and is likely to have introduced some variance into the data hindering comparison with our experimental predictions. Still, this acquisition provides quite convincing results on the contrast enhancement with a strong and brief excitation pulse. On the other hand, isotropic acquisition which are expected to provide increasing resolution at the cost of longer scan time and reduced SNR showed promising depiction of the whole length of the LC along the coronal plane (FIGURE 3.10b). Extending the isotropic observations to non-selective acquisitions would suggest that the visualisation of the LC could be achieved simultaneously to the characterisation of other brain structures allowing whole brain analyses.

The voxel size was not accounted for within the current implementation of the EPG-X framework which makes its impact on different signals difficult to quantify. The main difference between such aniso-/iso-tropic acquisitions lying in the SNR, the quantification of the noise within these data could help to better understand the impact of resolution on LC visualisation. In the scope of this project, the noise was not further investigated given the complexity of this procedure for MR data acquired with array coils and using parallel imaging but the resulting conclusions were drawn with care accounting for the differential data quality. Moreover, the Super-resolution algorithm used as a tool for denoising and increasing the data resolution showed convincing results in the improvement of data quality. The use of this algorithm seems very efficient in the process of LC visualisation. Still, one has to be careful on any potential biases introduced through such data processing.

Furthermore, the experimental results presented have to be put in perspective with the fact that only a single participant was tested, making these observations difficult to generalise. In fact, the LC population is known to exhibit numerous variations across the lifespan either intra- or inter-subjects which makes the optimisation of its visualisation even more challenging.

The evaluation of the signal intensity values in the tissues was realised by using a mask computed based on the combination of all acquired data. As a consequence, this method lower the bias that could have been introduced by applying a mask specific to each sequence. This choice was considered as the most robust when comparing contrast across various protocols. However, given the multitude of image processing steps, nothing excludes an erroneous definition of these masks thereby impacting the quantitative analysis.

The quantification of contrast achieved in the available data set provided several pieces of evidence suggesting that the initially developed model was not as representative of the LC contrast mechanisms as it was supposed to be. The main evidence is the order of magnitude lower C_n values obtained experimentally than predicted by simulations results, which indicates an over-estimation of the normalised contrast. In fact, the experimentally measured values were on average in line with those from Tona et al. [41]. Second, the bound pool fraction size of the surroundings f_{surr} was initially over-estimated. By reducing it to an assumed value of 0.13, a greater agreement between the simulation and the experiment was highlighted (FIGURE 3.13c) while the correlation coefficient with the predicted weighted contrast was kept at a decent value (FIGURE 3.15). Finally, a third evidence consists in the low correlation between experimental and predicted normalised contrast across anisotropic sequences when

excluding T_1_BWT6 (FIGURE 3.14b). This has still to be put in perspective with the low amount of experimental data.

In the perspective of a further validation of the SPGR model, additional experiments should be performed in order to assess with more confidence the model representation. For generating controlled variance in the data and thereby having better insight of the effect of sequence parameters on measured contrasts, successive isotropic sequences could be acquired while varying exclusively the B_1 amplitude of the RF excitation pulse, with all other parameters fixed. The choice of isotropic sequence is justified by its robustness to participant motion and difficult positioning of the FOV. Furthermore, the acquisitions realised with this resolution showed higher contrasts and better delineation of the LC along its entire length.

These findings and their related interpretation are contingent on the assumptions made regarding tissue properties. The investigation of the potential sources of discrepancies is therefore a crucial point to proceed to the establishment of a new model but highly challenging. In fact, the tissues description as a two-compartment model neglect several biological phenomena potentially impacting the contrast. These subjects are out of the scope of this project but surely require further investigation given the limited information available. However for most studies a two pool model has proved sufficient, albeit requiring accurate characterisation of the tissue properties. Therefore determination of this tissue parameter values arguably dictates the accuracy of the model representation. Given the multitude of parameters involved and their potential correlated influence, this analysis is not straightforward and would require a much deeper focus in future work. Each parameter is individually discussed as follows:

▸ T_1 relaxation time:

The analysis of MPM data provides confident values of T_1 relaxation times in both LC and surroundings given the multiple runs on the three participants considered. In addition, these values were confirmed by the T_1 values reported by literature [42, 46]. However, no insight was provided about the relaxation times within the respective pools of each tissue. It is still not clear how the relaxation times are affected within such two-compartment structures, which values are best at capturing the respective pools and whether the impact on simulated signals is significant or not.

▸ T_2 relaxation time:

While there is evidence for their precise values, the transverse relaxation times of the free pools were determined from the literature in the LC and assumed in the surroundings given the lower bound provided by quantitative T_2^* values. The assumption in the surroundings was in keeping with values reported in a 3T study even though the latter did not cover brainstem structures [45].

As previously, a distinction between compartments is required but had to be assumed. Because of the MT effects, the T_2 times in the bound pool are assumed to be so small (in the order of microseconds) that their transverse magnetisation is negligible. An additional assumption must be made on the T_2 value of the bound pool in order to compute the absorption lineshape G which dictates the saturation through a Super-Lorentzian function [22]. Here, a value of $T_{2,b} = 12\,\mu s$ has been used based on the default setting used by Malik et al. [31]. This value was in line with previous studies for which the measured $T_{2,b}$ was not significantly varying across brain structures [39]. Although the impact of $T_{2,b}$ on the predicted absorption curve is considerable (APPENDIX D.1), the downstream consequence on the predicted normalised contrast is not particularly large. In fact, a 5 fold increase

in $T_{2,b}$ time results in an increase of 1% in the predicted normalised contrast when considering the optimal protocol. The effect of the relaxation time T_2 in the bound pool may thereby be considered as small.

▸ Fractional bound pool size, f:

The fractional bound pool size in the LC was obtained from literature based on a quantitative study of the LC and is presumably a good representation of this tissue pool sizes. The same statement can not be asserted regarding the surroundings fraction value given the coarse estimation made from the pool size ratio map provided by this study [42].

This parameter has been shown to have an important impact on the signal intensities and thereby the predicted contrast. In fact, the higher the fractional bound pool size of the surroundings, the higher the predicted contrast by simulation, which is in line with theoretical expectations related to MT effects. The quantitative analysis provided evidence regarding the over-estimation of the initial bound pool fraction size in the surroundings as C_n decreased towards the experimental values as f_{surr} was reduced. However, this value must not reach a value as low as the one in the LC. Therefore, a value of f_{surr} was found to achieve a better alignment of simulation predictions with experiment (FIGURE 3.13c), to be consistent with the PSR map from Trujillo et al. (FIGURE 1.17) and to maintain a reasonable correlation coefficient between predicted and measured C_w values (FIGURE 3.15b).

▸ Exchange rate, k_{ab}:

A unique value of the exchange rate from compartment b to a was found in literature for characterising the LC. The exchange rate k_{ba} is related to k_{ab} by the EQUATION (1.2). However, computing k_{ab} from k_{ba} required the knowledge of the pool size ratio. k_{ab} was then derived from the k_{ba} value defined by literature with a pool size ratio of 0.09 in the LC and assumed to be the same for the two tissues.

It has been shown during the project that the variation of this parameter had a considerable impact on the predicted contrast indicating the importance of the exchange direction. Through simulations, it was observed that the predicted normalised contrast values were increased by approximately 10% when the exchange rate from compartment a to b was multiplied by a factor 10.

▸ B_1 efficiency:

The B_1 efficiency included in the numerical simulations was based on measurements in the LC region in previous set of data acquired on the 3T *Prisma* scanner from the WCHN. While this parameter was considered with a low inter-subject variability, data acquired during the project was characterised by a B_1 efficiency factor in the LC region of about 1.4. This non-negligible increase had nonetheless low impact on the results interpretation which was surprising given its impact on the saturation effect. However, this finding suggests that model predictions may be robust to session-specific variability in the achieved B1 efficiency.

Regarding the literature values, one has to keep in mind the challenge in the understanding of the variability within this structure and therefore in defining precise and general tissue properties. A requirement for the future LC visualisation studies would be to better fit these parameters to the model and highlighting the potential inter-relation between those not studied during this project.

4.2 Optimisation of SPGR sequence with MT pre-pulse: simulation

Optimal parameter values suggested by the simulations of the SPGR sequence including MT pulse are more likely to fit to the *in vivo* reality since the bound pool fraction size was decreased to 0.13. Nonetheless, as previously highlighted, many parameters are involved in the MT effects and their individual characterisation is nowadays unknown and would require additional investigation.

Results would suggest that the best LC visualisation is achieved with the most powerful but short MT pulse given the maximum B_1 amplitude and pulse characteristic duration. A somewhat counter intuitive result was given by the maximisation of the off-resonance frequency. First because of the current model implementation stating that a low frequency MT pre-pulse does not result in direct saturation of the free pool as it ought to, i.e. it does not take account of the pulse's finite bandwidth. Therefore, according to the model, we would intuitively have though that the lowest frequency would be preferred for maximising MT effects. In fact, because of the Super-Lorentzian lineshape representation of the absorption rate $G(f_z)$, the higher f_z, the lower the saturation effect. One first justification for this behaviour would be the trade-off between contrast and SNR emphasised by the variable C_w according to which the optimisation is realised. This hypothesis was rejected by the optimisation of the normalised contrast C_n resulting in a off-resonance frequency suggested equal to $f_z = 8\,\text{kHz}$ and not the minimal off-resonance frequency tested of 2 kHz. Deeper investigations of these specifications regarding the MT pre-pulse should be realised in order to understand better the mechanism. This MT pulse is followed by a long TR_1 period during which exchanges can occur. The maximisation of this delay parameter between both MT and excitation pulse corresponds thereby in the maximisation of the exchange processes within tissues. Because of this long TR_1 and because of the balance with TR_2 for a given TR implemented as a constraint in the model, the duration of the MT pulse is limited to 0.2 ms, the longest as it can be permitted for the given TR_1.

While the model validation was not realised in the scope of this project, a suggested experimental protocol would be isotropic sequences with the optimal parameters determined here-above while varying the delay between the saturation and the excitation pulse, TR_1. The subsequent question to answer would be whether or not the contrast is changing according to this parameter variation allowing to validate the model.

4.3 Summary

The conclusions drawn from both model with or without MT pre-pulse differ regarding the optimal sequence suggested mainly because of the way saturation is generated within pools. In the first case, one should maximise the power of the excitation pulse. In the second case, the power of the preparation pulse is maximised through B_1 amplitude and pulse duration while its off-resonance frequency is pushed at its upper limits and delay time for maximising exchange processes between tissue pools. This MT pre-pulse configuration offers an additional means of amplifying contrast within the LC region by negative contrast generation. In other words, the MT effects have as a consequence to decrease the signal amplitude, enhancing the overall contrast. This is crucial to account for given the impact of SNR on LC visualisation.

One of the main limitation of this work lies in the insufficient model validation realised as a con-

sequence of the low amount of data acquired. However, the analysis and the comparison of simulation predictions allowed to give a first good insight on the general trend to be followed in the future when investigating the LC tissue properties.

Conclusion

In this thesis, the underlying contrast generation mechanisms between the LC and its surroundings were investigated with the aim of optimising the visualisation of this structure through spoiled gradient echo imaging.

It has been suggested that contrast enhancement could be achieved through the specification of optimal parameters, compared to the sequences currently played out at the WCHN aiming at visualising the LC, either with SPGR including or not MT preparation pulse. However, the lack of experimental data prevents the validation of the implemented model with strong confidence. This approach highlighted some crucial parameters in the study of LC contrast such as the exchange rate between compartments and the fractional bound pool size of respective tissues.

While the visualisation of the LC is challenging by its nature and given the lack of knowledge, it has been demonstrated that the Super-resolution technique provided numerous benefits for improving data quality and thereby the LC depiction highlighting the interest of including this technique in future LC studies.

Further researches are required regarding the impact of tissue-dependent parameters on the developed model and the subsequent improvement of contrast predictions within these complex tissues. However, this work provides an initial tool for better understanding the contrast mechanisms in the LC and its refinements will hopefully allow to characterise better this crucial noradrenergic structure.

Appendices

Appendix A

Additional experimental data

Data resolution

Anisotropic/Isotropic acquisition

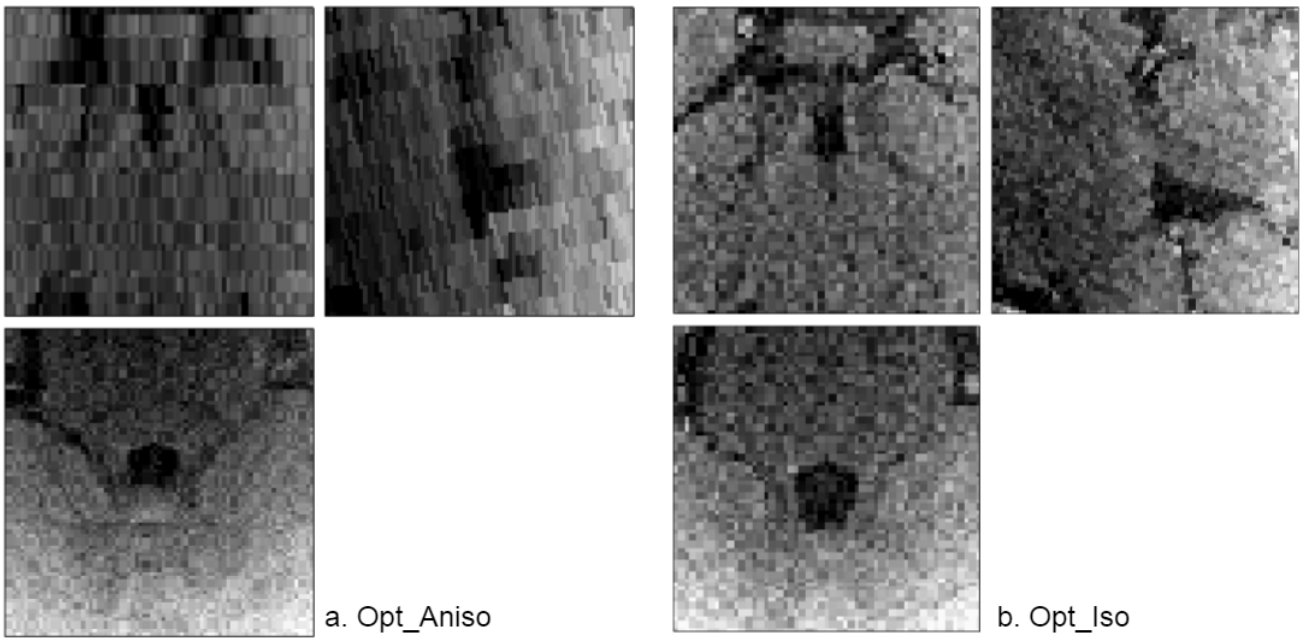

Figure A.1: Data acquired through a. the anisotropic $0.6 \times 0.6 \times 3$ mm^3 Optimal_FA7 protocol, b. the isotropic $0.6 \times 0.6 \times 0.6$ mm^3 Optimal_IsoFA7 protocol. Displayed without interpolation between voxels and zoom $40 \times 40 \times 40$ mm^3 on the LC region.

T_1-weighted sequence with BWT of 6 and 10

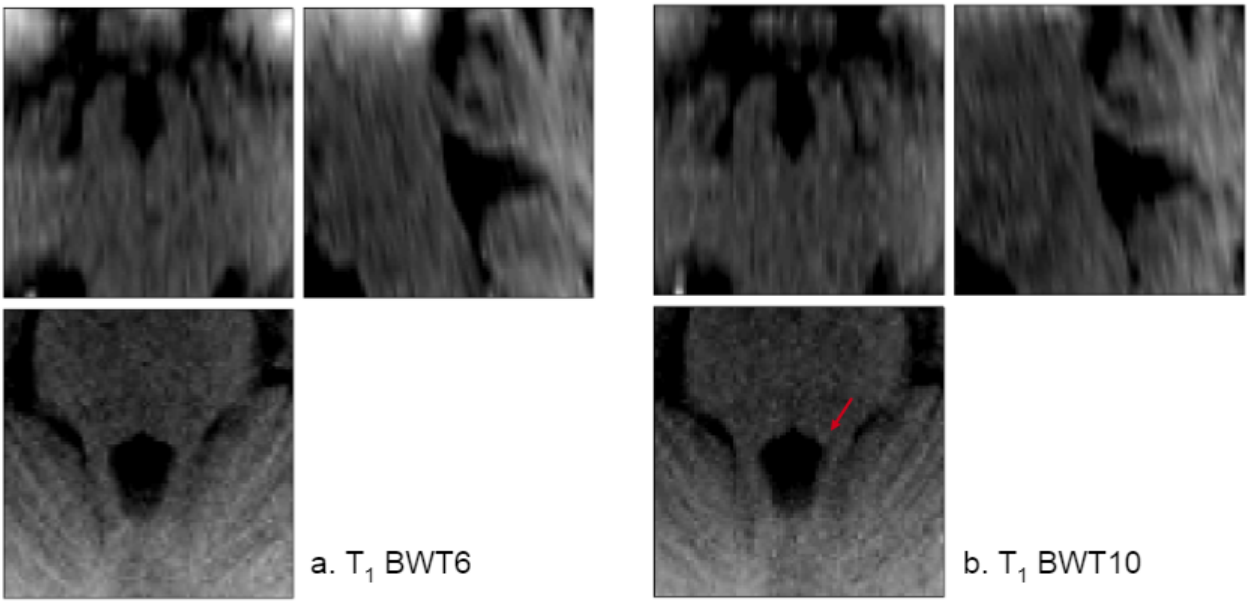

Figure A.2: Data acquired through the anisotropic T_1-weighted protocol with a bandwidth-time-product of a. 6 and b. 10. Zoom $40 \times 40 \times 40$ mm^3 on the LC region. The red arrow points to the discernable LC.

Appendix B

Contrast quantification

		Experimental data		Simulation predictions			
				$f_{surr} = 0.3$		$f_{surr} = 0.13$	
#	Sequence label	C_n (%)	C_w	C_n (%)	C_w	C_n (%)	C_w
2	PD_BWT6	4.75 $\pm$ 0.10	1757.55	44.33	3.46	9.27	0.72
3	T_1_BWT6	0.37 $\pm$0.01	102.96	35.25	2.36	9.17	0.61
4	PD_BWT10	5.06 $\pm$0.10	1875.86	51.25	3.84	11.09	0.83
5	T_1_BWT10	4.80 $\pm$ 0.10	1338.37	38.75	2.51	10.14	0.66
6	Opt	4.43 $\pm$ 0.09	1717.08	45.68	3.71	10.25	0.83
7	Opt_Inc137	7.10 $\pm$ 0.14	2779.67	44.61	3.68	9.58	0.79
8	Opt_Iso	6.67 $\pm$0.13	2625.81	45.68	3.71	10.25	0.83
10	Opt_FA11	5.61 $\pm$0.11	2186.55	47.95	4.01	11.36	0.95
11	Opt_Iso_SincNS	6.96 $\pm$ 0.14	2750.10	45.68	3.71	10.25	0.83
12	Opt_Iso_RectNS	6.22 $\pm$ 0.12	2414.89	45.68	3.71	10.25	0.83

Table B.1: Quantification of the contrast variables C_n and C_w in the data acquired during experiment and comparison with the expected contrast from SPGR simulations.

Appendix C

Optimal parameters for SPGR sequence with MT pre-pulse

Signal intensities in the LC and its surroundings

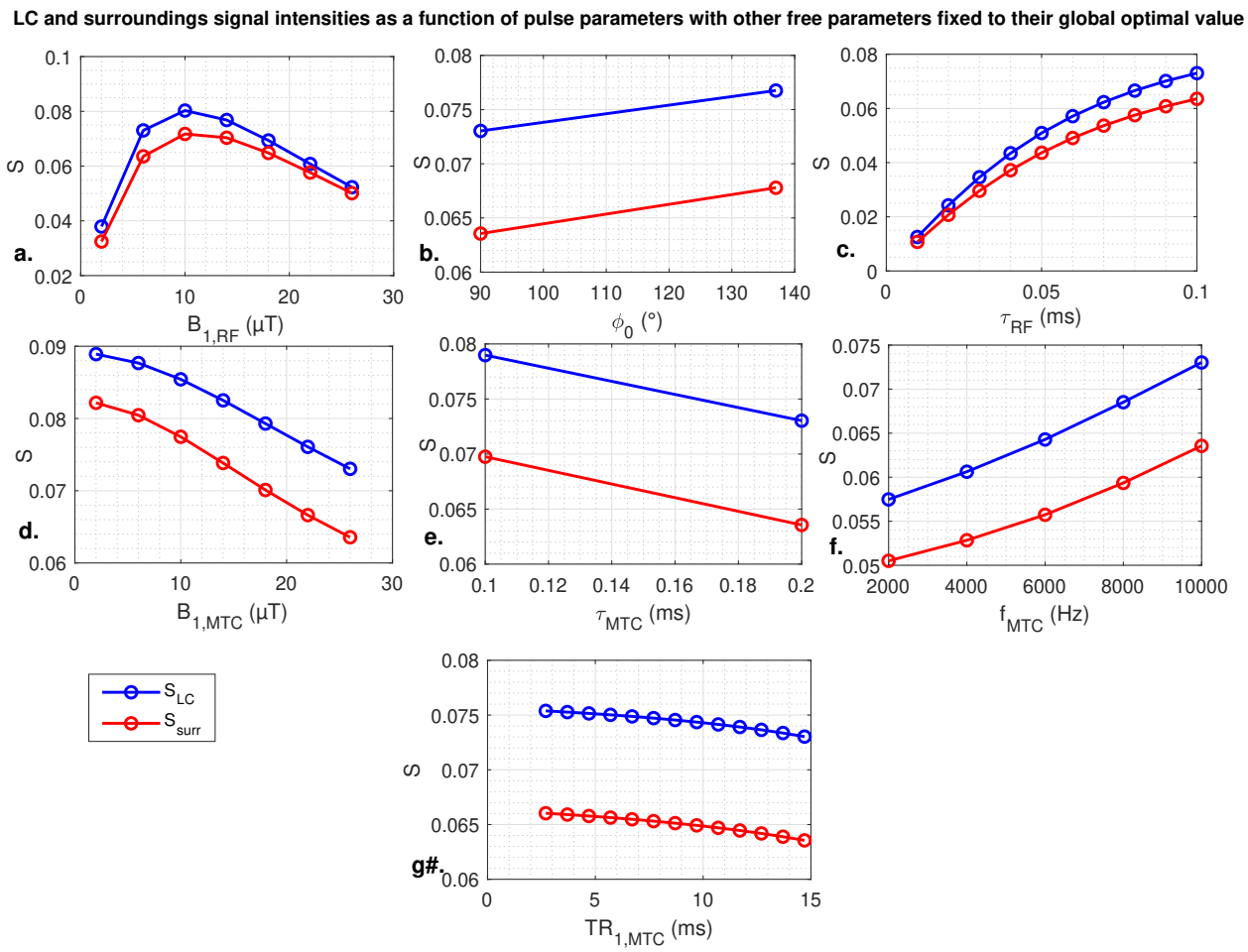

Figure C.1: LC and surroundings signal intensities as a function of $B_{1,RF}$, τ_{RF}, ϕ_0, $B_{1,MTC}$, τ_{MTC}, f_{MTC} and TR_1 around their global maximum value

Normalised contrast

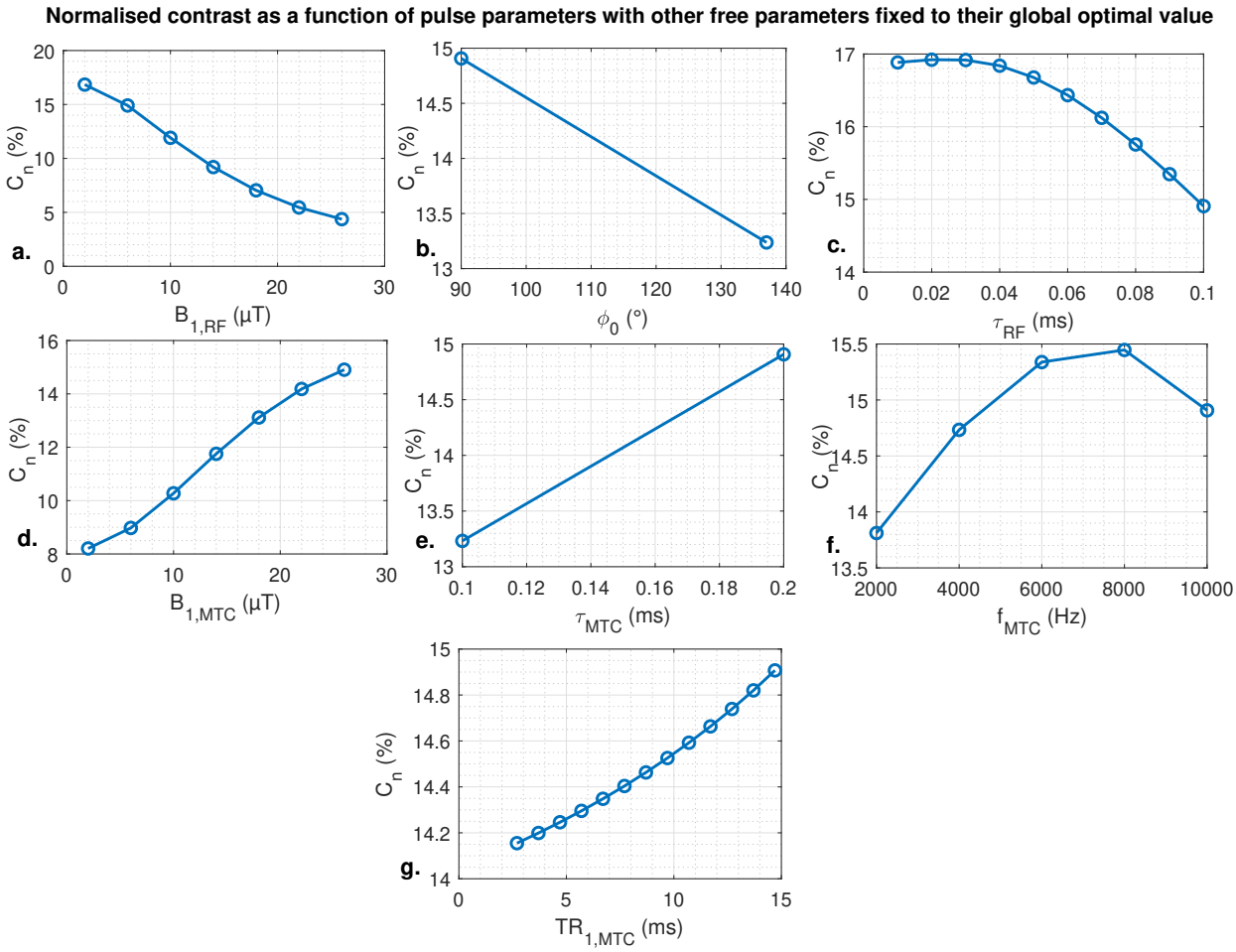

Figure C.2: Normalised contrast as a function of $B_{1,RF}$, τ_{RF}, ϕ_0, $B_{1,MTC}$, τ_{MTC}, f_{MTC} and TR_1 around their global maximum value

Appendix D

Super-Lorentzian absorption lineshape

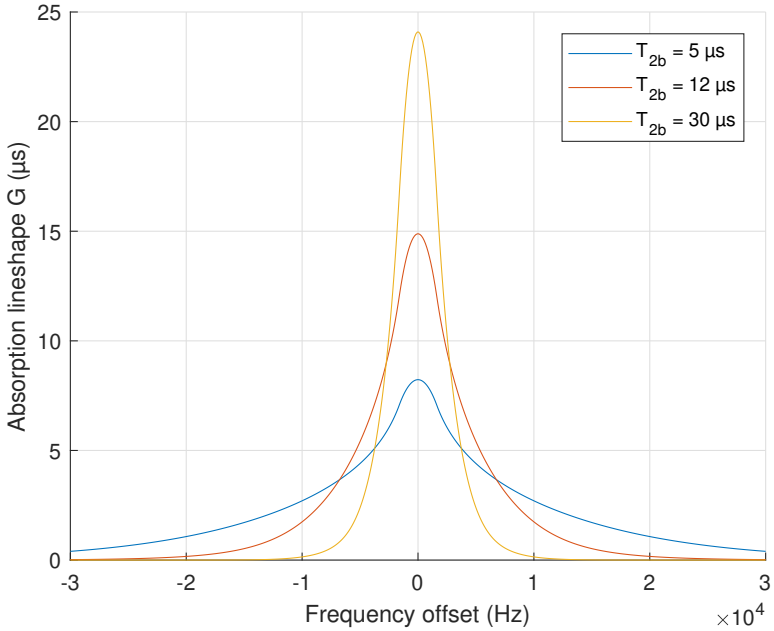

Figure D.1: Dependence of the absorption lineshape on $T_{2,b}$

Bibliography

[1] Alzheimer's Association – Stages of Alzheimer's. https://alz.org/alzheimers-dementia/stages. Last accessed on 19th April 2020.

[2] Dementia Platform UK – Medical Research Council. https://www.dementiasplatform.uk/about. Last accessed on 16th April 2020.

[3] Functional Imaging Laboratory, UCL London – Statistical Parametric Mapping. https://www.fil.ion.ucl.ac.uk/spm/. Last accessed on 14th April 2020.

[4] Le cerveau à tous les niveaux - Les troubles anxieux. http://lecerveau.mcgill.ca/flash/i/i_08/i_08_cr/i_08_cr_anx/i_08_cr_anx.html. Last accessed on 26th May 2020.

[5] G7 Academies' Joint Statements – The challenge of neurodegenerative diseases in a aging population. https://royalsociety.org/-/media/about-us/international/g-science-statements/2017-may-aging-population.pdf, 2017. Last accessed on 16th April 2020.

[6] ASTON-JONES, G., AND COHEN, J. D. Adaptive gain and the role of the locus coeruleus–norepinephrine system in optimal performance. *Journal of Comparative Neurology 493*, 1 (2005), pp. 99–110.

[7] BALTEAU, E. PHYS0128-1 Bases de l'imagerie par résonance magnétique nucléaire (slides). University of Liège, 2019-2020.

[8] BERNSTEIN, M. A., KING, K. F., AND ZHOU, X. J. *Handbook of MRI pulse sequences*. Elsevier, 2004.

[9] BETTS, M. J., KIRILINA, E., OTADUY, M. C., IVANOV, D., ACOSTA-CABRONERO, J., CALLAGHAN, M. F., LAMBERT, C., CARDENAS-BLANCO, A., PINE, K., PASSAMONTI, L., ET AL. Locus coeruleus imaging as a biomarker for noradrenergic dysfunction in neurodegenerative diseases, 2019.

[10] BLOCH, F. Nuclear induction. *Physical review 70*, 7-8 (1946), pp. 460.

[11] BOURET, S., AND SARA, S. J. Locus cœruleus. *Scholarpedia 5*, 3 (2010), pp. 2845. http://scholarpedia.org/article/Locus_coeruleus, last accessed on 24th March 2020.

[12] BROWN, R. W., CHENG, Y.-C. N., HAACKE, E. M., THOMPSON, M. R., AND VENKATESAN, R. *Magnetic resonance imaging: physical principles and sequence design*, 2nd ed. John Wiley & Sons, 2014.

[13] CERCIGNANI, M., DOWELL, N. G., AND TOFTS, P. S. *Quantitative MRI of the brain: principles of physical measurement*. CRC Press, 2018.

[14] CHAN-PALAY, V. Alterations in the locus coeruleus in dementias of Alzheimer's and Parkinson's disease. In *Progress in brain research*, vol. 88. Elsevier, 1991, pp. pp. 625–630.

[15] CHEN, X., HUDDLESTON, D. E., LANGLEY, J., AHN, S., BARNUM, C. J., FACTOR, S. A., LEVEY, A. I., AND HU, X. Simultaneous imaging of locus coeruleus and substantia nigra with a quantitative neuromelanin MRI approach. *Magnetic resonance imaging 32*, 10 (2014), pp. 1301–1306.

[16] CLEWETT, D. V., LEE, T.-H., GREENING, S., PONZIO, A., MARGALIT, E., AND MATHER, M. Neuromelanin marks the spot: identifying a locus coeruleus biomarker of cognitive reserve in healthy aging. *Neurobiology of aging 37* (2016), pp. 117–126.

[17] CONDON, B., PATTERSON, J., JENKINS, A., WYPER, D., HADLEY, D., GRANT, R., ROWAN, J., AND TEASDALE, G. MR relaxation times of cerebrospinal fluid. *Journal of computer assisted tomography 11*, 2 (1987), pp. 203–207.

[18] COSTE, A. *Methodological Developments for Sodium, Phosphorus and Lithium MRI at high magnetic field : Applications to clinical research at 3 and 7 Tesla.* PhD thesis, 10 2017.

[19] DE BOER, R. Magnetization transfer contrast Part 1: MR physics. *Medicamundi 40* (1995), pp. 64–73.

[20] ELSTER, A. D. Questions and Answers in MRI. `http://mriquestions.com/index.html`. Last accessed on 26th March 2020.

[21] FERNANDES, P., REGALA, J., CORREIA, F., AND GONÇALVES-FERREIRA, A. The human locus coeruleus 3-D stereotactic anatomy. *Surgical and radiologic anatomy 34*, 10 (2012), pp. 879–885.

[22] GLOOR, M., SCHEFFLER, K., AND BIERI, O. Quantitative magnetization transfer imaging using balanced SSFP. *Magnetic resonance in medicine 60*, 3 (2008), pp. 691–700.

[23] GRAHAM, S., AND HENKELMAN, R. M. Understanding pulsed magnetization transfer. *Journal of Magnetic Resonance Imaging 7*, 5 (1997), pp. 903–912.

[24] HÄMMERER, D., CALLAGHAN, M. F., HOPKINS, A., KOSCIESSA, J., BETTS, M., CARDENAS-BLANCO, A., KANOWSKI, M., WEISKOPF, N., DAYAN, P., DOLAN, R. J., ET AL. Locus coeruleus integrity in old age is selectively related to memories linked with salient negative events. *Proceedings of the National Academy of Sciences 115*, 9 (2018), pp. 2228–2233.

[25] HAYNES, H., AND HOLMES, W. *The Emergence of Magnetic Resonance Imaging (MRI) for 3D Analysis of Sediment Beds*. 2013. `https://www.researchgate.net/figure/Schematic-diagram-of-an-MRI-machine-illustrating-the-concentric-arrangement-of-coils_fig1_266266309`, last accessed on 14th May 2020.

[26] HELMS, G., DATHE, H., KALLENBERG, K., AND DECHENT, P. High-resolution maps of magnetization transfer with inherent correction for RF inhomogeneity and T1 relaxation obtained from 3D FLASH MRI. *Magnetic Resonance in Medicine: An Official Journal of the International Society for Magnetic Resonance in Medicine 60*, 6 (2008), pp. 1396–1407.

[27] KU, H. H., ET AL. Notes on the use of propagation of error formulas. *Journal of Research of the National Bureau of Standards 70*, 4 (1966), pp. 263–273.

[28] LANGLEY, J., HUDDLESTON, D. E., LIU, C. J., AND HU, X. Reproducibility of locus coeruleus and substantia nigra imaging with neuromelanin sensitive MRI. *Magnetic Resonance Materials in Physics, Biology and Medicine 30*, 2 (2017), pp. 121–125.

[29] LIU, K. Y., ACOSTA-CABRONERO, J., CARDENAS-BLANCO, A., LOANE, C., BERRY, A. J., BETTS, M. J., KIEVIT, R. A., HENSON, R. N., DÜZEL, E., HOWARD, R., ET AL. In vivo visualization of age-related differences in the locus coeruleus. *Neurobiology of aging 74* (2019), pp. 101–111.

[30] LIU, K. Y., MARIJATTA, F., HÄMMERER, D., ACOSTA-CABRONERO, J., DÜZEL, E., AND HOWARD, R. J. Magnetic resonance imaging of the human locus coeruleus: A systematic review. *Neuroscience & Biobehavioral Reviews 83* (2017), pp. 325–355.

[31] MALIK, S. J., TEIXEIRA, R. P. A., AND HAJNAL, J. V. Extended phase graph formalism for systems with magnetization transfer and exchange. *Magnetic resonance in medicine 80*, 2 (2018), pp. 767–779. EPG-X source code repository : `https://github.com/mriphysics/EPG-X`. Last accessed on 21th May 2020.

[32] MATSUURA, K., MAEDA, M., YATA, K., ICHIBA, Y., YAMAGUCHI, T., KANAMARU, K., AND TOMIMOTO, H. Neuromelanin magnetic resonance imaging in Parkinson's disease and multiple system atrophy. *European neurology 70*, 1-2 (2013), pp.70–77.

[33] NEWCOMB, B. Researchers pinpoint brain region as 'ground zero' of Alzheimer's disease. USC, 2016. `https://news.usc.edu/91957/researchers-pinpoint-brain-region-as-ground-zero-of-alzheimers-disease/`. Last accessed on 14th May 2020.

[34] PREIBISCH, C., AND DEICHMANN, R. Influence of RF spoiling on the stability and accuracy of T1 mapping based on spoiled FLASH with varying flip angles. *Magnetic Resonance in Medicine: An Official Journal of the International Society for Magnetic Resonance in Medicine 61*, 1 (2009), pp. 125–135.

[35] PRINCE, J. L., AND LINKS, J. M. *Medical imaging signals and systems*. Pearson Prentice Hall Upper Saddle River, NJ, 2006.

[36] PRIOVOULOS, N., JACOBS, H. I., IVANOV, D., ULUDAĞ, K., VERHEY, F. R., AND POSER, B. A. High-resolution in vivo imaging of human locus coeruleus by magnetization transfer MRI at 3T and 7T. *NeuroImage 168* (2018), pp. 427–436.

[37] SARA, S. J. The locus coeruleus and noradrenergic modulation of cognition. *Nature reviews neuroscience 10*, 3 (2009), pp. 211–223.

[38] SASAKI, M., SHIBATA, E., TOHYAMA, K., TAKAHASHI, J., OTSUKA, K., TSUCHIYA, K., TAKAHASHI, S., EHARA, S., TERAYAMA, Y., AND SAKAI, A. Neuromelanin magnetic resonance imaging of locus ceruleus and substantia nigra in Parkinson's disease. *Neuroreport 17*, 11 (2006), pp. 1215–1218.

[39] SLED, J. G., AND PIKE, G. B. Quantitative imaging of magnetization transfer exchange and relaxation properties in vivo using MRI. *Magnetic Resonance in Medicine: An Official Journal of the International Society for Magnetic Resonance in Medicine 46*, 5 (2001), pp. 923–931.

[40] THEOFILAS, P., EHRENBERG, A. J., DUNLOP, S., ALHO, A. T. D. L., NGUY, A., LEITE, R. E. P., RODRIGUEZ, R. D., MEJIA, M. B., SUEMOTO, C. K., FERRETTI-REBUSTINI, R. E. D. L., ET AL. Locus coeruleus volume and cell population changes during Alzheimer's disease progression: a stereological study in human postmortem brains with potential implication for early-stage biomarker discovery. *Alzheimer's & Dementia 13*, 3 (2017), pp. 236–246.

[41] TONA, K.-D., VAN OSCH, M. J., NIEUWENHUIS, S., AND KEUKEN, M. C. Quantifying the contrast of the human locus coeruleus in vivo at 7 Tesla MRI. *PloS one 14*, 2 (2019).

[42] TRUJILLO, P., PETERSEN, K. J., CRONIN, M. J., LIN, Y.-C., KANG, H., DONAHUE, M. J., SMITH, S. A., AND CLAASSEN, D. O. Quantitative magnetization transfer imaging of the human locus coeruleus. *NeuroImage 200* (2019), pp. 191–198.

[43] TRUJILLO, P., SUMMERS, P. E., FERRARI, E., ZUCCA, F. A., STURINI, M., MAINARDI, L. T., CERUTTI, S., SMITH, A. K., SMITH, S. A., ZECCA, L., ET AL. Contrast mechanisms associated with neuromelanin-MRI. *Magnetic resonance in medicine 78*, 5 (2017), pp. 1790–1800.

[44] VAN ZIJL, P. C., LAM, W. W., XU, J., KNUTSSON, L., AND STANISZ, G. J. Magnetization Transfer Contrast and Chemical Exchange Saturation Transfer MRI. Features and analysis of the field-dependent saturation spectrum. *Neuroimage 168* (2018), pp. 222–241.

[45] WANSAPURA, J. P., HOLLAND, S. K., DUNN, R. S., AND BALL JR, W. S. NMR relaxation times in the human brain at 3.0 tesla. *Journal of Magnetic Resonance Imaging: An Official Journal of the International Society for Magnetic Resonance in Medicine 9*, 4 (1999), pp.531–538.

[46] WATANABE, T., TAN, Z., WANG, X., MARTINEZ-HERNANDEZ, A., AND FRAHM, J. Magnetic resonance imaging of noradrenergic neurons. *Brain Structure and Function 224*, 4 (2019), pp. 1609–1625.

[47] WCHN. Denoising/Super-resolution code repository. `https://github.com/balbasty/super-resolution/`. Last accessed on 24th April 2020.

[48] WEIGEL, M. Extended phase graphs: dephasing, RF pulses, and echoes-pure and simple. *Journal of Magnetic Resonance Imaging 41*, 2 (2015), pp. 266–295.

[49] WEISKOPF, N., SUCKLING, J., WILLIAMS, G., CORREIA, M. M., INKSTER, B., TAIT, R., OOI, C., BULLMORE, E. T., AND LUTTI, A. Quantitative multi-parameter mapping of R1, PD*, MT, and R2* at 3T: a multi-center validation. *Frontiers in neuroscience 7* (2013), pp. 95.